Astronomy Letters, Vol. 30, No. 8, 2004, pp. 509–513. Translated from Pis'ma v Astronomicheskiĭ Zhurnal, Vol. 30, No. 8, 2004, pp. 563–567.

Hydrogen Absorption Lines in the Cosmic Microwave Background Spectrum

V. K. Dubrovich[1,2] and N. N. Shakhvorostova[3*]

[1] *Special Astrophysical Observatory, St. Petersburg Branch, Russian Academy of Sciences, St. Petersburg, Russia*

[2] *Pulkovo Astronomical Observatory, Russian Academy of Sciences, St. Petersburg, Russia*

[3] *Astrospace Center, Lebedev Physical Institute, Russian Academy of Sciences, Moscow, Russia*

Received November 4, 2003

Abstract—We have calculated the intensities of the subordinate hydrogen lines formed during the recombination epoch at redshifts $800 \lesssim z \lesssim 1600$. We show that an allowance for the angular momentum splitting of hydrogen atomic energy levels and the dipole transition selection rules can reveal absorption features in the cosmic microwave background recombination spectrum in the submillimeter wavelength range. © *2004 MAIK "Nauka/Interperiodica"*.

Key words: *theoretical and observational cosmology, CMB spectrum, CMB recombination lines, recombination epoch.*

INTRODUCTION

The problem of recombination lines in the cosmic microwave background (CMB) spectrum formed during the recombination of primordial hydrogen and helium in the early Universe has been discussed for more than 30 years (Zel'dovich *et al.* 1968; Dubrovich 1975; Bernshtein *et al.* 1977; Beigman and Sunyaev 1978; Dubrovich and Stolyarov 1995; Burdyuzha and Chekmezov 1994; Grachev and Dubrovich 1991; Burgin 2003). This problem is important because of the unique opportunities to estimate the fundamental parameters of the Universe. In particular, the dependence of the change in the Hubble constant on the scale factor can be reconstructed with a higher accuracy by analyzing the line profiles. In addition, the detection of such lines will allow us to reach higher z (using He I lines).

Potentially, the first resonance hydrogen line, Lα, must have been strongest. However, Zel'dovich *et al.* (1968) showed that this line as a rather narrow spectral feature is not formed due to the peculiarities of the recombination process, i.e., its strong reabsorption by neutral hydrogen and the subsequent two-photon decay with a continuum spectrum of the final photons. This result also proved to be of fundamental importance in understanding the subsequent calculations of the hydrogen recombination dynamics, which, in turn, is required to describe in detail the power spectrum of the spatial CMB temperature fluctuations. The most recent observations of these fluctuations (Tegmark *et al.* 2003) have brilliantly confirmed the validity of the main ideas of Zel'dovich *et al.* (1968).

However, the question of recombination lines formed during transitions from other levels was not considered in detail. This was done several years later by Dubrovich (1975), Bershtein *et al.* (1977), Beigman and Sunyaev (1978), and in more recent papers. It turned out that the almost complete absence of reabsorption for the lines of high subordinate series leads to their survival. As a result, one might expect the CMB spectrum at the current epoch to exhibit relatively narrow features whose parameters are unambiguously determined by recombination dynamics and the atomic constants of hydrogen and helium.

RECOMBINATION KINETICS

Since the intensities of recombination lines proved to be very difficult to determine accurately, all authors used certain assumptions that allowed the calculations to be simplified. The main difficulties arise from the presence of an external radiation field, which leads to multiple upward and downward level transitions, and the large number of levels when taking into account the dipole transition selection rules and, accordingly, the level orbital momentum structure. The first difficulty can be overcome by assuming that the recombination rate can be factorized into two independent cofactors: the so-called transition efficiency

[*] E-mail: nadya@asc.rssi.ru

and the recombination dynamics, which is common to all transitions. The second difficulty can be overcome by taking the matrix of the transition probabilities averaged over the angular momenta of each level as the base matrix. Numerous test calculations showed that the first assumption holds with a very high accuracy. There was some vagueness regarding the second assumption, because very cumbersome calculations were required to test it. Some of the qualitative physical arguments instilled much confidence in applying this approximation to levels with large quantum numbers, which was usually considered as well. However, the situation was less certain for transitions in the Balmer and close series. Moreover, these series were shown (Dubrovich 1997) to differ from other series due to the peculiarities of the recombination process.

Let us recall the main points of the theory of primordial hydrogen recombination. A free electron recombines with a proton to form a hydrogen atom in an excited state with a high (relative) probability. Subsequently, the electron either descends diffusively to the ground level or again becomes free through ionization. In the former case, the ground state can be reached in two alternative ways — via a single-photon resonance transition with the emission of a Lyman-photon in a very narrow spectral range or via a two-photon decay of the excited state with the emission of continuum photons. Since the optical depth of the primordial plasma for Lyman photon recapture is large, the emission of these photons does not actually lead to the formation of a ground-state atom. Total recombination can be achieved only via the second process – two-photon decay. Calculations show that the decay of the $2S$ level makes the largest contribution to this channel (Zel'dovich *et al.* 1968; Dubrovich 1987). Here, we disregard the contribution from other levels, but we plan to take them into account in our subsequent work. Thus, the recapture of Lyman photons (in particular, Lα) cannot depopulate the $2P$ level. At the same time, cascade transitions from higher levels and direct recombination to the $2P$ level populate it significantly. Therefore, we must consider the processes of the hydrogen atomic transition from $2P$ to $2S$.

The simplest mechanism, the radiative $2P \rightarrow 2S$ transition, proves to be inefficient for hydrogen, because the energy difference between these two states is very small (for He I, e.g., this is not the case, and this transition is the main channel). The probability of this transition is very low because of collisions with other particles. Only the radiative channel associated with the transitions to higher levels and the subsequent downward cascade transitions remains. The first permitted transition of this kind is the $2P \rightarrow 4D(S) \rightarrow 3P \rightarrow 2S$ track. At the first step, a Balmer Hβ photon from the external radiation field is absorbed. At the second and third steps, Paschen Pα and Balmer Hα photons, respectively, are emitted. The probability of this variant compared to other variants is very high. Other similar tracks should also be considered for completeness.

All this refines the formulation of the problem of hydrogen recombination, which is broken down into two subproblems: the recombination dynamics and the formation of recombination lines. To take into account the difference between the $2P$ and $2S$ level in the first subproblem, we can correct the statistical weight of the second level with sufficient accuracy by setting it equal to one instead of four, as is done in all present-day calculations (Grachev and Dubrovich 1991; Saselov *et al.* 1999). This approach works, because the rates of the radiative cascades under consideration are very high. However, the probability ratio of various cascade transitions rather than their absolute rates is important for calculating the intensities of recombination lines. In this case, the appearance or disappearance of a certain channel can change fundamentally the intensity of a particular line, and an allowance for the specific features of the level population process can even reverse the sign of the effect.

To calculate the line intensities, we must use the Einstein coefficients not averaged over the angular momentum in the transition probability matrix and write the level population vector by taking into account each sublevel. However, the splitting should be considered only for a few levels with small principal quantum numbers, while averaging should be used for higher levels as before. This approximation is dictated by computational limitations and is justified by the fairly rapid decrease in the probability of the transition from the $2P$ level to these levels. In this formulation of the problem, Burgin (2003) calculated the relative line formation probabilities for given transitions, i.e., the efficiencies mentioned above (Dubrovich 1975; Bernshtein *et al.* 1977). Some of these proved to be negative. This means that, to transfer electrons from $2P$ to $2S$, more photons of the corresponding frequencies than those emitted during recombination must be absorbed. Additional photons of these frequencies come from the main equilibrium cosmic microwave background. The efficiencies listed in the table for a set of ten lines are the result of the combined action of the two processes (absorption and emission).

Our objective is to determine the ultimate form of the spectral distortions in the Wien region of the CMB spectrum by taking into account the inferred efficiencies.

Values of η_l calculated by taking into account the level splitting in angular momentum l for the subordinate hydrogen lines

$n_{\rm up}\backslash n_{\rm low}$	2	3	4	5
3	7.75×10^{-1}	–	–	–
4	-1.40×10^{-1}	4.33×10^{-1}	–	–
5	-4.53×10^{-3}	7.48×10^{-2}	9.80×10^{-2}	–
6	5.94×10^{-3}	2.83×10^{-2}	2.92×10^{-2}	4.05×10^{-2}

Note. $n_{\rm up}$ and $n_{\rm low}$ are the numbers of the upper and lower levels, respectively, corresponding to the $n_{\rm up}\longrightarrow n_{\rm low}$ transition.

THE FORMATION OF CMB SPECTRAL DISTORSIONS IN THE WIEN REGION

Basic Equations and Relations

For convenience of calculation, we derived the basic relations in a comoving frame of reference. The relation between the physical and comoving volume elements is $dV=a^3d\bar{V}$, where a is the scale factor. For arbitrary particles whose number N is conserved over a fairly long time interval, $NdV=\bar{N}d\bar{V}$ and, consequently, $N=\bar{N}/a^3$. Below, the letters with a bar denote the quantities that refer to the comoving volume.

The relation between the observed photon frequency $\bar{\nu}$ and the frequency ν at time $t(a)$ is $\nu=\bar{\nu}/a$, i.e., $d\nu=d\bar{\nu}/a$. In the absence of emission and absorption, the relation $N_\nu d\nu dV=$ const and, consequently, $N_\nu(d\bar{\nu}/a)a^3d\bar{V}=$ const is valid for the monochromatic photon density N_ν. Thus, $N_\nu=$ const, where $\bar{N}_\nu=N_\nu a^2$.

The current monochromatic density of the photons that are in excess with respect to the CMB radiation at frequency $\bar{\nu}$ is given by

$$\bar{N}_\nu(\bar{\nu})=\int\limits_{t(0)}^{t(1)}\bar{Z}_\nu(\bar{\nu},a)e^{-\tau(\bar{\nu},a)}dt \qquad (1)$$
$$=\int\limits_0^1\frac{\bar{Z}_\nu(\bar{\nu},a)e^{-\tau(\bar{\nu},a)}}{\dot{a}}da.$$

Here, $\bar{Z}_\nu(\bar{\nu},a)$ is the rate of uncompensated radiative transitions per unit comoving volume per interval $\bar{\nu}$ of reduced frequencies, and $\tau(\bar{\nu},a)$ is the continuum absorption optical path for the photon emitted at time $t(a)$ and observed at time $t(1)$ at frequency $\bar{\nu}$,

$$\tau(\bar{\nu},a)=\int\limits_{t(a)}^{t(1)}k_c(\nu,a)cdt=\int\limits_a^1\frac{ck_c(\nu,a)}{\dot{a}}da, \qquad (2)$$

where $k_c=k_c(\nu,a)$ is the continuum absorption coefficient at frequency ν at time $t(a)$ with an allowance made for the induced emission, which is given by

$$k_c(\nu,a)=n_en^+\frac{16\pi^2e^6kT(a)}{3\sqrt{3}ch} \qquad (3)$$
$$\times\frac{1}{(2\pi mkT(a))^{3/2}}\frac{g_\nu}{\nu^3}.$$

Here, T is the temperature of the matter and radiation at time $t(a)$, and g_ν is the Gaunt factor.

The emission profile for a single narrow line can be fitted by the Dirac δ-function. Thus, the rate of uncompensated transitions per unit frequency interval per unit physical volume is

$$Z(\nu,a)=Z_l(a)\delta(\nu-\nu_l), \qquad (4)$$

where $Z_l(a)$ is the rate of uncompensated transitions in the spectral line per unit physical volume at time $t(a)$.

Let us introduce certain designations and quantities. Let N_X and $\bar{N}_X$ be the numbers of particles per unit physical and comoving volumes, respectively, and N_X^A be the number of atoms of ion X (the sum over all degrees of ionization). The fraction of the ions X in the total number of the corresponding atoms is then $f_X=\bar{N}_X/\bar{N}_X^A$. The fraction $\hat{f}_X$ of the ions with degrees of ionization lower than or equal to X in the total number of the corresponding atoms for HI, HeI, and HeII clearly obeys the relations $\hat{f}_{\rm HI}=f_{\rm HI}$ and $\hat{f}_{\rm HeI}=f_{\rm HeI}$. The rate $\bar{r}_X$ of formation of atoms of element X through uncompensated recombinations per unit comoving volume is

$$\bar{r}_X=\bar{N}_X^A\hat{f}'_X, \qquad (5)$$

where $\hat{f}'_X=d\hat{f}_X/da$.

Using Eq. (5), we obtain the following formula for $Z_l(a)$:

$$Z_l(a)=\frac{\bar{Z}_l}{a^3}=\frac{\eta_l\bar{r}_X}{a^3}. \qquad (6)$$

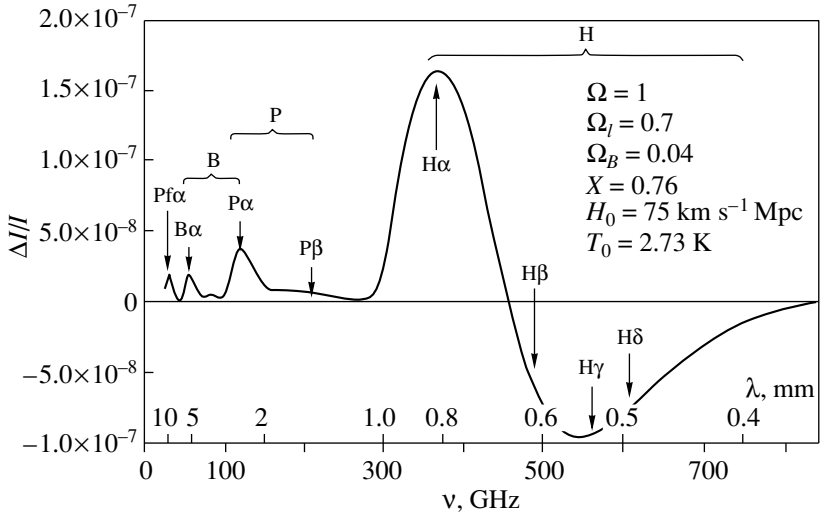

Recombination spectrum of the CMB distortions in the Wien region. $\Delta I/I$ is the relative change in intensity, ν is the radiation frequency, and λ is the wavelength.

Here, $\bar{Z}_l$ is the rate of uncompensated transitions in the spectral line per unit comoving volume, and η_l is the ratio of the rates of uncompensated transitions in this line and in the Lα line, i.e., $\eta_l = \eta_{ij} = Z_{ij}/Z_{21}$. This quantity was first introduced by Bernshtein *et al.* (1977) and was numerically calculated for various lines with an allowance made for the splitting in orbital momentum l of the atom by Burgin (2003a).

Using Eqs. (4) and (6), we transform Eq. (1) to

$$\bar{N}_\nu(\bar{\nu}) = \int_0^1 \frac{\bar{Z}_\nu(\bar{\nu},a)e^{-\tau(\bar{\nu},a)}}{\dot{a}}da \qquad (7)$$

$$= \int_0^1 \frac{Z_\nu(\nu,a)a^2e^{-\tau(\nu,a)}}{\dot{a}}da$$

$$= \begin{cases} \eta_l \bar{N}_X^A \hat{f}'_X(a_l)e^{-\tau(\bar{\nu},a_l)}/\nu_l, & \bar{\nu} < \nu_l \\ 0, & \bar{\nu} > \nu_l, \end{cases}$$

where $a_l = \bar{\nu}/\nu_l$.

However, we are concerned not with $\bar{N}_\nu$, but with the ratio $\Delta I_\nu/B_\nu$, where ΔI_ν is the change in intensity at frequency ν, and B_ν, the intensity of a uniform cosmic microwave background at the same frequency calculated using Planck's formula. The sought ratio is given by

$$\frac{\Delta I_\nu}{B_\nu} = \frac{ch\nu N_\nu}{4\pi B_\nu}, \qquad (8)$$

where c is the speed of light in a vacuum, and h is Planck's constant.

Model Parameters and Results of Calculations

In our calculations, we considered ten lines (see the table) for which Burgin (2003b) calculated η_l by taking into account all of the states with $2 \le n \le 6$, $0 \le l < n$ and only these. All of the remaining initial assumptions and the method of calculations were described by Burgin (2003a). We determined $\bar{N}_X^A$ and $d\hat{f}_X$ using the recombination kinetics calculated by Grachev and Dubrovich (1991). The parameters of the cosmological model used in our calculations were the following: $\Omega = 1$, $\Omega_l = 0.7$, $\Omega_B = 0.04$, $X = 0.76$ (hydrogen mass fraction), $H_0 = 75$ km s^{-1}Mpc^{-1}, and $T_0 = 2.73$ K.

For each line, we calculated the large-scale $\Delta I_\nu/B_\nu$ profile attributable to the cosmological expansion of the Universe and then obtained the recombination spectrum of the CMB distortions by adding up the ten calculated profiles. Note that it makes sense to consider the ratio $\Delta I_\nu/B_\nu$ only in a limited frequency range (and, accordingly, in a limited range of redshifts z), because other types of intense radiation (Galactic and extragalactic) are superimposed on the CMB radiation in the Wien region.

The figure shows the resulting spectrum of the CMB distortions in the region concerned that corresponds to the frequency range $100 < \nu < 800$ GHz and, accordingly, the redshift range $700 < z < 1800$. This range covers the entire recombination period.

As we see from the figure, the spectrum of the CMB distortions contains an absorption component. It is attributable to the negative η_l for the Hβ and Hγ lines. During the transition of a hydrogen atom from $2P$ to $2S$, the photons of the corresponding frequencies are absorbed from the surrounding uniform CMB radiation field. The number of absorbed photons of these frequencies is larger than the number

of similar photons emitted through recombination. As was pointed out in the Introduction, this is the reason why the line efficiencies (i.e., η_l) are negative.

CONCLUSIONS

We have calculated the spectrum of hydrogen recombination lines in the Wien region of the CMB radiation near its maximum. We showed that the correct analysis of the recombination kinetics can reveal the absorption features in the hydrogen recombination spectrum that correspond to the Hβ and Hγ lines. The presence of such features is an interesting fact of the conditions of almost complete thermodynamic equilibrium during the hydrogen recombination epoch. Observationally, this can increase significantly the detection probability of these spectral lines.

A detailed analysis of the observing technique and the prospects for detecting these lines is beyond the scope of this study. Note only that the rapid increase in the number of submillimiter-wavelength telescopes and detectors and the emergence and development of new microbolometer arrays give hope that the predicted calculated distortions of the CMB radiation will be actually detected in the near future.

In addition, note the importance of solving a similar problem for a more realistic cosmological model that includes the small-scale fluctuations of the baryonic density. Of particular importance in this case is the sharp decrease in the line width from each individual fluctuation and the possible increase in the line intensity due to an increase in the baryonic overdensity. In fact, we are dealing with the Balmer emission of individual clouds during the recombination epoch. The absorption features are preserved in this case because the overall formation physics of the radiation spectrum for fluctuations is the same as that for uniform and isotropic baryonic matter, on average. We plan to consider this issue in more detail in our forthcoming papers.

ACKNOWLEDGMENTS

This work was supported by the Russian Foundation for Basic Research (project no. 02-02-16535). We are grateful to M.S. Burgin (Astrospace Center, Lebedev Physical Institute, Russian Academy of Sciences) and S.I. Grachev (Astronomical Institute, St. Petersburg State University) for the provided data before their publication and valuable remarks. We are also grateful to V.G. Kurt and N.S. Kardashev (Astrospace Center, Lebedev Physical Institute, Russian Academy of Sciences) for their support and interest in this work.

REFERENCES

1. I. L. Beĭgman and R. A. Sunyaev, Preprint No. 164, FIAN (Lebedev Phys. Inst., Moscow, 1978).
2. I. N. Bernshteĭn, D. N. Bernshteĭn, and V. K. Dubrovich, Astron. Zh. **54**, 727 (1977) [Sov. Astron. **21**, 409 (1977)].
3. M. S. Burgin, Astron. Zh. **80**, 771 (2003) [Astron. Rep. **47**, 709 (2003)].
4. M. S. Burgin, private communication (2003).
5. V. V. Burdyuzha and A. N. Chekmezov, Astron. Zh. **71**, 341 (1994) [Astron. Rep. **38**, 297 (1994)].
6. V. K. Dubrovich, Pis'ma Astron. Zh. **1**, 3 (1975) [Sov. Astron. Lett. **1**, 196 (1975)].
7. V. K. Dubrovich, Opt. Spektrosk. **63**, 439 (1987).
8. V. K. Dubrovich and V. A. Stolyarov, Astron. Astrophys. **302**, 635 (1995).
9. V. K. Dubrovich, Doctoral Dissertation in Mathematical Physics (Spets. Astron. Obs. Ross. Akad. Nauk, Nizhniĭ Arkhyz, 1997).
10. S. I. Grachev and V. K. Dubrovich, Astrofizika **34**, 249 (1991).
11. Saselov *et al.,* astro-ph/9912182 (1999).
12. M. Tegmark *et al.*, astro-ph/0310723 (2003).
13. Ya. B. Zel'dovich, V. G. Kurt, and R. A. Sunyaev, Zh. Éksp. Teor. Fiz. **55**, 278 (1968) [Sov. Phys. JETP **28**, 146 (1969)].

Translated by G. Rudnitskii

Astronomy Letters, Vol. 30, No. 8, 2004, pp. 514–518. Translated from Pis'ma v Astronomicheskiĭ Zhurnal, Vol. 30, No. 8, 2004, pp. 568–573.

Galactic Bars and Spirals as Slow Modes of Stellar Disks

E. V. Polyachenko*

Institute of Astronomy, Russian Academy of Sciences, Pyatnitskaya ul. 48, Moscow, 119017 Russia

Received September 8, 2003; in final form, March 4, 2004

Abstract—We suggest a new approach to the description of galactic structures. This approach is based on the hypothesis that these may be treated as low-frequency (slow) modes in a stellar disk that consists of orbits precessing with different angular velocities. The definition of the modes is mathematically formulated as an eigenvalue problem for the Fredholm integral operator. Two types of modes (barlike and spiral) are shown to exist. When the resonance interaction is disregarded, the bar modes are neutral disk perturbations. Their growth is attributable to the influence of the long-range gravitational field of the modes on the stars in the region of corotation and outer Lindblad resonance. The spiral perturbations are waves with a zero total angular momentum. Their growth may be due to the inner Lindblad resonance. We demonstrate the efficiency of our approximation by comparison with N-body simulations. © *2004 MAIK "Nauka/Interperiodica"*.

Key words: *galaxies*.

INTRODUCTION

Kalnajs (1965) and Shu (1970) derived general integral equations for determining the disk eigenmodes. However, these equations remained virtually unused because of their complexity. For the same reason, analyzes of general integral equations could not provide an insight into the physical mechanisms of mode formation and reveal the instabilities responsible for this. At present, analyses of the stellar disk most commonly reduce to numerical N-body simulations that are difficult to interpret. In contrast, most of the analytical approaches substitute an effective gaseous disk for the stellar disk (see, e.g., Bertin and Lin 1996).

The situation is greatly simplified if we deal not with arbitrary disk modes but only with low-frequency modes. Consider an axisymmetric disk with an unperturbed potential $\Phi_0(r)$ and the corresponding angular velocity $\Omega(r)$ of the circular rotation. Let an orbit precessing at an angular velocity $\Omega_{\rm pr}$ be subjected to the perturbing potential of a mode that rotates at an angular velocity $\Omega_{\rm p}$. As Lynden-Bell (1979) pointed out, if

$$\epsilon = \frac{\delta\Omega}{\Omega} = \frac{|\Omega_{\rm p} - \Omega_{\rm pr}|}{\Omega} \ll 1, \qquad (1)$$

then we may assume that the orbit as a whole (rather than the individual stars in it) will respond to such a perturbation. We may then represent the disk as a set of precessing orbits. In this model, the normal modes are orbit compression and rarefaction waves that travel azimuthally at an angular velocity $\Omega_{\rm p}$ of the order of $\Omega_{\rm pr}$. The angular velocity $\Omega_{\rm pr}$ of the orbital precession is low compared to the angular velocity Ω of the disk rotation; in this sense, the modes under consideration are low-frequency modes. For these modes, we can derive a comparatively simple integral equation that can be analyzed in general form and effectively solved.

Let us assume, as a hypothesis, that the observed galactic structures can be described as low-frequency modes. At first glance, this hypothesis seems to be implausible, because bars and spirals usually reach the corotation radius at which the angular velocity of the pattern is equal to that of the disk. Note, however, that the disk mode can be determined by the central part due to the strong mass concentration at the center of the disk and its rapid decrease with increasing radius. The applicability of this theory then follows from estimates of ϵ (1) for typical galactic disk models. Thus, for example, using the data by Lin *et al.* (1969) for the spirals of our Galaxy, we can show that ϵ is less than 0.1 even at a Galactocentric distance of 12 kpc. Virtually the same is true for bar modes: ϵ is $\sim$0.1 for the angular velocities of the modes in Plummer's potential $\Phi_0(r) = -(1+r^2)^{-1/2}$ at $r \lesssim 1$ found by Athanassoula and Selwood (1986) through numerical N-body simulations. The value of ϵ is $\sim$0.3 only for the highest-frequency modes. The hypothesis under consideration will be better substantiated in a separate paper, although the most important argument for this approach is, of course, the good

*E-mail: epolyach@inasan.ru

agreement between the modes found using it and the results of detailed N-body simulations for a large number of models.

Mathematically, our approach is based on an analysis of the linear integral equation for low-frequency normal modes. A general analysis of this integral equation can be easily performed, and it reveals the main properties of its solution. The eigenfrequencies of the model stellar disk inferred using this approach are then compared with N-body simulations (Athanassoula and Sellwood 1986). In the Conclusion, we discuss our results.

BASIC EQUATIONS

The low-frequency bisymmetric modes ($m = 2$) are convenient to analyze using the variables $\mathbf{J} \equiv (J_f, L)$, $J_f = I_1 + I_2/2$, and $L = I_2$, where $(I_1, I_2) \equiv \mathbf{I}$ are the standard actions (Lynden-Bell 1979). The angular variables corresponding to $\mathbf{I}$ are $\mathbf{w} \equiv (w_1, w_2)$. The variables $\mathbf{J}$ are also the actions for which $\bar{\mathbf{w}} \equiv (\bar{w}_1, \bar{w}_2) = (w_1, w_2 - w_1/2)$ are the canonically conjugate angles. It can then be easily shown that in an unperturbed disk, $\bar{w}_2^{(0)} = \Omega_{\rm pr}(\mathbf{J})t$, where t is the time; $\Omega_{\rm pr}(\mathbf{J}) = \Omega_2(\mathbf{J}) - \Omega_1(\mathbf{J})/2$ is the angular velocity of the precession of an orbit with the actions $\mathbf{J}$; Ω_1 and Ω_2 are the frequencies of the radial and azimuthal stellar oscillations, respectively: $\Omega_i \equiv \partial E(\mathbf{I})/\partial I_i$ $(i = 1, 2)$; E is the stellar energy. Thus, $\bar{w}_2$ is a slow variable if $|\Omega_{\rm pr}| \ll |\Omega_1|, |\Omega_2|$.

Let us write the total potential $\Phi_{\rm tot}$ and distribution function $\mathcal{F}_{\rm tot}$ that describe the low-frequency mode as a sum of the unperturbed and perturbed parts:

$$\Phi_{\rm tot} = \Phi_0(\mathbf{J}) + \Phi(\mathbf{J}, \bar{w}_1)e^{im\bar{w}_2}, \qquad (2)$$
$$\mathcal{F}_{\rm tot} = \mathcal{F}_0 + \mathcal{F}(\mathbf{J}, \bar{w}_1)e^{im\bar{w}_2}.$$

As Polyachenko (1992) showed, the low-frequency disk modes then obey the following simple integral equation for the average potential:

$$\bar{\Phi} = \frac{1}{2\pi}\int_0^{2\pi} \mathrm{d}\bar{w}_1 \Phi(\mathbf{J}, \bar{w}_1).$$

Using the relation between $\bar{\Phi}$ and the average perturbed distribution function (Polyachenko 1992; Polyachenko and Polyachenko 2002, 2003),

$$\bar{\mathcal{F}} = -\mathcal{F}_0' \frac{\bar{\Phi}}{\Omega_{\rm p} - \Omega_{\rm pr}(\mathbf{J})}, \qquad (3)$$

where $\mathcal{F}_0' \equiv \partial\mathcal{F}_0(J_f, L)/\partial L$, we may rewrite the integral equation in the form of a classical eigenvalue problem; the eigenvalues are the angular velocities $\Omega_{\rm p}$ of the modes:

$$\Omega_{\rm p}\bar{\mathcal{F}}(\mathbf{J}) = \int d\mathbf{J}' K(\mathbf{J}, \mathbf{J}')\bar{\mathcal{F}}(\mathbf{J}'). \qquad (4)$$

Here, the kernel is

$$K(\mathbf{J}, \mathbf{J}') = \frac{G}{2\pi}\mathcal{F}_0'(\mathbf{J})\Pi(\mathbf{J}, \mathbf{J}') + \Omega_{\rm pr}(\mathbf{J})\delta[\mathbf{J} - \mathbf{J}'], \qquad (5)$$

where G is the gravitational constant,

$$\Pi(\mathbf{J}, \mathbf{J}') = \int d\bar{w}_1 d\bar{w}_1' d\delta\bar{w}_2 \frac{e^{im\delta\bar{w}_2}}{r_{12}}, \qquad (6)$$

$r_{12} = [r^2 + r'^2 - 2rr'\cos\delta\varphi]^{1/2}$, $\delta\bar{w}_2 \equiv \bar{w}_2' - \bar{w}_2$, $\delta\varphi \equiv \varphi' - \varphi$. When calculating the integral in (6), the quantities r, r', and $\delta\bar{w}_2 - \delta\varphi$ should be expressed in terms of $\mathbf{J}$, $\mathbf{J}'$, $\bar{w}_1$, and $\bar{w}_1'$.

Below, Eq. (4) is called the basic integral equation of the proposed theory of the formation of galactic structures. It is much simpler than the general integral equations for normal disk modes derived previously by Kalnajs (1965) and Shu (1970). The power of an ordinary personal computer is enough to solve Eq. (4).

GENERAL ANSLYSIS OF THE MASTER INTEGRAL EQUATION

The function Π defined by (6) can be transformed to

$$\Pi(\mathbf{J}, \mathbf{J}') = 8\int_0^\pi d\bar{w}_1 \cos m\varphi_1 \int_0^\pi d\bar{w}_1' \cos m\varphi_1' \psi(r, r'), \qquad (7)$$

where $\varphi_1(\mathbf{J}, \bar{w}_1) = \bar{w}_2 - \varphi$, $\varphi_1'(\mathbf{J}', \bar{w}_1') = \bar{w}_2' - \varphi'$,

$$\psi(r, r') = \int_0^\pi d\alpha \frac{\cos m\alpha}{\sqrt{r^2 + r'^2 - 2rr'\cos\alpha}}. \qquad (8)$$

It is clear from Eq. (7) that Π is a real and symmetric function: $\Pi(\mathbf{J}, \mathbf{J}')^* = \Pi(\mathbf{J}, \mathbf{J}')$, $\Pi(\mathbf{J}, \mathbf{J}') = \Pi(\mathbf{J}', \mathbf{J})$. It follows from Eq. (3) that $\bar{\mathcal{F}} \propto \mathcal{F}_0'$; therefore, both sides of Eq. (4) may be divided by $\mathcal{F}_0'$, multiplied by $\bar{\mathcal{F}}^*$, and integrated over $\mathbf{J}$. Calculating the imaginary part of the resulting equation, we obtain

$$(\mathrm{Im}\Omega_{\rm p})L_m = 0, \qquad (9)$$

where L_m is the angular momentum (or, to be more precise, the quasi-momentum; see McIntair (1981)) of the mode, which can be derived from the general

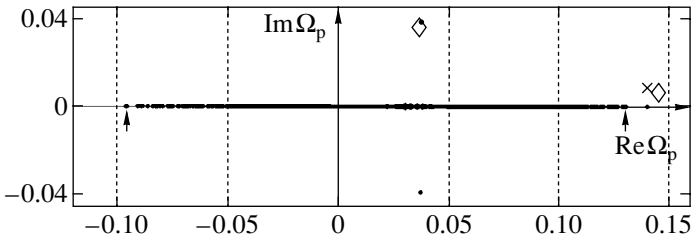

Fig. 1. Spectrum of the complex angular velocities of the modes (dots) calculated as the eigenvalues of problem (4) for the model ($m = 6$, $\beta = 3$, $q = 1$, $J_c = 0.6$) by Athanassoula and Selwood (1986). The cross denotes the theoretical complex angular velocity of the bar where the growth rate was estimated using formula (11). The diamonds denote the experimental complex angular velocities obtained from N-body simulations. The arrows indicate the minimum and maximum angular precession velocities of the stars.

formula by Lynden-Bell and Kalnajs (1972) by retaining the only term that dominates for low-frequency modes:

$$L_m = -\int d\mathbf{J}\frac{|\bar{\mathcal{F}}|^2}{\mathcal{F}_0'} = -\int d\mathbf{J}\mathcal{F}_0'\frac{|\bar{\Phi}|^2}{|\Omega_\mathrm{p}-\Omega_\mathrm{pr}|^2}. \quad (10)$$

The latter equality can be derived using relation (3) between $\bar{\mathcal{F}}$ and the average potential $\bar{\Phi}$ of the mode.

It turns out that the type of the solution of the basic integral equation depends crucially on the behavior of the derivative $\mathcal{F}_0'$. Below, we call it the Lynden-Bell derivative of the distribution function.[1] Consider the following two cases.

(1) Let us assume that $\mathcal{F}_0'$ is strictly positive everywhere in the phase space of the system. L_m is then negative, as is the energy (to be more precise, the quasi-energy) E_m of the mode, because $E_m = \Omega_\mathrm{p}L_m$ (Lynden-Bell and Kalnajs 1972). Therefore, we obtain $\mathrm{Im}\Omega_\mathrm{p} = 0$ from Eq. (9). The corresponding eigenfunctions $\bar{\mathcal{F}}$ are real and describe the nonspiral solutions, i.e., bars.

Clearly, in our case where $\mathcal{F}_0' > 0$, the integral equation (4) defines only the angular velocity of the mode $\mathrm{Re}\Omega_\mathrm{p}$. It grows due to the angular momentum exchange with resonance stars at the corotation radius (CR) and at the outer Lindblad resonance (OLR). We emphasize that this exchange is directly driven by the long-range gravitational field of the bar mode.

Let us now estimate the corresponding growth rate of the mode using the formula $\gamma = \dot{L}_m/2L_m$, where $\dot{L}_m = \dot{L}_m^{(1)} + \dot{L}_m^{(2)}$, and take the expressions for the rate of angular momentum exchange at the CR ($\dot{L}_m^{(1)}$) and OLR ($\dot{L}_m^{(2)}$) from the general formulas by Lynden-Bell and Kalnajs (1972) by slightly transforming them:

$$\dot{L}_m^{(l)} = -\frac{1}{4\pi}\int\left(\frac{l}{2}\frac{\partial\mathcal{F}_0}{\partial J_f} + \frac{\partial\mathcal{F}_0}{\partial L}\right) \times |\Psi_l|^2\delta[\Omega^{(l)}(\mathbf{J}) - \Omega_\mathrm{p}]d\mathbf{J}, \quad (11)$$

where $\Omega^{(l)}(\mathbf{J}) \equiv \Omega_2(\mathbf{J}) + (l-1)\Omega_1(\mathbf{J})/2$, and Ψ_l are the Fourier coefficients corresponding to the CR ($l = 1$) and OLR ($l = 2$) in the expansion of the perturbed potential in terms of $e^{il\bar{w}_1}$

$$\Phi(\mathbf{J}, \bar{w}_1) = \sum_l \Psi_l(\mathbf{J})e^{il\bar{w}_1}. \quad (12)$$

Our estimate of the growth rate may be considered only as a first, rough approximation. Thus, Ψ_l in formula (11) is generally the Fourier transform of the total perturbed potential, which, apart from the bar potential, includes the potential of the spiral density wave generated at the resonance (see, e.g., Goldreich and Tremaine 1979). In addition, when calculating the growth rate, the components of the potential that were not included in the principal order of the perturbation theory may prove to be significant. These issues will be discussed in more detail in another paper.

The interaction of stars in resonance regions with the gravitational potential of the mode leads to spiral responses (see, e.g., Polyachenko 2002a, 2002b). Therefore, the perturbation pattern in the entire disk consists of the bar and the adjacent spiral arms, which is what we observe in actual SB galaxies.

(2) Let us now assume that $\mathcal{F}_0'$ is negative in some of the regions of the phase space. It can be shown that for realistic distribution functions, these regions, if they exist, can occupy only a small fraction of the total phase volume. In this case, in addition to the bars considered above, unstable spiral solutions can also appear. In contrast to the bars, these new modes grow due to the internal instability inherent in the

[1] When analyzing slow bars, Lynden-Bell (1979) considered a similar derivative of the angular precession velocity $\partial\Omega_\mathrm{pr}/\partial L$ for stars.

mode itself. As follows from Eq. (9), the angular momentum $L_m = 0$ for an unstable mode ($\mathrm{Im}\Omega_\mathrm{p} > 0$); i.e., the contributions from the regions with opposite signs of the Lynden-Bell derivative $\mathcal{F}_0'$ to L_m cancel each other out: $L_m = L^+ + L^- = 0$. Accordingly, the growth rate of the unstable mode can be estimated as

$$\gamma = \frac{\dot{L}^+}{2L^+} = \frac{\dot{L}^-}{2L^-}, \qquad (13)$$

$$\dot{L}_\pm = -\frac{1}{4\pi}\int\limits_{\Gamma_\pm} \mathcal{F}_0'|\bar{\Phi}|^2\delta[\Omega_\mathrm{pr}(\mathbf{J}) - \Omega_\mathrm{p}]d\mathbf{J},$$

Γ_+ and Γ_- denote the regions of the phase space with positive and negative Lynden-Bell derivatives $\mathcal{F}_0'$, respectively.

The instability criterion $\mathcal{F}_0' < 0$ is the growth condition for a negative-energy wave at the inner Lindblad resonance (ILR), which actually is contained in the general results by Lynden-Bell and Kalnajs (1972). The difference is that Lynden-Bell and Kalnajs assumed $\mathcal{F}_0'$ to be positive throughout the phase space and, therefore, their waves must have been damped out at the ILR.

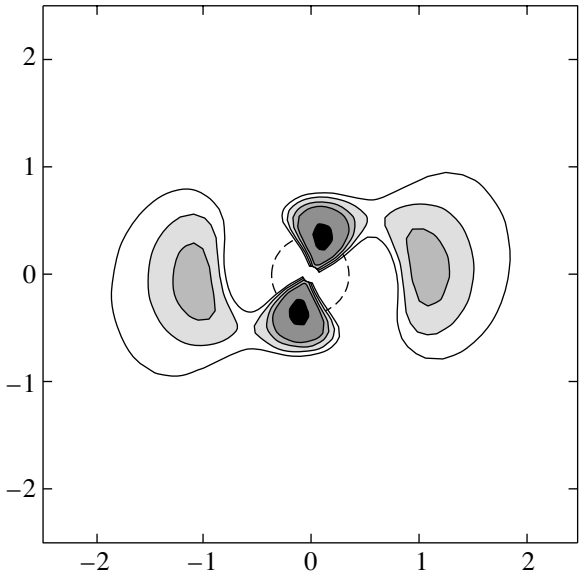

Fig. 2. Qualitative pattern of the surface density of a spiral unstable mode for the model ($m = 6$, $\beta = 3$, $q = 1$, $J_c = 0.6$) by Athanassoula and Selwood (1986). Higher spiral densities correspond to darker regions. The dashed circumference indicates the position of the inner ILR (the outer ILR for this model is located at $r = 5$).

NUMERICAL SOLUTIONS OF THE MASTER INTEGRAL EQUATION

We tested the theory using test models. The basic integral equation (4) was solved numerically. The unknown function $\bar{\mathcal{F}}(\mathbf{J})$ and the kernel $K(\mathbf{J}, \mathbf{J}')$ were considered on a 31×31 grid in phase space (E, L). The resulting matrix equation can then be solved using the standard methods of linear algebra.

We computed a total of about ten models that were previously analyzed by Athanassoula and Selwood (1986) using N-body simulations. In all cases, the results of our calculations are in satisfactory agreement: the angular velocities of the modes are determined with an accuracy better than 10%. As an example, let us consider in more detail the model with $m = 6$, $\beta = 3$, $q = 1$, and $J_c = 0.6$,[2] which has both barlike and spiral modes. The equilibrium potential of the model is $\Phi_0(r) = -(1 + r^2)^{-1/2}$. Figure 1 shows the eigenvalue spectrum of the bisymmetric modes for this model inferred from the solution of Eq. (4). We see that the spectrum contains continuous and discrete parts.

The continuous spectrum is located in the interval between the minimum and maximum angular precession velocities: $(-0.096, 0.13)$. Below, however, we are interested only in the modes of the discrete spectrum. Note that the observed structures in the N-body simulations by Athanassoula and Selwood (1986) were always determined by these modes.

Since the Lynden-Bell derivative is not everywhere positive in the phase space for the model under consideration, the discrete spectrum contains complex frequencies. In Fig. 1, we see one unstable complex eigenfrequency and one real eigenfrequency that belong to the discrete spectrum. The complex eigenfrequency derived from the solution of the basic integral equation is very close to the experimental frequency given by Athanassoula and Selwood (1986). Figure 2 shows the perturbed surface density of the spiral mode.

The angular velocity of the bar mode is equal to the value obtained in the N-body simulations with an accuracy of 3%. Its growth rate was roughly estimated to be $\gamma = 0.018$ by assuming that the orbits were almost circular. This estimate is only 30% larger than that obtained by Athanassoula and Selwood in their N-body simulations.

DISCUSSION

The bar formation mechanism suggested above imposes a natural constraint on the angular velocity of the bar modes: $\Omega_\mathrm{p} > (\Omega_\mathrm{pr})_\mathrm{max}$. Otherwise, the inner Lindblad resonances at which the mode must be damped out (at $\mathcal{F}_0' > 0$) appear. The excess of Ω_p above $(\Omega_\mathrm{pr})_\mathrm{max}$ is provided by self-gravitation;

[2]Here, we use the notation adopted by Athanassoula and Selwood (1986).

i.e., bars can be formed only in galaxies with high-mass disks. If, however, the disk mass is low, then, as follows from specific numerical calculations, only the continuous eigenvalue spectrum exists at $\mathcal{F}_0' > 0$, while an unstable spiral mode emerges in the presence of a region with negative $\mathcal{F}_0'$. Note that the inequality $\Omega_p > (\Omega_{pr})_{max}$ is difficult to satisfy not only for low-mass disks, but also for disks with a high central mass concentration.

Clearly, the bar mode of the type under consideration is formed through the azimuthal adjustment of the orbits. The admissible frequency (angular velocity) of the galactic bar is one of the eigenvalues of the basic integral equation. This implies that the corresponding waves remain unchanged over many rotations of the galaxy, although the orbits precess at different angular velocities. The mode grows due to the resonance exchange of angular momentum with the stars at the corotation and outer Lindblad resonances. The half-turn spirals adjacent to the bar are also formed through resonance interaction.

The eigenfrequencies of all modes obtained previously by Athanassoula and Selwood (1986) in their N-body simulations can be accurately calculated using the suggested new approach. In the long run, precisely this justifies the hypothesis about the effective low-frequency nature of the galactic modes formulated above and their formation mechanism that follows from it.

Athanassoula and Selwood (1986) overlooked the simple possibility of explaining the growth of modes through resonance interaction (although they calculated many bar modes and could easily estimate their growth rates). Instead, they switched to the language of swing amplification with the concepts of local growth rate, waves traveling in the galaxy inward and outward with radius-dependent group velocities, etc. (Toomre 1981; Binney and Tremain 1987; Bertin and Lin 1996). In essence, this was an attempt to use a clearly inadequate language to describe global modes.

The formation mechanism of the structures observed in normal spiral galaxies is usually interpreted using either swing amplification (Toomre 1981) or superreflection (see, e.g., Bertin and Lin 1996). The corotation region plays the central role in these mechanisms. In the suggested approach, the spiral perturbations are unstable waves with zero total angular momentum. Such waves can exist only in the presence of regions with a negative Lynden-Bell derivative, $\mathcal{F}_0' < 0$. As we pointed out at the end of the section General Analysis of the Master Integral Equation, $\mathcal{F}_0' < 0$ is the condition for the growth of a negative-energy wave at the inner Lindblad resonance. A more detailed discussion of the spiral modes will be given in a separate paper.

ACKNOWLEDGMENTS

I am grateful to V.L. Polyachenko for his helpful discussions. This work was supported by the Russian Science Support Foundation, the Russian Foundation for Basic Research (project no. 02-02-16878), and the Ministry of Industry and Science (the Leading Scientific Schools project no. NSh 925.2003.2 and the State Contracts nos. 40.022.1.1.1101 and 40.020.1.1.1167.IA.1).

REFERENCES

1. E. Athanassoula and J. Sellwood, Mon. Not. R. Astron. Soc. **221**, 213 (1986).
2. G. Bertin and C. C. Lin, *Spiral Structure in Galaxies* (MIT Press, Cambridge, 1996).
3. J. Binney and S. Tremaine, *Galactic Dynamics* (Princeton Univ. Press, Princeton, 1987).
4. P. Goldreich and S. Tremaine, Astrophys. J. **233**, 857 (1979).
5. A. J. Kalnajs, Ph.D. Thesis (Harvard Univ. Press, 1965).
6. C. C. Lin, C. Yuan, and F. H. Shu, Astrophys. J. **155**, 721 (1969).
7. D. Lynden-Bell, Mon. Not. R. Astron. Soc. **187**, 101 (1979).
8. D. Lynden-Bell and A. J. Kalnajs, Mon. Not. R. Astron. Soc. **157**, 1 (1972).
9. M. McIntair, J. Fluid Mech. **106** (1981); *A Special Issue Celebrating the 25th Anniversary of the Journal,* Ed. by G. Batchalor and H. Moffat (Cambridge Univ. Press, Cambridge, 1981; Mir, Moscow, 1984).
10. V. L. Polyachenko, Zh. Éksp. Teor. Fiz. **101**, 1409 (1992) [Sov. Phys. JETP **74**, 755 (1992)].
11. E. V. Polyachenko, Mon. Not. R. Astron. Soc. **330**, 105 (2002a).
12. E. V. Polyachenko, Mon. Not. R. Astron. Soc. **331**, 394 (2002b).
13. E. V. Polyachenko and V. L. Polyachenko, astro-ph/0212553 (2002).
14. E. V. Polyachenko and V. L. Polyachenko, Pis'ma Astron. Zh. **29**, 508 (2003) [Astron. Lett. **29**, 447 (2003)].
15. F. H. Shu, Astrophys. J. **160**, 89 (1970).
16. A. Toomre, *Structure and Evolution of Normal Galaxies,* Ed. by S. M. Fall and D. Lynden-Bell (Cambridge Univ. Press, Cambridge, 1981), p. 111.

Translated by A. Dambis

Astronomy Letters, Vol. 30, No. 8, 2004, pp. 519–526. Translated from Pis'ma v Astronomicheskiĭ Zhurnal, Vol. 30, No. 8, 2004, pp. 574–581.

UGC 5119: A Galaxy with a Stellar Polar Ring?

V. A. Yakovleva and G. M. Karataeva*

St. Petersburg State University, Universitetskii pr. 28, Petrodvorets, 198504 Russia

Received January 19, 2004

Abstract—We present our photometric BVR_c observations of UGC 5119, a candidate polar-ring galaxy. We have determined its absolute magnitude, $M_{0,B} = -20\overset{m}{.}3$, and total color indices, $(B-V)^0_t = +0\overset{m}{.}73 \pm 0\overset{m}{.}10$ and $(V-R_c)^0_t = +0\overset{m}{.}54 \pm 0\overset{m}{.}10$. A Fourier analysis of the shape of its isophotes shows that UGC 5119 is most likely an elliptical galaxy with a disk component in the central part and a "boxy" feature on the periphery. At distances larger than $8''$, the galaxy exhibits a turn of its major axis and a change in the phase of the fourth harmonic. Assuming the position angle of the major axis to be constant, a stellar ringlike structure is distinguished in the galaxy. The age of the ring stars is the same as that of the stars in the host galaxy. The distinguished ringlike structure cannot be attributed to typical polar rings rich in gas and in young stars. © *2004 MAIK "Nauka/Interperiodica"*.

Key words: *galaxies, peculiar galaxies, UGC 5119.*

INTRODUCTION

The galaxy no. 5119 in the UGC catalog is listed as peculiar. Its B-band image obtained with the 6-m Special Astrophysical Observatory (SAO) telescope is shown in Fig. 1. As we see from this figure, the central region of UGC 5119 resembles an elliptical or S0 galaxy, while its outer parts have an almost square shape. Although this is a rather bright galaxy (according to RC3, its total magnitude is $m_B^T = 14\overset{m}{.}48$), the data on it are very scarce. In the catalog of polar-ring galaxies (PRGs) by Whitmore *et al.* (1990), UGC 5119 was included in group B of the most probable candidates, because the boxy shape of the object's outer isophotes can be explained by the presence of a polar ring whose size is approximately equal to the size of the galaxy's major axis.

As a PRG candidate, UGC 5119 has been studied spectroscopically (Reshetnikov and Combes 1994) and included in radio surveys (Huchtmeier 1997; van Driel *et al.* 2000). Reshetnikov and Combes (1994) pointed out that a strong absorption line is superimposed on the Hα emission. A low 21-cm flux of $\sim$7 Jy km s^{-1} was recorded from the galaxy with the Effelsberg 100-m radio telescope (Huchtmeier 1997), but this result was not confirmed in a repeat survey with a different instrument (van Driel *et al.* 2000).

Since the mid-1990s, photometric and spectroscopic studies of PRGs and PRG candidates have been carried out at the Astronomical Institute of St. Petersburg State University. The peculiar galaxy UGC 5119 was included in this program.

To estimate the distance to the galaxy, we used a heliocentric velocity of 6037 km s^{-1} (Reshetnikov and Combes 1994). For $H_0 = 65$ km s^{-1}Mpc^{-1}, this distance is 93 Mpc, which yields a scale of 0.45 kpc in $1''$.

OBSERVATIONS AND REDUCTION

Our photometric observations of the galaxy UGC 5119 were performed with the 6-m SAO telescope in Johnson's B and V bands and Cousins' R_c band. The observational material is given in Table 1. In all cases, the seeing was about $2''$.

The detector was a Photometrix 1024×1024 CCD array with a readout noise of $6e^-$. The angular pixel size was $0''.2 \times 0''.2$, and the field of view was $3'.6 \times 3'.6$. During each night, standard stars from the lists by Landolt (1983) were observed for calibration purposes. When correcting the data for atmospheric extinction, we used the mean transparency coefficients for SAO.

We reduced the observations using the ESO-MIDAS and IRAF software packages.

RESULTS

General Photometric Characteristics

Figure 2 shows the galaxy's isophotes in the B, V, and R_c color bands. Since the isophotes have a similar shape in all colors, we may consider its changes

*E-mail: narka@astro.spbu.ru

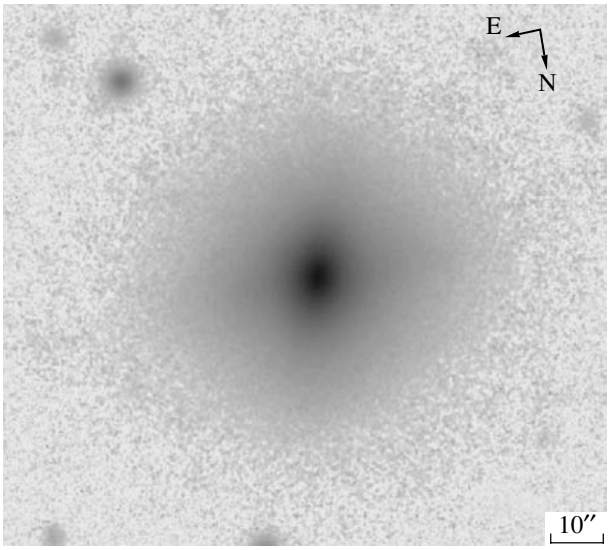

Fig. 1. Reproduction of the galaxy UGC 5119 in the B band.

with distance using the B band as an example. The isophotes in the central region are elliptical in shape, but beginning from the 22.5 mag/□″ isophote, protrusions appear in the E–W direction. This feature led Whitmore *et al.* (1990) to suspect the presence of a polar ring. As we pass to fainter isophotes, their shape becomes almost square. One of the diagonals of this figure coincides with the direction of the galaxy's major axis (PA = 12°), while the other diagonal runs at an angle of about 78° to it. Note that a star is projected onto the galaxy's body at a distance of ≈ 21″ to the west of the center; this star is clearly seen in the V and R_c images and distorts the shape of the isophotes at this location.

Table 1. Observational material

Date	Band	Exposure time, s	z, deg
Jan. 22, 1999	R_c	50	7
	B	100	7
	V	80	8
	R_c	50	9
	B	300	10
	V	150	12
Jan. 24, 1999	R_c	50	8
	B	300	8
	V	200	6

Figure 3 shows photometric profiles along the galaxy's major axis (PA = 12°). A large brightness gradient is observed in the central region in all colors, while beginning from a distance of ≈10″, all of the profiles become flatter. The size of the galaxy's major axis at the $\mu_B = 26$ mag/□″ level is ∼64″, which corresponds to a linear size of ∼29 kpc. The profiles along the major axis of the presumed ring differ from those along the major axis of the galaxy, first, by a steeper brightness gradient in the central region, and, second, by more extended flat wings. The diameter of the presumed ring at the $\mu_B = 26$ mag/□″ level reaches 70″ (32 kpc).

The total apparent magnitudes of the galaxy were determined using multi-aperture photometry. It was found that the curve of brightness rise in B at small radii coincides with the standard RC3 curves for S0 galaxies ($T = -1$) and runs slightly above these curves as the radius increases, which is undoubtedly attributable to the shape of the outer isophotes. Therefore, there is uncertainty in the estimate of the total magnitude; the apparent B magnitude can be brighter by several hundredths. We adopted the following total magnitudes: $B_t = 14^m.29 \pm 0^m.1$, $V_t = 13^m.55 \pm 0^m.1$, $R_{c,t} = 13^m.00 \pm 0^m.1$.

The total magnitudes corrected for the absorption in our Galaxy (Schlegel *et al.* 1998) are given in Table 2. Note that the $(B-V)_t^0$ color index is approximately $0^m.1$ bluer than the mean color index for S0 galaxies and differs even more strongly from the mean color indices for elliptical galaxies. The $(V-R_c)_t^0$ color index is close to the mean value for E–S0 galaxies.

Color Distributions

An analysis of the $B-V$ and $V-R_c$ color distributions shows that the $B-V$ maps are featureless, while structural features are clearly seen in the $V-R_c$ distribution (see Fig. 4). The difference in the behaviors of the color indices can be quantitatively estimated from the profiles along the major axes of the galaxy and the presumed ring shown in Fig. 5. As we see from this figure, the $B-V$ variations are small on both profiles and lie within $0^m.15$. The nuclear region is reddest (in the nucleus, $B-V = 0^m.82$). The color index slightly decreases in the outer parts of the galaxy. At a distance of 20″ from the center, $B-V \approx 0^m.7$. Our data reveal no decrease of the color index in the region of the presumed ring (Figs. 4, 5b).

In the $V-R_c$ distribution (Fig. 4), a roughly elliptical structure elongated along the galaxy's major axis is distinguished at the center. As we see from

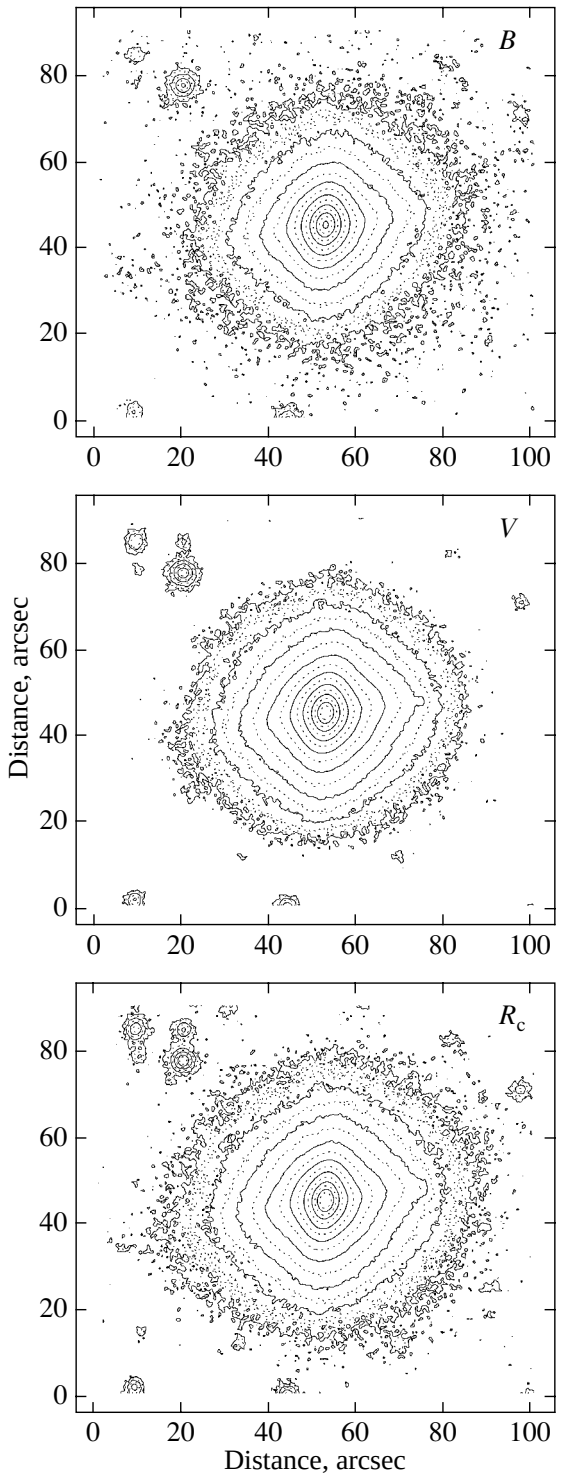

Fig. 2. Isophotes of UGC 5119 in the B, V, and R_c bands at 0.5 mag/□″ intervals. The ranges in B, V, and R_c are from 18.0 to 25.5 mag/□″, from 18.0 to 25.5 mag/□″, and from 17.5 to 25.0 mag/□″, respectively.

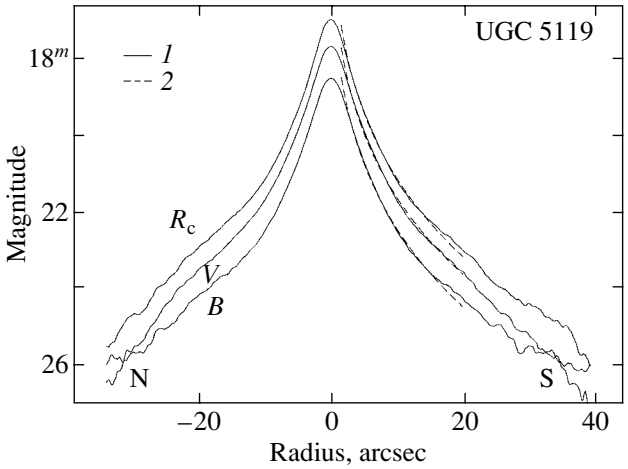

Fig. 3. Photometric profiles along the galaxy's major axis (*1*). The result of fitting the observed profile by the De Vaucouleurs law (*2*).

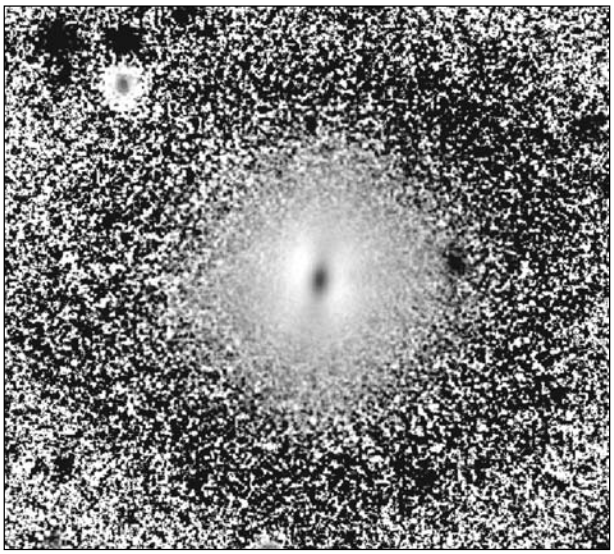

Fig. 4. $V-R_c$ color distribution in UGC 5119 (the larger the color index, the darker the image); the color index varies over the range $0^m.4$ to $0^m.8$.

Fig. 5, this is the reddest region. The color index is at a maximum in the nucleus ($V-R_c = 0^m.72$) and decreases with distance from it; a sharper change in color is observed in the east–west direction (Fig. 5b). The color index reaches its minimum, $0^m.4$, at a distance of ∼3″ from the center and then begins to slowly increase and reaches $B-R_c = 0^m.6$ at ∼ 20″ on both profiles. The regions at distances between 2″ and 4″ to the E and W of the nucleus are bluest in the $V-R_c$ color distribution (Figs. 4, 5b).

Data on the $B-R_c$ color index are often provided for elliptical galaxies (see, e.g., Franx *et al.* 1989; Peletier *et al.* 1990). Our values of this color index are approximately $0^m.2$ bluer than the mean values

Table 2. Basic parameters of UGC 5119

Distance	93 Mpc ($H_0 = 65$ km s^{-1}Mpc^{-1})
Scale	0.45 kpc in 1″
E_{B-V}	$0\overset{m}{.}014$
Morph. type	E2
B_t	$14\overset{m}{.}23 \pm 0\overset{m}{.}10$
$(B-V)^0_\mathrm{t}$	$+0\overset{m}{.}73 \pm 0\overset{m}{.}10$
$(V-R_\mathrm{c})^0_\mathrm{t}$	$+0\overset{m}{.}54 \pm 0\overset{m}{.}10$
Semimajor axis, a	32″ (14.5 kpc)
($\mu_B = 26.0$ mag/□″)	
PA of major axis	12°
$M_{0,B}$	$-20\overset{m}{.}3$
Bulge parameters	
μ^B_e	19.9 mag/□″
r^V_e	$3\overset{''}{.}5$ (1.6 kpc)
μ^V_e	19.3 mag/□″
r^B_e	$3\overset{''}{.}7$ (1.6 kpc)
μ^R_e	18.5 mag/□″
r^R_e	$3\overset{''}{.}4$ (1.5 kpc)
Semimajor axis of ring	70″ (32 kpc)
($\mu_B = 26.0$ mag/□″)	
PA of major axis of ring	78°
$(B-V)_\mathrm{ring}$	$0\overset{m}{.}7$
$(V-R_\mathrm{c})_\mathrm{ring}$	$0\overset{m}{.}5$

for E galaxies. In addition, no appreciable decrease of the color index is observed in the outer regions of UGC 5119.

ANALYSIS AND DISCUSSION

Consider the shape of the profiles along the galaxy's major axis (Fig. 3). A slight asymmetry is noticeable between the northern and southern parts of the profile, but, on average, their shape is satisfactorily represented by the de Vaucouleurs law. Our parameters of this expansion, the effective radius (r_e) and the corresponding surface brightness (μ_e), are given in Table 2. As we see from Fig. 3, where the dashed lines indicate the computed curves, there is a deviation from the $r^{1/4}$ law in the nuclear region ($|r| < 2''$) and in the outer parts of the galaxy ($|r| > 15''$). Since our frames were taken at moderately good seeing ($\sim 2''$), the shape of the profile in the nuclear region is smoothed. The observed data points in the outer parts lie above the theoretical curve, which may be indicative of the presence of a weak disk or a "boxy" feature.

To analyze the photometric structure of the galaxy, we used a technique suggested by Jedrzejewski (1987) that is based on the Fourier expansion of the deviations of isophotes from the elliptical shape. In the IRAF package, which we used for data reduction, the function $I(\vartheta)$ that represents the change in intensity along the ellipse with the major axis r fitted into the isophote is expanded into a Fourier series:

$$I(\vartheta) = I_0 + \sum_{n=1}^{\mathrm{k}} \left(A_n \cos(n\vartheta) + B_n \sin(n\vartheta)\right), \quad (1)$$

where the angle ϑ is reckoned from the major axis of the ellipse. The dimensionless parameters a_n and b_n that are related to A_n and B_n by the following relations are most commonly used to describe the shape of the isophotes:

$$a_n = A_n \Big/ \left(r \left|\frac{dI(r)}{dr}\right|\right), \quad (2)$$
$$b_n = B_n \Big/ \left(r \left|\frac{dI(r)}{dr}\right|\right).$$

As a result, we determined the following parameters for each semimajor axis: the ellipticity, the position angle of the major axis of the ellipse (PA) measured from the northward direction eastward, and the third and fourth harmonic coefficients. These data are shown in Fig. 6.

As we see from Fig. 6a, the ellipticity is constant up to $\sim 6''$ from the center and equal to 0.25±0.002 in the B and V bands and 0.28±0.003 in the R_c band. Farther out, it decreases in all bands to 0.1±0.007

($r \sim 10''-12''$) and, on average, does not change in the galaxy's outer regions, while the scatter of data points is probably attributable to an increase in the errors.

The variations in the position angle of the major axis of the ellipses (Fig. 6b) correlate with the ellipticity variations. In the central region ($0'' < r < 6''$), PA is constant and equal to $12° \pm 1°$; farther from the center, it changes and turns through $45° \pm 2°$ at a distance of $15''$ from the center.

Figures 6c and 6e show the behavior of the relative coefficients of $\cos(3\vartheta)$ and $\sin(3\vartheta)$, respectively. Within $10''$, both coefficients, $a3$ and $b3$, are equal to zero in all colors. Farther out, they differ slightly from zero, but their errors also increase. The behavior of $a4$ and $b4$ (Figs. 6d, 6f) is of greatest interest. The value and sign of the coefficient of the cosine of the fourth harmonic can reveal the presence of a disk or "boxy" component in elliptical galaxies. As we see from Figs. 6d and 6f, both coefficients are equal to zero in the central region; farther from the center, $a4$ increases sharply and reaches 0.04 ± 0.002 at a distance of $8''$, suggesting the presence of a disk component. Farther out, $a4$ decreases sharply and changes its sign. In the region from $12''$ to $22''$, $a4$ reaches its maximum negative value of -0.07 ± 0.004, suggesting a "boxy" shape of the isophotes in the outer parts of the galaxy.

The presence of dust is known to manifest itself in a difference between the third and fourth harmonic coefficients in the B and R_c bands; the third harmonic coefficients are more reliable indicators of the presence of even small amounts of dust than the total color indices (Peletier *et al.* 1990). In our case, the coefficients of the third harmonic and $b4$ are equal in the B and R_c bands; $a4$ in R_c is larger than its value in B by 0.005 only in the central region of the galaxy. This galaxy probably contains very little dust. This is also suggested by its relatively blue total color index $(B-V)_t^0 = 0^m.75$.

In conclusion, let us consider the peculiarity in the variations of the fourth harmonic coefficients observed for UGC 5119. It is commonly assumed that a positive coefficient of $\cos(4\vartheta)$ suggests the presence of a weak disk (see, e.g., Jedrzejewski 1987; Bender and Möllenhoff 1987), while a negative coefficient is indicative of a "boxy" feature that may be related to the triaxial shape of the galaxy's potential (see, e.g., Benney and Petrou 1985). However, as Franx *et al.* (1989) pointed out, if a turn of the galaxy's major axis and a change in the phase of the fourth harmonic are observed, then caution should be exercised in explaining the origin of "boxy" features. The effects of the projection and mutual orientation of the galaxy's disk and main body can play a significant role

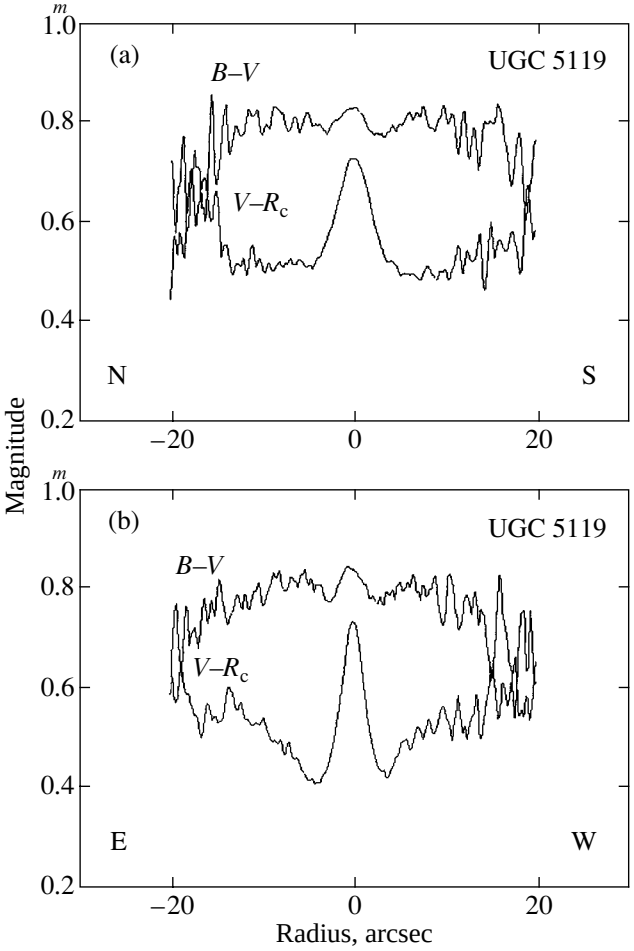

Fig. 5. Variations of the color indices along the galaxy's major axis (a) and along the presumed ring (b).

in this case. For the galaxy UGC 5119, we observe just a turn of the major axis by $\sim 45°$. In addition, as we see from Fig. 6c, the coefficient of $\sin(4\vartheta)$ varies and reaches -0.06 ± 0.003 at a distance of $11''$. This implies that the phase of the fourth harmonic changes with distance. The amplitudes and phases of the fourth harmonic are shown in Fig. 7, where the phase is reckoned from the major axis of the ellipse. The amplitude of the fourth harmonic exceeds 0.04 in the region from $8''$ to $25''$, a rapid change in the phase and a turn of PA of the galaxy's major axis also take place here (Fig. 6b). A plausible explanation of the observed feature is the presence of two components: the host galaxy with a constant position angle of its major axis (PA = 12°) and a ringlike structure at an angle of $\approx 80°$ to the galaxy's major axis. To test this hypothesis, we attempted to distinguish the second component. To this end, in each band, we calculated the difference between the observed bright-

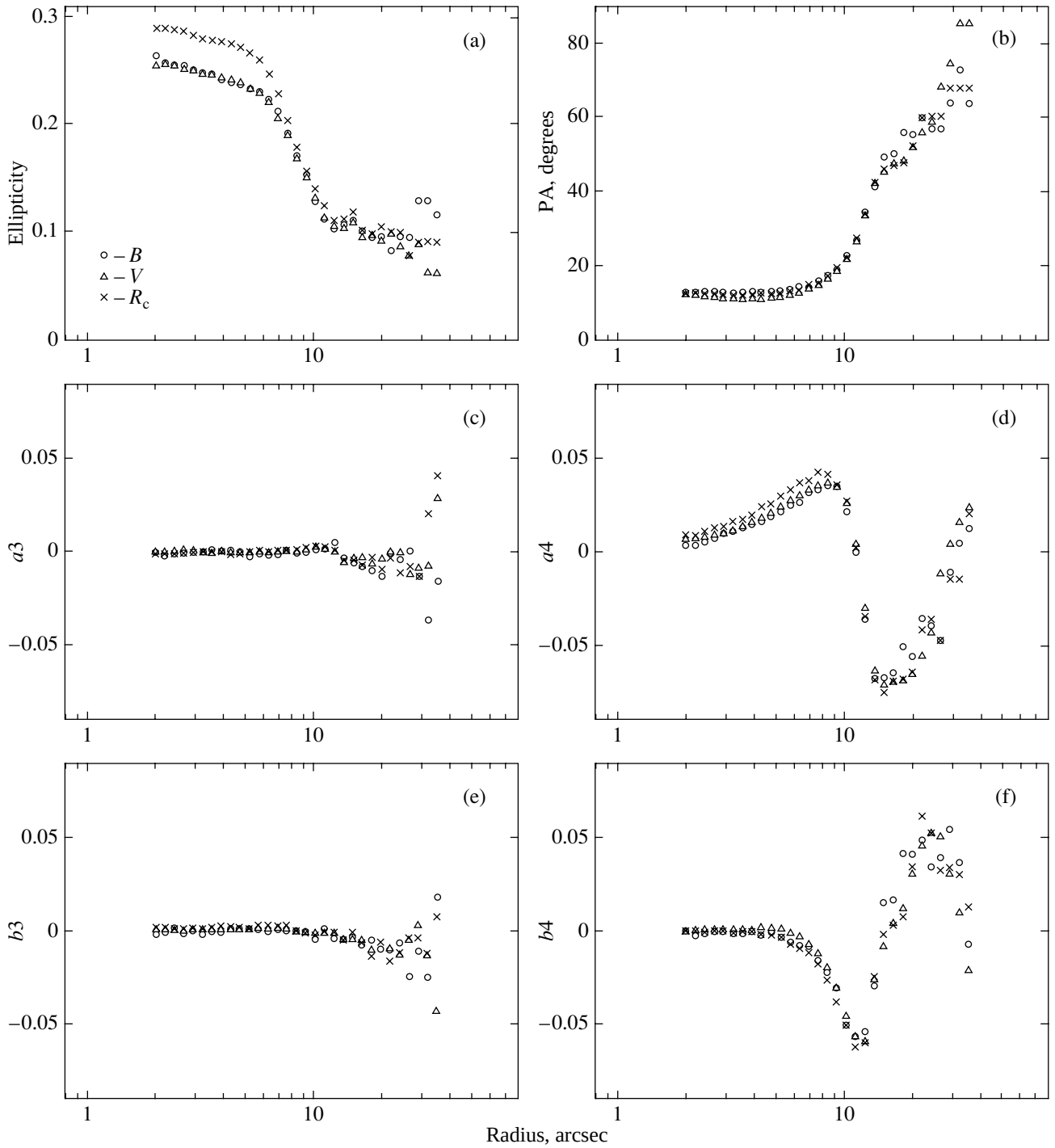

Fig. 6. Parameters of the isophote shape versus semimajor axis of the ellipse fitted into the isophote: ellipticity (a), position angle (b), and third and fourth harmonic coefficients ($a3$, $a4$, $b3$, $b4$) (c–f).

ness distribution and the brightness distribution in the bulge whose parameters were determined above. Figure 8 shows the B-band brightness distribution in the residual image. The second component, which is most likely ring-shaped, is clearly distinguished. A similar picture is also observed in other bands. The mean color indices of the ring, $(B-V)_{\rm ring} \approx 0\overset{m}{.}7$ and $(V-R_c)_{\rm ring} \approx 0\overset{m}{.}5$, are close to the color indices of the outer parts of the host galaxy. Consequently, the stellar populations of the ringlike structure and the

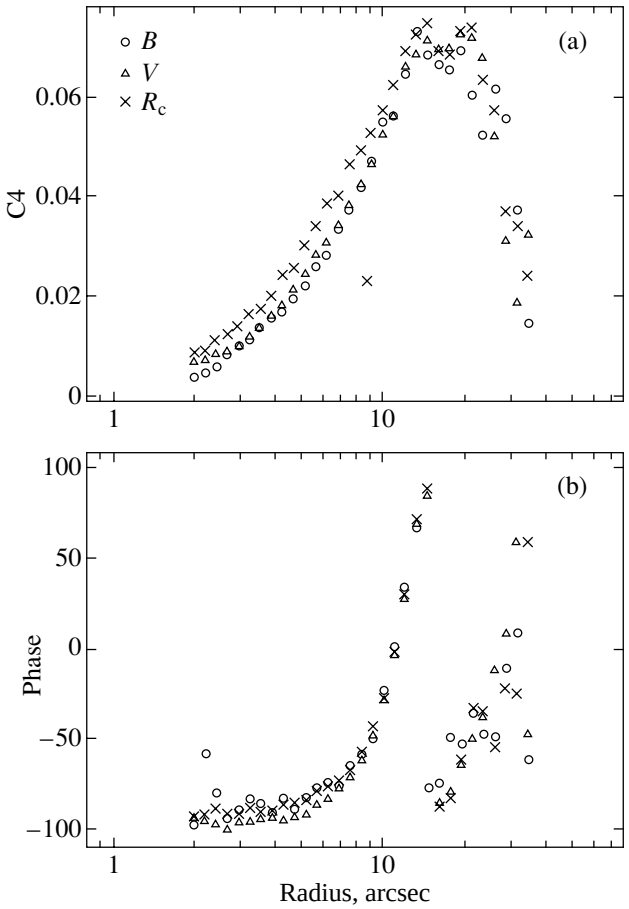

Fig. 7. Amplitude (a) and phase (b) of the fourth harmonic. The phase is reckoned from the major axis of the ellipse fitted into the isophote.

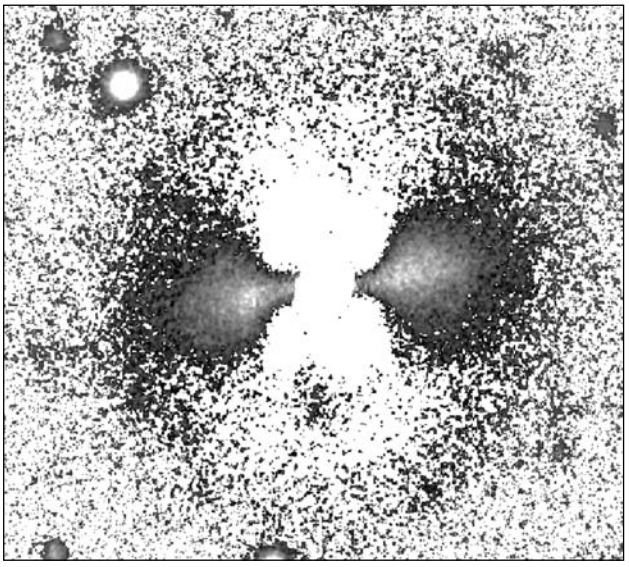

Fig. 8. B-band brightness distribution after the subtraction of the bulge. The shades from gray to black correspond to the change in brightness from 24.0 to 26 mag/□″.

galaxy are approximately of the same age. A similar result was obtained for the galaxy NGC 1700 by Franx *et al.* (1989).

CONCLUSIONS

Our photometric study has shown that UGC 5119 is probably an E2 elliptical galaxy. Its total parameters are consistent with this conclusion, although the color index $(B-V)_t^0$ is bluer than the mean values for E galaxies by $0^m.2$. A Fourier analysis of the isophote shape revealed a weak disk component in the region from 6″ to 10″ and a "boxy" feature in the outer parts of the galaxy, a turn of PA of the major axis and a change in the phase of the fourth harmonic. If the position angle of the major axis of the host galaxy is assumed to be constant, then a second ringlike component is distinguished in the east–west direction from the nucleus. The angle between the major axes of the components is about 80°. The coincidence between the color indices of the ring and the host galaxy suggests that their stellar populations are of the same age. The ringlike feature could originate from the capture of a dwarf elliptical galaxy. Reshetnikov and Sotnikova (2000) showed that a ringlike stellar structure could be formed at early destruction stages of the companion. However, a special flyby geometry is needed for a polar ring to emerge. The nature of the two bluer regions in the $V-R_c$ color distribution is not yet clear. These features may be assumed to also have resulted from the collision of galaxies. As regards the presence of the polar ring suspected by Whitmore *et al.* (1990), it should be emphasized that the ringlike structure we found is not a typical polar ring. As was noted in several papers (see, e.g., Reshetnikov and Sotnikova 1997; Karataeva *et al.* 2004), polar rings are rich in gas, intense star formation occurs in them, and they have many young stars.

It will be possible to reach ultimate conclusions about the nature of this object after obtaining spectroscopic data and analyzing the behavior of the radial velocities and velocity dispersion.

ACKNOWLEDGMENTS

We are grateful to the 6-m telescope committee for allocating observational time on the telescope and to the staff of the SAO for help in the observations. We wish to thank N.Ya. Sotnikova for her helpful discussions. This study was supported in part by the federal Astronomy program (40.022.1.1.1001) and the Russian Foundation for Basic Research (project no. 02-02-16033).

REFERENCES

1. R. Bender and C. Möllenhoff, Astron. Astrophys. **177**, 71 (1987).
2. J. Benney and M. Petrou, Mon. Not. R. Astron. Soc. **214**, 449 (1985).
3. W. van Driel, M. Arnaboldi, F. Combes, and L. S. Sparke, Astron. Astrophys., Suppl. Ser. **141**, 385 (2000).
4. M. Franx, G. Illingworth, and T. Heckman, Astron. J. **98**, 538 (1989).
5. W. K. Huchtmeier, Astron. Astrophys. **319**, 401 (1997).
6. R. Jedrzejewski, Mon. Not. R. Astron. Soc. **226**, 747 (1987).
7. G. M. Karataeva, I. O. Drozdovsky, V. A. Hagen-Thorn, *et al.*, Astron. J. **127**, 789 (2004).
8. A. U. Landolt, Astron. J. **88**, 439 (1983).
9. R. F. Peletier, R. L. Davies, G. Illingworth, *et al.*, Astron. J. **100**, 1091 (1990).
10. V. Reshetnikov and F. Combes, Astron. Astrophys. **291**, 57 (1994).
11. V. Reshetnikov and N. Sotnikova, Astron. Astrophys. **325**, 933 (1997).
12. V. P. Reshetnikov and N. Ya. Sotnikova, Pis'ma Astron. Zh. **26**, 333 (2000) [Astron. Lett. **26**, 277 (2000)].
13. D. J. Schlegel, D. P. Finkbeiner, and M. Davis, Astrophys. J. **500**, 525 (1998).
14. B. C. Whitmore, R. A. Lucas, D. B. McElroy, *et al.*, Astron. J. **100**, 1489 (1990).

Translated by N. Samus'

Astronomy Letters, Vol. 30, No. 8, 2004, pp. 527–533. Translated from Pis'ma v Astronomicheskiĭ Zhurnal, Vol. 30, No. 8, 2004, pp. 582–588.

A Hard X-ray Sky Survey with the SIGMA Telescope of the GRANAT Observatory

M. G. Revnivtsev[1,2*], R. A. Sunyaev[1,2], M. R. Gilfanov[1,2], E. M. Churazov[1,2], A. Goldwurm[3,4], J. Paul[3,4], P. Mandrou, and J. P. Roques[5]

[1] *Space Research Institute, Russian Academy of Sciences, Profsoyuznaya ul. 84/32, Moscow, 117810 Russia*
[2] *Max Planck Institut für Astrophysik, Karl Schwarzschild Str. 1, 85740 Garching bei München, Germany*
[3] *DAPNIA/Service d'Astrophysique CEA Saclay, France*
[4] *Fédération de Recherche Astroparticule et Cosmologie Université de Paris, France*
[5] *Centre d'Etudes Spatiale des Rayonnements, Toulouse, France*

Received January 15, 2004

Abstract—The SIGMA X-ray telescope accumulated the images of more than a quarter of the sky during the in-orbit operation of the GRANAT observatory. The longest exposure time (∼9 million s) was spent on the observations of the Galactic center region. We give an overview of the SIGMA X-ray observations and report the sensitivities achieved in various regions of the sky. © *2004 MAIK "Nauka/Interperiodica"*.

Key words: *GRANAT Observatory, SIGMA X-ray telescope, sky survey.*

INTRODUCTION

The SIGMA telescope of the GRANAT observatory was the first coded-aperture orbital X-ray telescope to operate in the energy range 35 keV–1.3 MeV. The long operation time of the telescope (which operated with interruptions for almost eight years) made it possible to obtain a unique set of hard X-ray sky images with the then record spatial resolution of $\sim 15'$ and source localization accuracy ($\sim 2'-3'$). As a result, in particular, the hard X-ray source GRS 1758–258 located at only 40′ from the bright soft X-ray source GX5–1 (Mandrou *et al.* 1991; Sunyaev *et al.* 1991a) was discovered, significant hard (>400 keV) X-ray variability was detected from the black hole 1E1740.7–2942, hard emission was recorded from the X-ray burster A1742–294 (Churazov *et al.* 1995), and an upper limit was placed on the hard X-ray flux from the central supermassive black hole in our Galaxy (Sunyaev *et al.* 1991a; Goldwurm *et al.* 1994).

In recent years, substantial progress has been made in the area of all-sky hard (20–200 keV) X-ray surveys. In particular, the INTEGRAL orbital observatory, which can provide a factor of 5–8 higher sensitivity than that of SIGMA in the energy range 40–100 keV, was put into orbit in 2002 (Winkler *et al.* 2003), the SWIFT observatories are planned to be launched (Gehrels 2000), and the SIMBOL-X observatory, which will be more than two orders of magnitude more sensitive than SIGMA at energies up to 60–70 keV (Ferrando 2002), is being developed. Therefore, we deemed it appropriate to publish an overview of all of the SIGMA/GRANAT observations.

The SIGMA observations during the period 1990–1998 covered more than a quarter of the sky with a sensitivity higher than 100 mCrab. The longest exposure time (∼9 million s) was spent on the observations of the Galactic center, providing a ∼10 mCrab sensitivity for the discovery of new sources. In this paper, we give an overview of the SIGMA observations, the achieved sensitivities of the sky survey, and a list of the sources detected during the period 1990–1998.

RESULTS

The joint French–Soviet SIGMA X-ray telescope was one of the main instruments onboard the GRANAT orbital observatory. The coded aperture, a tungsten mask located at a distance of ∼2.5 m from the position-sensitive NaI detector, allowed X-ray sky images in the energy range 35–1300 keV to be reconstructed with a spatial resolution of $\sim 15'$. The high-apogee orbit of the GRANAT observatory (with a revolution period of 4 days and an apogee height of ∼200 000 km) made it possible to perform

*E-mail: revnivtsev@iki.rssi.ru

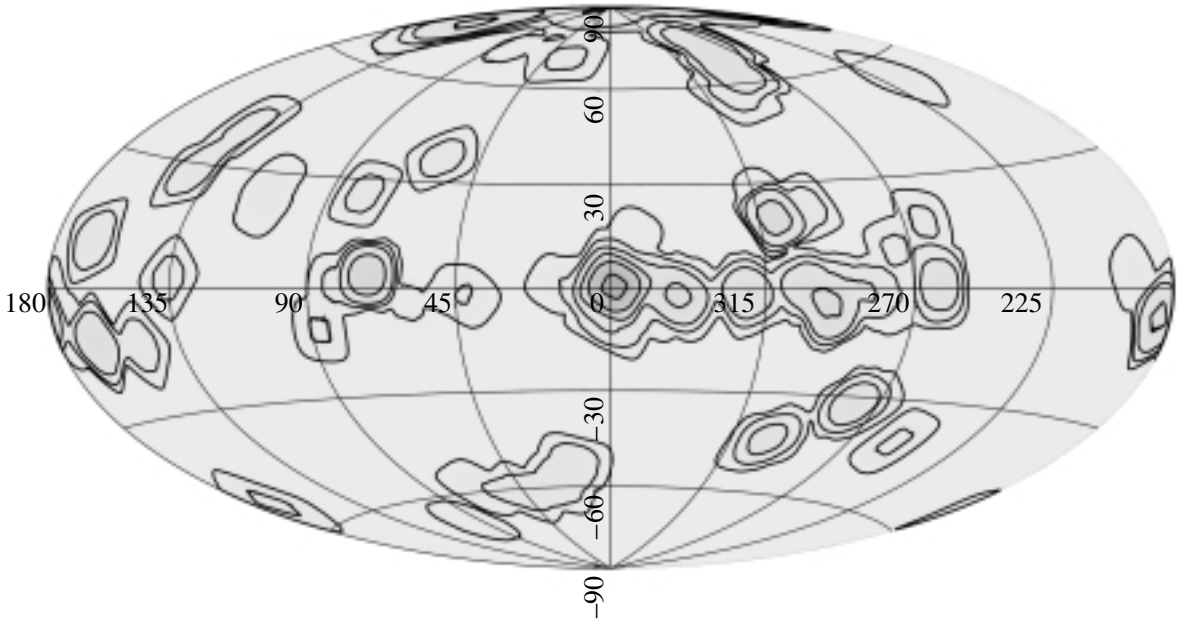

Fig. 1. Exposure map of the SIGMA X-ray observations for the period 1990–1998. The contours indicate the regions with exposure times longer than 10 000, 100 000, 316 000, 1.0×10^6, 3.16×10^6, and 8×10^6 s.

almost continuous observations for 3 days, interrupted by data transmission sessions. The telescope was described in detail by Paul *et al.* (1991); in-flight calibrations of the instrument were given by Mandrou *et al.* (1991).

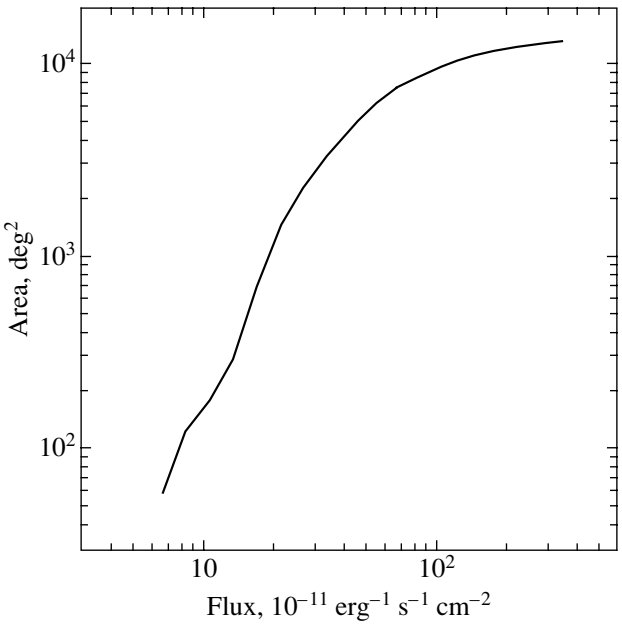

Fig. 2. Solid angle in the sky versus SIGMA sensitivity to the detection of new sources (5σ) achieved over the entire observing period.

Over the period 1990–1998, the telescope performed more than 500 pointed observations of astrophysical objects with a typical duration of about 20 h. The total effective exposure time of all observations (corrected for the dead time) is ~30 million s. About 9 million s of these were spent on the observations of the Galactic-Center region. Figure 1 shows a map of the effective exposure (corrected for dead time and vignetting—the dependence of the effective exposure on distance from the center of the field of view) for all pointed SIGMA observations. The contours in this figure correspond to exposure times of 10, 100, and 316 thousand s, 1, 3.16, and 8 million s.

The SIGMA sensitivity to typical X-ray sources reaches its maximum in the energy range 40–100 keV. In Fig. 2, the solid angle in the sky is plotted against the sensitivity achieved in this solid angle over the entire observing period. Figure 3 shows sensitivity contours in the longest-exposure region (the Galactic Center and the Norma Arm tangent). The sensitivity corresponds to the 5σ detection level, i.e., to the detection of an unknown source. A lower level (e.g., ~2–3σ) can be used to place an upper limit on the flux from a source with a known position. In this case, the upper limit on the flux from a source in the region of the Galactic Center will be ~4–6 mCrab. For a source with an energy spectrum similar to that of the Crab nebula (a power-law spectrum with a

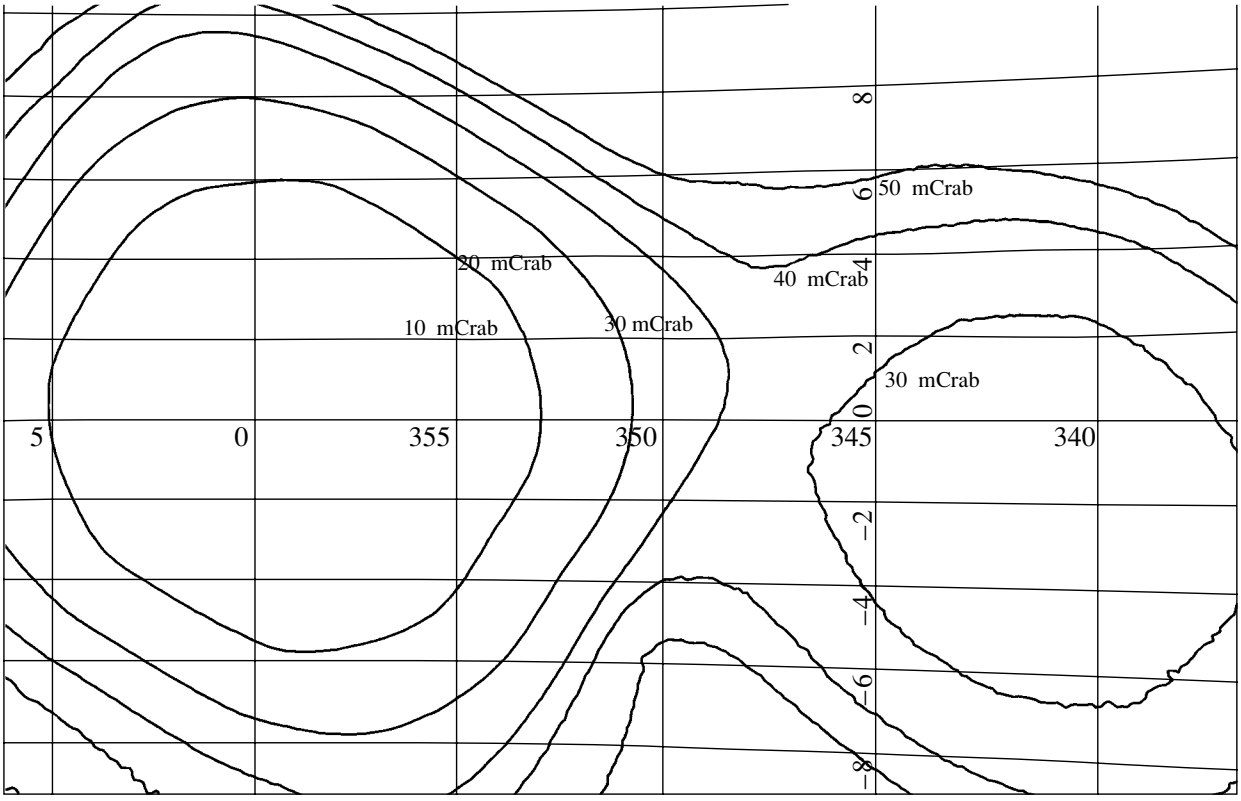

Fig. 3. Contours of SIGMA sensitivity to the detection of new sources (5σ) in the region of the Galactic Center and the Norma spiral arm.

photon index of 2.1), a 1-mCrab flux in the energy range 40–100 keV corresponds to an energy flux of $\approx 9.7\times10^{-12}$ erg s^{-1} cm^{-2} or $\approx 1.0\times10^{-4}$ photons s^{-1} cm^{-2}, which corresponds to a luminosity of $\sim 8\times10^{35}$ erg s^{-1} at the distance of the Galactic Center (8.5 kpc).

Over the period of its operation, the telescope detected several X-ray sources of various natures: compact Galactic sources, including binaries with black holes and neutron stars; X-ray novae; and active galactic nuclei. The table lists all of the sources that were detected by the telescope at a statistically significant level over the entire observing period. The last column of the table gives references to the papers that describe the SIGMA results in more detail.

Figure 4 shows the sky map obtained by averaging all of the observations. Figure 5 shows enlarged images of the region of the Galactic Center and the Norma Arm tangent. Since the data averaged over the entire eight-year observing period are shown in these images, we see no weak transient sources as, for example, several weak X-ray novae (e.g., KS/GRS 1730–312 and GRS 1739–278) and the variable X-ray burster KS 1731–260, which periodically appears and disappears in the hard X-ray energy range.

To summarize, we can say the following about the SIGMA sky survey: The typical sensitivity of the telescope to the detection of new sources was about 100 mCrab for much ($\sim$1/4) of the sky. This sensitivity is slightly lower than that of the previous hard X-ray all-sky survey conducted by the A4 scanning collimator of the HEAO1 observatory (it had a typical sensitivity of $\sim$10–15 mCrab to the detection of new sources; see Levine *et al.* 1984). However, the SIGMA high spatial resolution and source localization accuracy allowed this telescope to make several interesting discoveries in the densely populated region of the Galactic Center, which was inaccessible to HEAO1/A4. The SIGMA telescope achieved a sensitivity of about $\sim$8–10 mCrab in the Galactic-Center region that was comparable to the HEAO1/A4 sensitivity; however, the SIGMA resolution was $\sim 15'$, while its source localization accuracy was within $\sim 2'$–$3'$.

List of sources detected by the SIGMA telescope in the energy range 40–100 keV

Source	$F_{max,40-100}$, mCrab	Class	References
Galactic sources			
Crab[h]	1000	Pulsar	1
Cyg X–1[h]	2000	BH	2, 3, 4
1E1740.4–2942[h]	150	BH	4, 5, 6, 7
GRS 1758–258[h]	100	BH	5, 8, 9, 10
GRS 1915+105[h]	150	BH	11
GX339–4[h]	430	BH	12, 13
SLX 1735–269	20	NS, Burster	14
KS 1731–260	70	NS, Burster	15
TrA X–1	80	BH?	16
4U1724–30 (Terzan 2)	50	NS, Burster	16, 17
H1732–304 (Terzan 1)	10	NS, Burster	18
GX354–0 (4U1728–34)	100	NS, Burster	19
A1742–294	30	NS, Burster	20
4U1705–44	70	NS, Burster	21
4U1608–52	70	NS, Burster	21
4U1700–37	200	NS, HMXB	22, 23
OAO 1657–415	100	NS, Accr. Pulsar	24
Vela X–1	200	NS, Accr. Pulsar	25
GX1+4	100	NS, Accr. Pulsar	26, 27
PSR 1509–58	17	NS, Pulsar	28
GRS 0834–430	100	NS, Accr. Pulsar	29
GRO J1744–28	120	NS, Accr. Burster-pulsar	30
Sgr A*	<10	SBH	5, 31
GRS 1227+025	100		32
Extragalactic sources			
Cen A	130	AGN	33, 34, 35
3C273	40	Blasar	34, 36
NGC 4151	40	AGN	34, 37, 38
NGC 4388	10	AGN	39
GRS 1734–292	36	AGN	40
X-ray novae			
Nova Musca 91 (GS/GRS 1124–68)	1070	BH	40, 41, 42
Nova Persei 92 (GRO J0422+32)	2800	BH	43, 44, 45, 46, 47
Nova Oph 93 (GRS 1716–249)	1200	BH	48
Nova Vel 93 (GRS 1009–45)	65	BH	49
KS/GRS 1730–312	170	BH	50, 51
GRS 1739–278	100	BH	52
GRS 1737–31	115	BH	53
XTE J1755–324	85	BH	54, 55

Note. [h]—The sources was also detected in the energy range 100–200 keV. 1—Gilfanov *et al.* (1994), 2—Salotti *et al.* (1992), 3—Vikhlikhin *et al.* (1994), 4—Kuznetsov *et al.* (1997), 5—Sunyaev *et al.* (1991a), 6—Bouchet *et al.* (1991), 7—Sunyaev *et al.* (1991b), 8—Laurent *et al.* (1993a), 9—Gil'fanov *et al.* (1993), 10—Kuznetsov *et al.* (1999), 11—Finoguenov *et al.* (1994), 12—Bouchet *et al.* (1993), 13—Trudolyubov *et al.* (1998), 14—Goldwurm *et al.* (1996), 15—Barret *et al.* (1993), 16—Barret *et al.* (1992), 17—Barret *et al.* (1991), 18—Borrel *et al.* (1996), 19—Claret *et al.* (1994), 20—Churazov *et al.* (1995), 21—Revnivtsev *et al.* (1997), 22—Laurent *et al.* (1992), 23—Sitdikov *et al.* (1993), 24—Mereghetti *et al.* (1991), 25—Laurent *et al.* (1995), 26—Laurent *et al.* (1993b), 27—David *et al.* (1998), 28—Laurent *et al.* (1994), 29—Denis *et al.* (1993), 30—Meji'a *et al.* (2002), 31—Goldwurm *et al.* (1994), 32—Jourdain *et al.* (1992a), 33—Bassani *et al.* (1993), 34—Churazov *et al.* (1994b), 35—Bond *et al.* (1996), 36—Bassani *et al.* (1992), 37—Jourdain *et al.* (1992b), 38—Finoguenov *et al.* (1995), 39—Lebrun *et al.* (1992), 40—Gilfanov *et al.* (1991), 41—Sunyaev *et al.* (1992), 42—Goldwurm *et al.* (1992), 43—Claret *et al.* (1993), 44—Roques *et al.* (1994), 45—Denis *et al.* (1994), 46—Vikhlikhin *et al.* (1995), 47—Finoguenov *et al.* (1996), 48—Revnivtsev *et al.* (1998), 49—Goldoni *et al.* (1998), 50—Trudolyubov *et al.* (1996), 51—Vargas *et al.* (1996), 52—Vargas *et al.* (1997), 53—Trudolyubov *et al.* (1999), 54—Revnivtsev *et al.* (1999), 55—Goldoni *et al.* (1999).

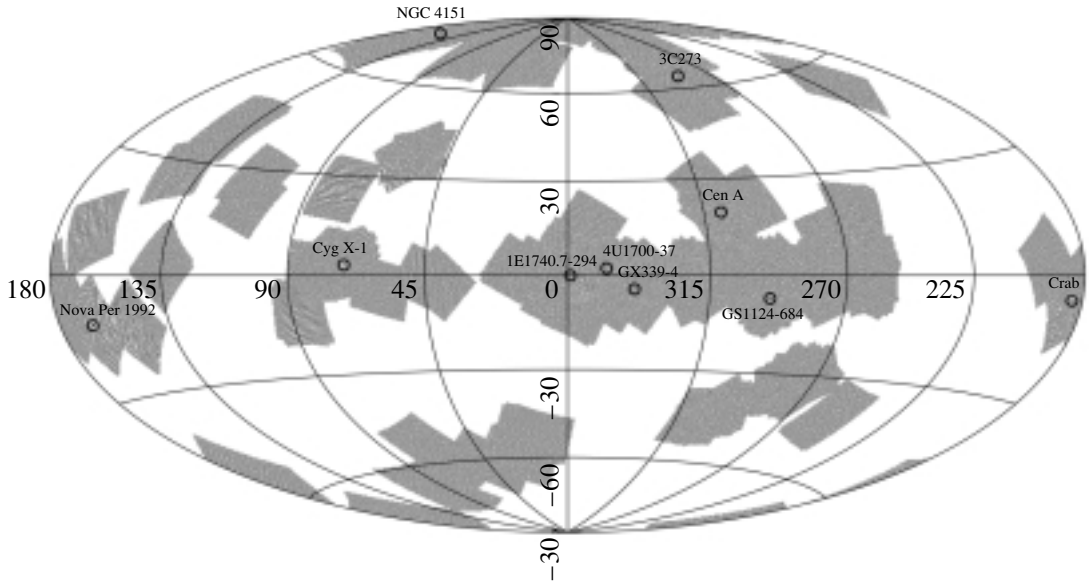

Fig. 4. Averaged all-sky SIGMA image. Only the brightest sources are labeled.

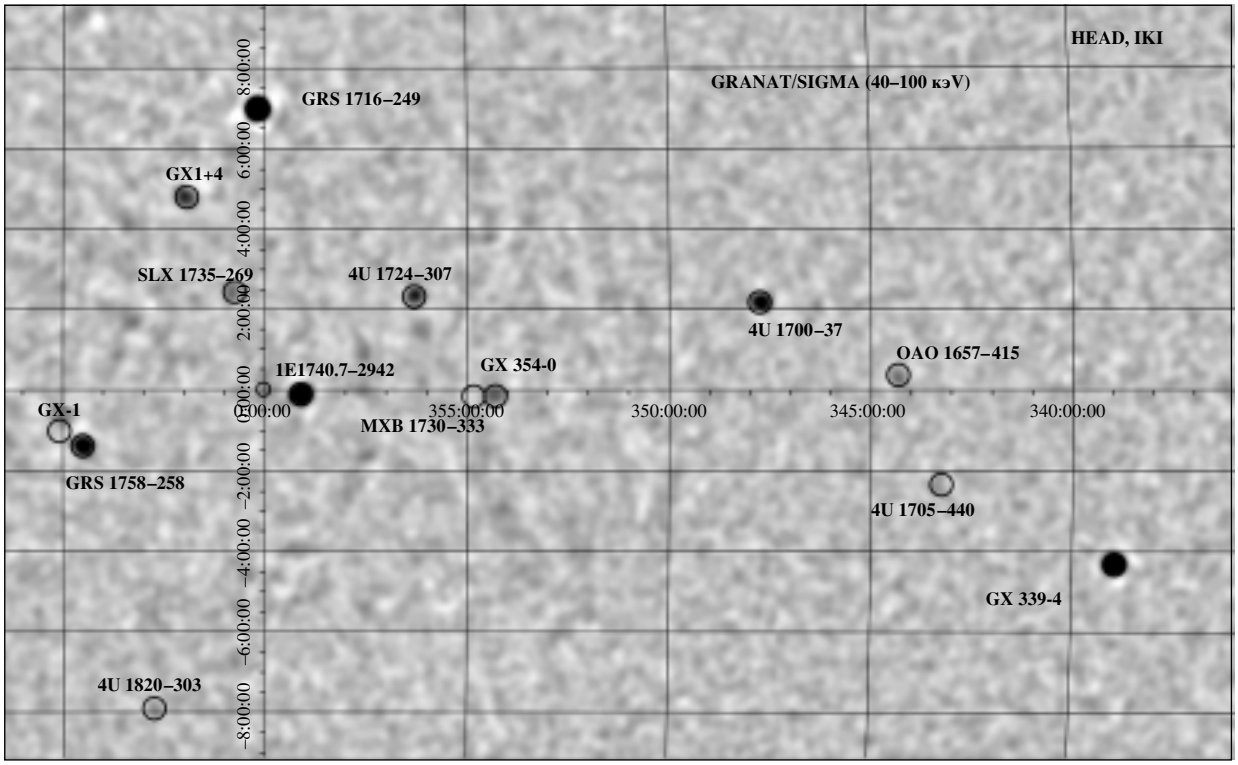

Fig. 5. Averaged image of the region of the Galactic Center obtained by the SIGMA telescope over the entire observing period.

ACKNOWLEDGMENTS

This work was supported by the Ministry of Industry and Science (RF Presidential Grant no. NSh-2083.2003.2) and the Nonstationary Phenomena in Astronomy Program of the Russian Academy of Sciences.

REFERENCES

1. D. Barret, S. Mereghetti, J. P. Roques, *et al.*, Astrophys. J. **379**, 21 (1991).
2. D. Barret, J. P. Roques, P. Mandrou, *et al.*, Astrophys. J. **392**, 19 (1992).
3. D. Barret, P. Mandrou, J. P. Roques, *et al.*, Astron. Astrophys., Suppl. Ser. **97**, 241 (1993).

4. L. Bassani, E. Jourdain, J. P. Roques, *et al.*, Astrophys. J. **396**, 504 (1992).
5. L. Bassani, E. Jourdain, J. P. Roques, *et al.*, Astron. Astrophys., Suppl. Ser. **97**, 89 (1993).
6. G. Belanger, A. Goldwurm, P. Goldoni, *et al.*, Astron. Astrophys. (2003, in press); astro-ph/0311147.
7. I. A. Bond, J. Ballet, M. Denis, *et al.*, Astron. Astrophys. **307**, 708 (1996).
8. V. Borrel, L. Bouchet, E. Jourdain, *et al.*, Astrophys. J. **462**, 754 (1996).
9. L. Bouchet, P. Mandrou, J. P. Roques, *et al.*, Astrophys. J. **383**, L45 (1991).
10. L. Bouchet, E. Jourdain, P. Mandrou, *et al.*, Astrophys. J. **407**, 739 (1993).
11. E. Churazov, M. Gilfanov, R. Sunyaev, *et al.*, Astrophys. J. Suppl. **92**, 381 (1994).
12. E. Churazov, M. Gilfanov, A. Finoguenov, *et al.*, IAU Symp. **159**, 63 (1994).
13. E. Churazov, M. Gilfanov, R. Sunyaev, *et al.*, Astrophys. J. **443**, 341 (1995).
14. A. Claret, J. Ballet, A. Goldwurm, *et al.*, Adv. Space Res. **13**, 735 (1993).
15. A. Claret, A. Goldwurm, B. Cordier, *et al.*, Astrophys. J. **423**, 436 (1994).
16. B. Cordier, A. Goldwurm, P. Laurent, *et al.*, Adv. Space Res. **11**, 169 (1991).
17. P. David, P. Laurent, M. Denis, *et al.*, Astron. Astrophys. **332**, 165 (1998).
18. M. Denis, J. P. Roques, D. Barret, *et al.*, Astron. Astrophys., Suppl. Ser. **97**, 333 (1993).
19. M. Denis, J. Olive, P. Mandrou, *et al.*, Astrophys. J. Suppl. **92**, 459 (1994).
20. Ph. Ferrando, in *Proceedings of the 4th Microquasar Workshop, Corsica, France, 2002*, Ed. by Ph. Durouchoux, Y. Fuchs, and J. Rodriguez; astro-ph/0209062.
21. A. Finoguenov, E. Churazov, M. Gilfanov, *et al.*, Astrophys. J. **424**, 940 (1994).
22. A. Finoguenov, E. Churazov, M. Gilfanov, *et al.*, Astron. Astrophys. **300**, 101 (1995).
23. A. Finoguenov, M. Gilfanov, E. Churazov, *et al.*, Astron. Lett. **22**, 721 (1996).
24. N. Gehrels, Proc. SPIE **4140**, 42 (2000).
25. M. Gilfanov, R. Sunyaev, E. Churazov, *et al.*, Pis'ma Astron. Zh. **17**, 1059 (1991) [Sov. Astron. Lett. **17**, 437 (1991)].
26. M. Gilfanov, E. Churazov, R. Sunyaev, *et al.*, Astron. Astrophys. **418**, 844 (1993).
27. M. Gilfanov, E. Churazov, R. Sunyaev, *et al.*, Astrophys. J., Suppl. Ser. **92**, 411 (1994).
28. P. Goldoni, M. Vargas, A. Goldwurm, *et al.*, Astron. Astrophys. **239**, 186 (1998).
29. P. Goldoni, M. Vargas, A. Goldwurm, *et al.*, Astrophys. J. **511**, 847 (1999).
30. A. Goldwurm, J. Ballet, B. Cordier, *et al.*, Astrophys. J. **389**, L79 (1992).
31. A. Goldwurm, B. Cordier, J. Paul, *et al.*, Nature **371**, 589 (1994).
32. A. Goldwurm, M. Vargas, J. Paul, *et al.*, Astron. Astrophys. **310**, 857 (1996).
33. E. Jourdain, L. Bassani, J. P. Roques, *et al.*, Astrophys. J. **395**, L69 (1992a).
34. E. Jourdain, L. Bassani, L. Bouchet, *et al.*, Astron. Astrophys. **256**, 38 (1992b).
35. S. Kuznetsov, M. Gilfanov, E. Churazov, *et al.*, Mon. Not. R. Astron. Soc. **292**, 651 (1997).
36. S. Kuznetsov, M. Gilfanov, E. Churazov, *et al.*, Pis'ma Astron. Zh. **25**, 414 (1999) [Astron. Lett. **25**, 351 (1999)].
37. P. Laurent, A. Goldwurm, F. Lebrun, *et al.*, Astron. Astrophys. **260**, 237 (1992).
38. P. Laurent, B. Cordier, A. Goldwurm, *et al.*, Adv. Space Res. **13**, 751 (1993a).
39. P. Laurent, L. Salotti, J. Paul, *et al.*, Astron. Astrophys. **278**, 444 (1993b).
40. P. Laurent, J. Paul, A. Claret, *et al.*, Astron. Astrophys. **286**, 838 (1994).
41. P. Laurent, J. Paul, M. Denis, *et al.*, Astron. Astrophys. **300**, 399 (1995).
42. F. Lebrun, J. Ballet, J. Paul, *et al.*, Astron. Astrophys. **264**, 22 (1992).
43. A. Levine, F. Lang, W. Lewin, *et al.*, Astrophys. J., Suppl. Ser. **54**, 581 (1984).
44. P. Mandrou, J. P. Chabaud, and M. Ehanno, in *Proceedings of the International Symposium on Gamma-Ray Line Astrophysics, Paris, 1990* (AIP, New York, 1991), p. 492.
45. J. Meji'a, T. Villela, P. Goldoni, *et al.*, Astrophys. J. **566**, 387 (2002).
46. S. Mereghetti, J. Ballet, A. Lambert, *et al.*, Astrophys. J. **366**, L23 (1991).
47. M. N. Pavlinsky, S. A. Grebenev, and R. A. Sunyaev, Pis'ma Astron. Zh. **18**, 291 (1992) [Sov. Astron. Lett. **18**, 116 (1992)].
48. M. Pavlinsky, S. Grebenev, and R. Sunyaev, Astrophys. J. **425**, 110 (1994).
49. J. Paul, J. Ballet, M. Cantin, *et al.*, Adv. Space Res. **11**, 279 (1991).
50. M. Revnivtsev, M. Gilfanov, E. Churazov, *et al., Joint European and National Astronomical Meeting, JENAM-97* (Thessaloniki, Greece, 1997), p. 289.
51. M. Revnivtsev, M. Gilfanov, E. Churazov, *et al.*, Astron. Astrophys. **331**, 557 (1998).
52. M. Revnivtsev, M. Gilfanov, E. Churazov, *et al.*, Pis'ma Astron. Zh. **25**, 575 (1999) [Astron. Lett. **25**, 493 (1999)].
53. J. P. Roques, L. Bouchet, E. Jourdain, *et al.*, Astrophys. J. Suppl. **92**, 451 (1994).
54. L. Salotti, J. Ballet, B. Cordier, *et al.*, Astron. Astrophys. **253**, 145 (1992).
55. A. Sitdikov, M. Gilfanov, R. Sunyaev, *et al.*, Pis'ma Astron. Zh. **19**, 483 (1993) [Astron. Lett. **19**, 188 (1993)].
56. G. Skinner, T. Ponman, A. Hammersley, and C. Eyles, Astrophys. Space Sci. **136**, 337 (1987a).
57. G. Skinner, A. Willmore, C. Eyles, *et al.*, Nature **330**, 544 (1987b).
58. R. Sunyaev, E. Churazov, V. Efremov, *et al.*, Adv. Space Res. **10**, 41 (1990).
59. R. Sunyaev, E. Churazov, M. Gilfanov, *et al.*, Astron. Astrophys. **247**, 29 (1991a).

60. R. Sunyaev, E. Churazov, M. Gilfanov, *et al.*, Astrophys. J. **383**, L49 (1991b).
61. R. Sunyaev, E. Churazov, M. Gilfanov, *et al.*, Astrophys. J. **389**, L75 (1992).
62. R. Sunyaev, S. Grebenev, A. Lutovinov, *et al.*, Astron. Telegram, No. 190 (2003).
63. S. Trudolyubov, M. Gilfanov, E. Churazov, *et al.*, Pis'ma Astron. Zh. **22**, 740 (1996) [Astron. Lett. **22**, 664 (1996)].
64. S. Trudolyubov, M. Gilfanov, E. Churazov, *et al.*, Astron. Astrophys. **334**, 895 (1998).
65. S. Trudolyubov, E. Churazov, M. Gilfanov, *et al.*, Astron. Astrophys. **342**, 496 (1999).
66. M. Vargas, A. Goldwurm, and M. Denis, Astron. Astrophys. Suppl. **120**, 291 (1996).
67. M. Vargas, A. Goldwurm, P. Laurent, *et al.*, Astrophys. J. **476**, L23 (1997).
68. A. Vikhlinin, E. Churazov, M. Gilfanov, *et al.*, Astrophys. J. **424**, 395 (1994).
69. A. Vikhlinin, E. Churazov, M. Gilfanov, *et al.*, Astrophys. J. **441**, 779 (1995).
70. C. Winkler, T. J.-L. Courvoisier, G. Di Cocco, *et al.*, Astron. Astrophys. **411**, 1 (2003).

Translated by A. Dambis

Astronomy Letters, Vol. 30, No. 8, 2004, pp. 534–539. Translated from Pis'ma v Astronomicheskiĭ Zhurnal, Vol. 30, No. 8, 2004, pp. 589–595.

A Hard X-ray Survey of the Sagittarius Arm Tangent with the IBIS Telescope of the INTEGRAL Observatory: A Catalog of Sources

S. V. Molkov[1,2*], A. M. Cherepashchuk[2], A. A. Lutovinov[1], M. G. Revnivtsev[1,3], K. A. Postnov[2], and R. A. Sunyaev[1,3]

[1] *Space Research Institute, Russian Academy of Sciences, Profsoyuznaya ul. 84/32, Moscow, 117810 Russia*

[2] *Sternberg Astronomical Institute, Universitetskiĭ pr. 13, Moscow, 119992 Russia*

[3] *Max Planck Institut für Astrophysik, Karl Schwarzschild Str. 1, Postfach 1317, D-85741 Garching bei München, Germany*

Received February 2, 2004

Abstract—We analyze the images of the Sagittarius Arm tangent obtained with the IBIS telescope of the INTEGRAL observatory in the energy range 18–120 keV during its observations in the spring of 2003. We detected 28 sources at a statistically significant level with fluxes above 1.4 mCrab in the energy range 18–60 keV. Of these sources, 16 were previously identified as binaries of various classes in our Galaxy, 3 were identified as extragalactic objects, 2 were identified as pulsars in supernova remnants, and 7 sources were of an unknown nature. These observations revealed three new sources. A statistically significant flux in the energy range 60–120 keV was recorded from 13 sources. © *2004 MAIK "Nauka/Interperiodica"*.

Key words: *Galaxy, spiral arms, hard X-ray sources.*

INTRODUCTION

The Sagittarius Arm of the Galaxy is one of the spiral arms closest to its center and lies at a distance of ~2.2 kpc from the Sun. From the Earth, it is observed at a tangential angle, which increases the number of stars on the line of sight. This region is very rich in young, massive stars and the end products of their evolution (high-mass X-ray binaries, microquasars, X-ray pulsars, supernova remnants, etc.).

There are a number of interesting objects in the region of the arm, such as the brightest microquasar GRS 1915+105, the peculiar black hole SS 433, other black hole candidates (XTE J1908+094, X1908+075), the soft gamma repeater SGR 1900+14, supernova remnants, more than ten persistent and transient X-ray bursters (4U1916–053, Ser X-1, Aql X-1), and X-ray pulsars (XTE J1855–026, 4U1907+097, GS1843+009, X1901+03, etc.). Several sources in this region were discovered by instruments of the INTEGRAL observatory.

Observations of such regions of the sky rich in sources as the Galactic Center (Revnivtsev *et al.* 2004) and the Sagittarius Arm tangent demonstrate the excellent potentialities of the telescopes of the INTEGRAL observatory for mapping the sky in hard X rays. This makes it possible to conduct high-sensitivity sky surveys and to monitor the state of transient sources within the field of view of the INTEGRAL telescopes (Cherepashchuk *et al.* 2003; Molkov *et al.* 2003).

This study is part of the program of mapping the Galaxy in hard X rays and searching for pointlike X-ray sources. It is based on data obtained with the IBIS telescope of the INTEGRAL observatory. The results of a deep survey of the Galactic-center region were published by Revnivtsev *et al.* (2004).

OBSERVATIONS AND DATA ANALYSIS

The INTEGRAL International Gamma-Ray Observatory was launched into a high-apogee orbit by a Russian PROTON carrier rocket from Baikonur on October 17, 2002 (Eismont *et al.* 2003). It includes four instruments that enable simultaneous observations of sources in the X-ray, gamma-ray, and optical energy ranges (Winkler *et al.* 2003). One of these instruments, the IBIS telescope, its upper ISGRI detector (Lebrun *et al.* 2003), best meets the goals of mapping and detecting pointlike X-ray sources in the hard X-ray energy range. This instrument works on the principle of a coded aperture and can reconstruct the image of a selected sky area within a $29^\circ \times 29^\circ$ field of view (the region of full coding is $9^\circ \times 9^\circ$) in the energy range 15–200 keV with an angular resolution of $12'$.

*E-mail: molkov@hea.iki.rssi.ru

1063-7737/04/3008-0534$26.00

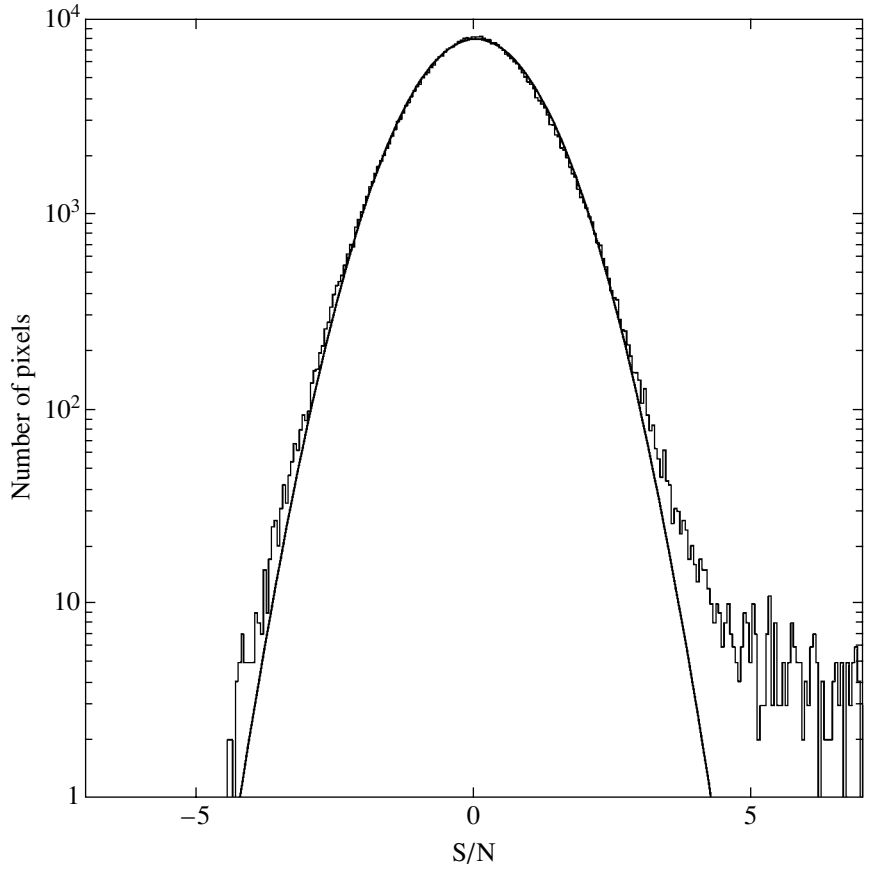

Fig. 1. Distribution of the signal-to-noise ratio for all points of the total image of the region being analyzed. The solid curve indicates the normal distribution with a zero mean and a unit dispersion.

The Sagittarius Arm tangent of the Galaxy was regularly observed by the INTEGRAL observatory during the first year of its in-orbit operation. In this paper, we used the data of the general program obtained during a series of observations of the transient source Aql X-1 during its outburst in March–April 2003 (Molkov *et al.* 2003) and observations of the peculiar black hole SS 433 in May 2003 (Cherepashchuk *et al.* 2003a). The total exposure time for this region was ~830 ks. Since the so-called raster system was used in the observations, when, apart from the pointing at the source itself, 24 pointings at neighboring regions with offsets by 2° and 4° from the source were made, a substantial region of the sky in this part of the Galaxy with a size of about 40° × 35° could be covered.

We processed all of the observations using the technique described by Revnivtsev *et al.* (2004). Our analysis of a large set of calibration observations for the Crab Nebula with different positions of this source within the field of view of the telescope showed that, with the approach and software used, the conservative estimate of the systematic uncertainty in the absolute value of the measured fluxes from the sources is ~10%. The localization accuracy of bright sources similar to the Crab Nebula is $\sim 0'.4$ (1σ); for fainter sources, it decreases to $\sim 2'-3'$.

When analyzing the images obtained, we considered the presence of a peak with an intensity above a certain value as evidence of a pointlike source. The statistical threshold was chosen after the total image was analyzed. We found a signal-to-noise ratio (S/N) that provided a detection probability of no more than one spurious source in the entire field under study.

Figure 1 shows the distribution of the signal-to-noise ratio for all points of the total image of the region. For an ideal image with negligible systematic deviations, the distribution of this quantity in a region without any sources must be described by the normal distribution with a zero mean and a unit dispersion. The solid curve in Fig. 1 indicates the normal distribution with these parameters on a logarithmic scale. We clearly see from the negative part of the distribution that the measured distribution is well described by the theoretically expected distribution down to S/N ~ −4. However, small deviations in the S/N range from −4 to −5 are also noticeable: the measured distribution exhibits a slightly larger number

of points than their predicted number. Thus, we may conclude that it would be incorrect to use the purely theoretical detection threshold of a source ($\sim 4.2\sigma$). Therefore, below, we use $S/N > 5.0$ as a lower limit of the statistically significant signal detection threshold.

RESULTS

The table lists the detected sources together with their coordinates and fluxes in mCrabs in two energy ranges. A flux of 1 mCrab in the energy ranges 18–60 and 60–120 keV for a source with a power-law spectrum with the photon index $\Gamma = 2.1$ corresponds to energy fluxes of $\sim 1.4\times10^{-11}$ and $\sim 7.1\times10^{-12}$ erg s^{-1} cm^{-2}, respectively. The localization accuracy of the sources is $\sim 2'$–$3'$ (the radius of the 90% confidence contour). The sources are arranged in order of decreasing detection significance, which depends not only on the intensity, but also on the effective observing time of each specific object.

Figure 2 shows an image of the Sagittarius Arm tangent with sizes of $\sim 35^\circ \times 25^\circ$ in the energy range 18–60 keV in Galactic coordinates. Our analysis of the images obtained revealed 28 sources in the energy range 18–60 keV; some of them (14) are still fairly bright and are detectable in the harder energy range 60–120 keV at a statistically significant level (see the table).

Some of the detected sources (21 of the 28) are of a known nature and are either high-mass (HMXB) or low-mass (LMXB) X-ray binaries or extragalactic objects. In the table, the class of the detected objects is given in the last column using the following abbreviations: LMXB (low-mass X-ray binaries with a mass of the normal companion $\sim 1M_\odot$); HMXB (high-mass X-ray binaries with a mass of the normal companion $\geq 8M_\odot$); BH (black hole candidates); T (transient sources); P (X-ray pulsars); B (X-ray bursters), systems with a neutron star as the compact object with occasional bursts of unsteady thermonuclear burning on their surfaces; Z (Z sources); G (sources in globular clusters); AXP (anomalous X-ray pulsars); SNR (supernova remnants); and AGN (active galactic nuclei).

Four black hole candidates were detected during the observations: the best-known candidate, GRS 1915+105, was in a bright state and was observed by the INTEGRAL observatory several more times (Hannikainen *et al.* 2003a), along with SS 433 (Cherepashchuk *et al.* 2003), XTE J1908+094, and X1908+075 (Wen *et al.* 2000).

In addition, a statistically significant X-ray flux was detected from seven X-ray pulsars: X1901+03, 4U1907+097, XTE J1855–026, GS1843+009, A1845–024, 1E1841–045 (an anomalous X-ray pulsar), and PSR J1846–0258. The first of these (X1901+03) was previously known only as a transient high-mass binary (Forman *et al.* 1976), which had exhibited no activity since 1971. In early 2003, the source reappeared in the X-ray sky, and coherent X-ray pulsations were detected from it (Galloway *et al.* 2003a; Molkov *et al.* 2003).

Six of the seven detected low-mass X-ray binaries with neutron stars are bursters (one of them, 4U1850–087, is in the globular cluster NGC 6712).

During our observations, we detected a statistically significant X-ray flux from three supernova remnants (the flux from two of them was associated above with pulsars) and two active galactic nuclei (NGC 6814 and SS 442/1H1934–063). The identification of the last source is ambiguous. What is important is that the position of the source derived in our analysis differs from the more accurate position of SS 442/1H1934–063 taken from the catalog by $\sim 5'.6$. However, since the source is recorded at a very low sensitivity level ($\sim 5\sigma$) and since the radius of the 90% confidence contour for its localization is $\sim 3'$, there is a $\sim 10\%$ probability that its measured position will differ from the actual position by more than $3'$. Nevertheless, we cannot rule out the possibility that it is a new source, IGR J19378–0617.

Two known X-ray sources discovered by RXTE (XTE J1901+014) and ASCA (AX J183800–0655) were detected in our observations at a statistically significant level; however, their class has not yet been established.

Finally, there were seven sources discovered by the INTEGRAL observatory within the IBIS field of view. Five of these sources were detected with confidence in our observations: IGR J19140+098 (Hannikainen *et al.* 2003b), IGR J18483–031 (Chernyakova *et al.* 2003), IGR J18490–0000, IGR J18406–0539, and IGR J18450–0435 (the last three sources were detected for the first time in this work). The remaining two sources, IGR J18325–0756 and IGR J18539+0727, discovered previously by INTEGRAL (Lutovinov *et al.* 2003a, 2003b), were not detected in these observations, and we give here only the upper limits on their fluxes. Note that source IGR J18539+0727 is probably a black hole candidate (Lutovinov and Revnivtsev 2003).

In summary, we may conclude that seven of the 28 sources detected during the observations of the Sagittarius Arm tangent of the Galaxy are of an unknown nature; five of these were discovered by the INTEGRAL observatory.

In conclusion, we note that the results presented here (a list of sources and their fluxes) were obtained from averaged images of the region under

List of sources detected during the observations of the Sagittarius Arm of the Galaxy in the period March–May 2003

No.	J2000		Mean flux, mCrab[a]		Identification	Class
	α	δ	18–60 keV	60–120 keV		
1	288.80	10.95	252.6 ± 0.2	80.0 ± 0.7	GRS 1915+105	LMXB, BH
2	285.91	3.21	77.4 ± 0.2	3.2 ± 0.6	X1901+03[b]	HMXB, TP
3	287.96	4.99	14.0 ± 0.2	6.2 ± 0.6	SS433	HMXB, BH
4	287.71	7.60	10.9 ± 0.2	6.8 ± 0.6	X1908+075	HMXB, BH?
5	287.42	9.83	10.9 ± 0.2	0.8 ± 0.7[f]	4U1907+097	HMXB, TP
6	283.87	−2.60	8.8 ± 0.2	4.4 ± 0.7	XTE J1855–026	HMXB, P
7	279.99	5.03	7.5 ± 0.2	0.6 ± 0.7[f]	Ser X-1	LMXB, B
8	288.53	9.87	6.5 ± 0.2	2.8 ± 0.7	IGR J19140+098	?
9	281.40	0.86	6.3 ± 0.2	3.6 ± 0.7	GS 1843+009[b]	HMXB, TP
10	287.79	0.56	4.1 ± 0.2	1.3 ± 0.6[f]	Aql X-1[b]	LMXB, TBA
11	289.69	−5.24	5.2 ± 0.2	1.4 ± 0.8[f]	4U1916–053	LMXB, B
12	285.41	1.45	3.6 ± 0.2	3.1 ± 0.6	XTE J1901+014	?
13	282.10	−3.16	4.3 ± 0.2	3.9 ± 0.8	IGR J18483–031	?
14	274.03	−14.02	42.9 ± 2.4	3.2 ± 8.1[f]	GX 17+2	LMXB, ZB
15	287.22	9.35	2.9 ± 0.2	4.4 ± 0.6	XTE J1908+094	HMXB, BH
16	273.77	−12.12	20.6 ± 1.7	24.0 ± 5.8	M1812–12	LMXB, B
17	282.08	−2.48	2.7 ± 0.2	1.7 ± 0.9[f]	A1845–024	HMXB, TP
18	283.25	−8.70	2.6 ± 0.3	3.7 ± 1.1	4U1850–087	LMXB, GB
19	279.50	−6.91	2.7 ± 0.4	1.8 ± 1.1[f]	AX J183800–0655	?
20	280.37	−4.94	2.1 ± 0.3	6.8 ± 0.9	1E1841–045	AXP, SNR
21	281.61	−2.97	1.6 ± 0.2	3.4 ± 0.8	PSR J1846–0258	P, SNR
22	295.60	−10.36	4.1 ± 0.6	4.6 ± 2.1[f]	NGC 6814	AGN
23	282.25	−0.00	1.4 ± 0.2	0.6 ± 0.7[f]	IGR J18490–0000[c]	?
24	276.32	−0.03	2.2 ± 0.3	0.5 ± 1.1[f]	4U1822–000	LMXB
25	280.23	−5.65	2.0 ± 0.3	1.7 ± 1.0[f]	IGR J18406–0539[c]	?
26	281.25	−4.58	1.5 ± 0.3	1.7 ± 0.9[f]	IGR J18450–0435[c]	?
27	294.46	−6.28	1.7 ± 0.3	1.1 ± 1.1[f]	SS442/1H1934–063[d]	AGN
28	278.40	−10.58	3.1 ± 0.6	4.6 ± 2.1[f]	SNR 21.5–0.9	SNR
29	278.12	−7.93	1.6 ± 0.5	1.1 ± 1.5[f]	IGR J18325–0756[e]	?
30	283.48	7.45	0.6 ± 0.2	0.5 ± 0.7[f]	IGR J18539+0727[e]	BH?

[a] The table lists only statistical errors (the systematic error is ∼10%).
[b] Sources observed during outbursts (Molkov *et al*. 2003; Cherepashcuk *et al*. 2003a, 2003b).
[c] Sources discovered in these observations.
[d] Observed position of this source differs from the more accurate position of SS 442 by ∼5′.6; it may well be that this is a new object, IGR J19378–0617 (see text).
[e] Sources discovered by the IBIS telescope in other observations of the INTEGRAL observatory.
[f] Sources undetectable at a statistically significant level.

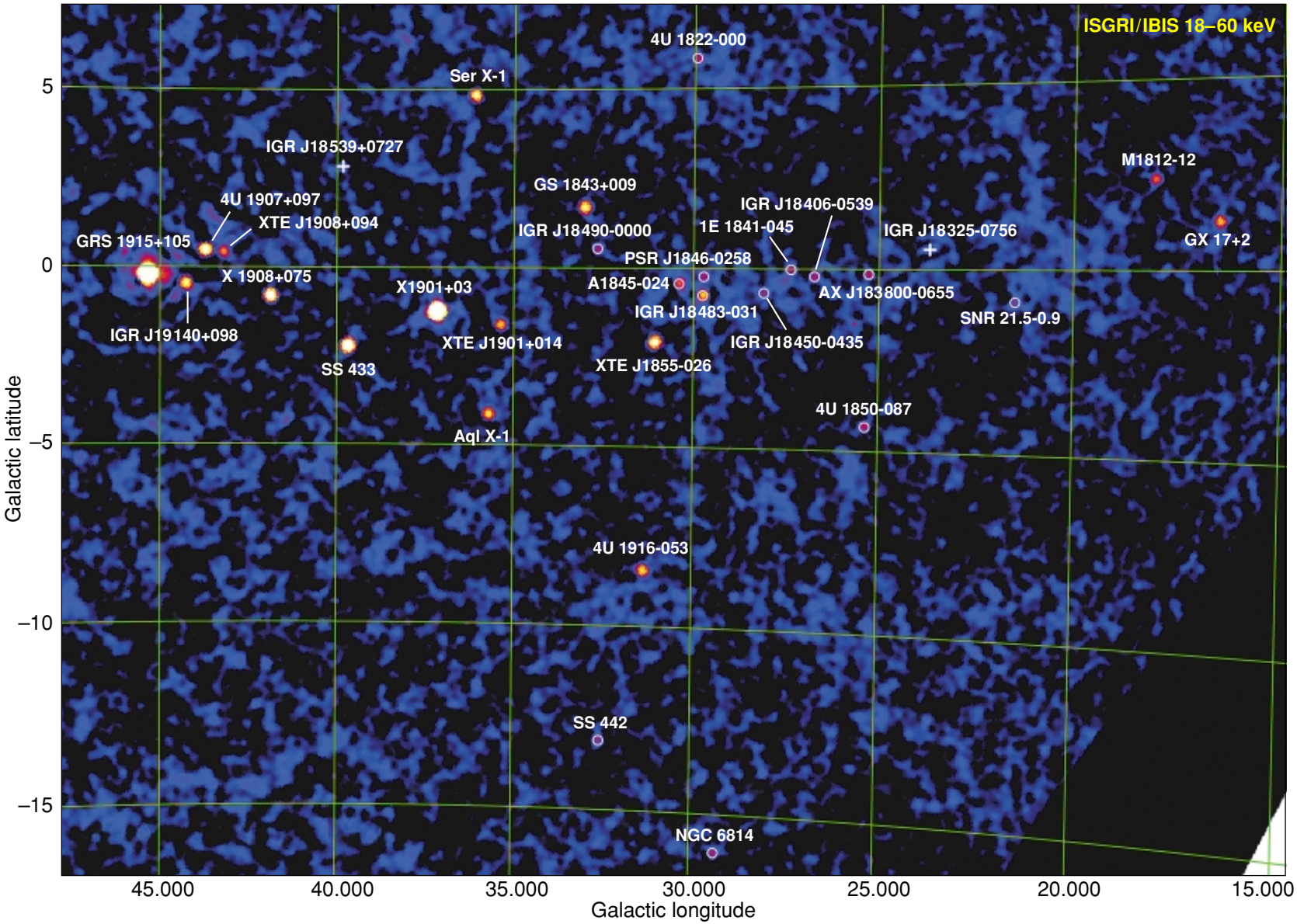

Fig. 2. Map of the Sagittarius Arm tangent obtained with the IBIS telescope of the INTEGRAL observatory in the energy range 18–60 keV. The total exposure time is ~830 ks.

study. Therefore, we cannot completely rule out the probability of short-duration bursts of other transient sources that are undetectable in these images.

ACKNOWLEDGMENTS

We would like to thank E.M. Churazov, who developed the algorithms for IBIS data analysis and provided the software. This work was supported by the Ministry of Industry and Science of Russia (RF Presidential Grant no. NSh-2083.2003.2) and the Nonstationary Phenomena in Astronomy Program of the Russian Academy of Sciences. K.A. Postnov wishes to thank the Russian Foundation for Basic Research (project no. 03-02-16110) for its support. We would like to thank the Swiss INTEGRAL Science Data Center (Versoix, Switzerland) and the Russian INTEGRAL Science Data Center (Moscow, Russia). The results of this work are based on observations of the INTEGRAL observatory, an ESA project with the participation of the Czech Republic, Denmark, France, Germany, Italy, Poland, Spain, Switzerland, Russia, and the United States.

REFERENCES

1. A. M. Cherepashchuk, S. Molkov, L. Foschini, *et al.*, Astron. Telegram, No. 159 (2003a).
2. A. M. Cherepashchuk, R. A. Sunyaev, F. Seifina, *et al.*, Astron. Astrophys. **411**, L441 (2003b).
3. M. Chernyakova, A. Lutovinov, F. Capitanio, *et al.*, Astron. Telegram, No. 157 (2003).
4. N. A. Eismont, A. V. Ditrikh, G. Janin, *et al.*, Astron. Astrophys. **411**, L37 (2003).
5. W. Forman, H. Tananbaum, and C. Jones, Astrophys. J. **205**, L29 (1976).
6. D. Galloway, R. Remillard, and E. Morgan, IAU Circ., No. 8070 (2003a).
7. D. Galloway, R. Remillard, and E. Morgan, IAU Circ., No. 8081 (2003b).
8. D. C. Hannikainen, J. Rodriguez, K. Pottschmidt, *et al.*, IAU Circ., No. 8088 (2003a).
9. D. C. Hannikainen, O. Vilhu, J. Rodriguez, *et al.*, Astron. Astrophys. **411**, L415 (2003b).
10. F. Lebrun, J. P. Leray, P. Lavocat, *et al.*, Astron. Astrophys. **411**, L141 (2003).
11. A. A. Lutovinov and M. G. Revnitsev, Pis'ma Astron. Zh. **29**, 810 (2003) [Astron. Lett. **29**, 719 (2003)].
12. A. Lutovinov, J. Rodriguez, N. Produit, *et al.*, Astron. Telegram, No. 151 (2003a).
13. A. Lutovinov, S. Shaw, L. Foschini, *et al.*, Astron. Telegram, No. 154 (2003b).
14. S. V. Molkov, A. A. Lutovinov, and S. A. Grebenev, Astron. Astrophys. **411**, L357 (2003).
15. M. G. Revnitsev, R. A. Sunyaev, D. A. Varshalovich, *et al.,* Pis'ma Astron. Zh. **30**, 426 (2004); astro-ph/0402027.
16. L. Wen, R. A. Remillard, and H. V. Bradt, Astrophys. J. **532**, 1119 (2000).
17. C. Winkler, T. J.-L. Courvoisier, G. Di Cocco, *et al.*, Astron. Astrophys. **411**, L1 (2003).

Translated by G. Rudnitskii

Astronomy Letters, Vol. 30, No. 8, 2004, pp. 540–548. Translated from Pis'ma v Astronomicheskiĭ Zhurnal, Vol. 30, No. 8, 2004, pp. 596–604.

Observations of the X-ray Pulsar GX 301-2 with the ART-P Telescope of the Granat Observatory

S. S. Tsygankov[1], A. A. Lutovinov[1*], S. A. Grebenev[1], M. R. Gilfanov[1,2], and R. A. Sunyaev[1,2]

[1] *Space Research Institute, Russian Academy of Sciences, Profsoyuznaya ul. 84/32, Moscow 117810, Russia*

[2] *Max Planck Institut für Astrophysik, Karl Schwarzschild Str. 1, Postfach 1317, D-85741 Garching bei München, Germany*

Received February 15, 2004

Abstract—The variability of the X-ray flux from the pulsar GX 301-2 is analyzed by using data from the ART-P telescope of the GRANAT Observatory. The intensity variations with time scales of several thousand seconds are studied at various orbital phases. The high-state flux from the source exceeds its low-state flux by as much as a factor of 10. The hardness and spectrum of the source are shown to change greatly with its intensity. These intensity variations are most likely caused by substantial inhomogeneities in the stellar wind from the companion star. © *2004 MAIK "Nauka/Interperiodica".*

Key words: *pulsars, neutron stars, X-ray sources.*

INTRODUCTION

The X-ray pulsar GX 301-2, which forms a binary system with the blue supergiant Wray 977 with an eccentricity of ~0.462 and an orbital period of ~41.5 (Sato *et al.* 1986), is one of the longest-period pulsars known to date. Throughout the history of its observation, the spin period of this source has repeatedly undergone abrupt changes. In April 1984, the Tenma satellite measured the maximum pulsation period, 701.14 s (Sato *et al.* 1986), which decreased sharply to ~677 s in 1992 (Lutovinov *et al.* 1994; Chichkov *et al.* 1995). At this point, however, the period of prolonged steady spin-up with a mean rate of $\dot{P}/P \sim -4.4 \times 10^{-3}$ yr^{-1} ended, and the pulsation period stabilized at ~679.5 s in November 1996 (Pravdo *et al.* 2001). On smaller time scales, the switches between the spin-up and spin-down of the neutron star manifest themselves much more frequently (Chichkov *et al.* 1995; Koh *et al.* 1997). The X-ray flux recorded from the binary is variable during the orbital cycle. As the pulsar approaches the optical star, the X-ray luminosity of the binary increases and reaches its maximum 1.2 days before periastron passage (White *et al.* 1984). An increase in the intensity of the source is also observed near the apoastron (Chichkov *et al.* 1995; Koh *et al.* 1997).

Parkes *et al.* (1980) determined the parameters of the optical star (its radius ~$43R_\odot$ and mass ~$30M_\odot$) and the distance to the binary system ($d \sim 1.8$ kpc). Note that the precise spectral type of the companion star has not yet been firmly established. Some authors classify it as a B star (Vidal 1973; Kaper *et al.* 1995), while others (Parkes *et al.* 1980) classify it as an emission-line Be star. The normal star can occupy an intermediate position and occasionally switches over from one state to another.

At present, there is no agreement about the structure and distribution of the matter in the binary GX 301-2/Wray 977 either. Based on the very small changes in the characteristic values of these parameters with pulse phase, Tashiro *et al.* (1991) concluded that the distribution of the photoabsorbing and iron line emitting matter was spherically symmetric. On the other hand, having performed detailed phase-resolved spectroscopy, Leahy *et al.* (1990) concluded that the distribution of the matter around the neutron star was nonuniform. All authors point out a significant hydrogen column density reaching ~2×10^{24} cm^{-2}.

In this paper, we present the results of a comprehensive analysis of the observational data for the pulsar GX 301-2 obtained with the ART-P telescope of the Granat orbital observatory, identifying two distinct (high and low) states in its light curve.

OBSERVATIONS

The X-ray pulsar GX 301-2 was observed by the Granat observatory from January 1991 through February 1992. Over this period, the ART-P telescope conducted four observing sessions for this source with a total useful time of ~97 ks (see Table 1).

*E-mail: aal@hea.iki.rssi.ru

Table 1. ART-P observations of the pulsar GX 301-2 during the period 1991–1992[a]

Date	Orbital phase	Exposure time, s	Flux, mCrab	L_X,[b] 10^{36} erg s^{-1}	Period, s
Jan. 9, 1991	0.03–0.04	23584			682.83 ± 0.04
(I)		2835	32 ± 8	0.29 ± 0.07	
(II)		6126	301 ± 8	2.72 ± 0.08	
(III)		7067	126 ± 6	1.14 ± 0.05	
(IV)		7556	420 ± 9	3.81 ± 0.08	
Aug. 13, 1991	0.23–0.24	33346	–[c]	–[c]	678.91 ± 0.43
Jan. 29, 1992	0.31	11376	28 ± 5	0.26 ± 0.05	678.77 ± 1.82
Feb. 7, 1992	0.52–0.53	28540			676.83 ± 0.08
(I)		986	198 ± 21	1.80 ± 0.19	
(II)		13965	37 ± 5	0.33 ± 0.04	
(III)		13589	167 ± 6	1.51 ± 0.06	

[a] In the energy range 6–40 keV.
[b] For the assumed distance to the source of $d = 1.8$ kpc.
[c] For technical reasons, the spectrum of the source cannot be reconstructed.

The ART-P X-ray telescope consists of four coaxial, completely independent modules, each of which includes a position-sensitive detector with a geometrical area of 625 cm^2 and a coded mask. The telescope is sensitive to photons in the energy range 2.5–60 keV (the energy resolution is ~22% in the 5.9-keV calibration iron line) and can image the sky within a $3.^\circ4 \times 3.^\circ6$ field of view with a nominal angular resolution of ~5 arcmin (the angular size of the mask element). For a more detailed technical description of the telescope, see Sunyaev *et al.* (1990).

The observations were carried out in a photon-by-photon mode in which the coordinates of each photon on the detector, its energy (1024 channels), and arrival time (the photon arrival time was accurate to within 3.9 ms, and the dead time was 580 μm) were written into the ART-P buffer memory. This mode allows both timing and spectral analyses of the emission from each X-ray source within the ART-P field of view to be performed. Data were transferred to the main memory after the temporary buffer was filled (once in 200–250 s, the exposure time) during ~25–30 s, which led to gaps in information.

All of the observations of the pulsar GX 301–2 were performed by the third ART-P module with a reduced sensitivity to soft (3–8 keV) energies. Subsequently, this complicated (and, in several cases, did not allow) a spectral analysis of the X-ray emission.

TIMING ANALYSIS

Our studies showed that the flux from GX 301-2 near the periastron and apoastron is highly variable. Two states, high and low, can be arbitrarily identified; the switches between them can occur several times during one observing session. Figure 1a shows the light curves of the pulsar for all four observing sessions. The hardness, which is defined as the ratio of the fluxes from the source in the energy ranges 30–40 and 10–20 keV, is given for each light curve (Fig. 1b).

We see from the figure that the switches of the source from the low state to the high and back are rapid; its intensity during such switches changes by about an order of magnitude. At the same time, the hardness of the source during the switch to its high state decreases (by a factor of ~3). Note that, although the absolute stability of the low-state intensity is higher than that of the high-state intensity (as is illustrated in Fig. 1), the fractional rms of these variations are close. Thus, the fractional rms during periastron passage changed from ~21 to ~34% in the low and high states, respectively; near the apoastron,

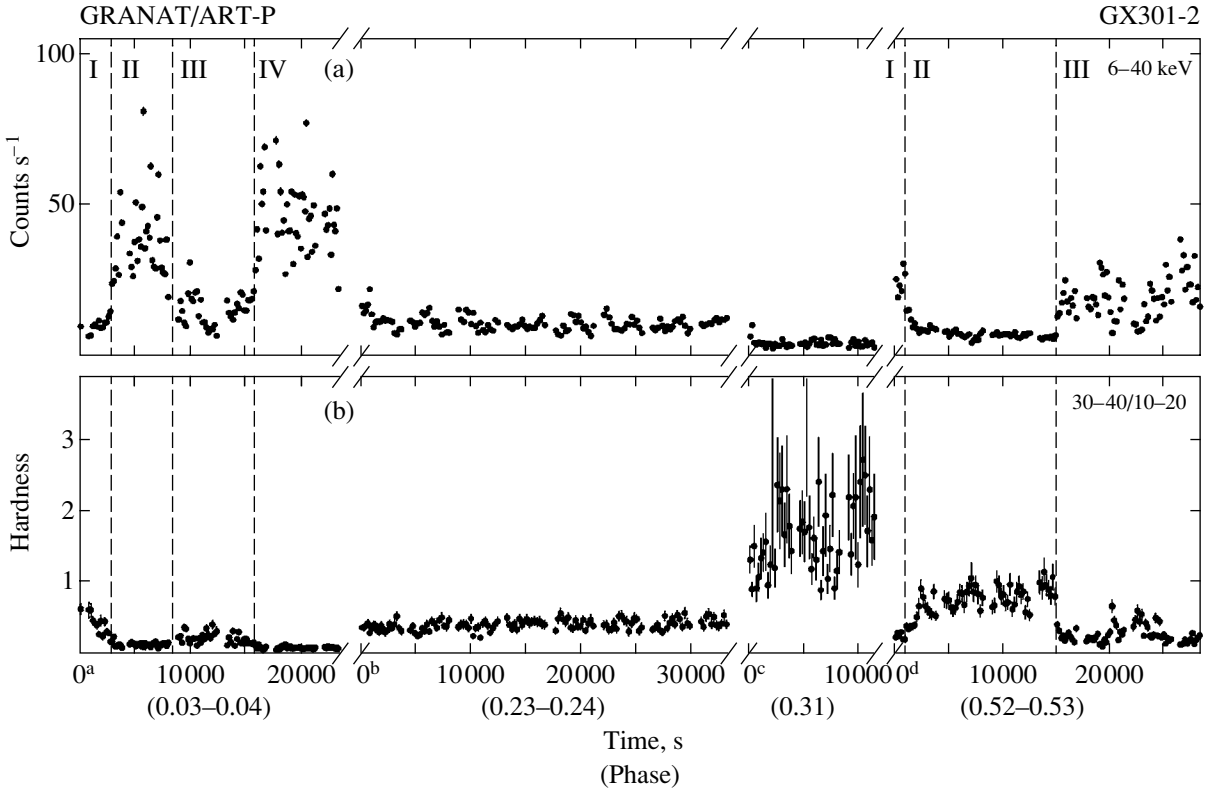

Fig. 1. Light curve for the pulsar GX 301-2 (a) in the energy range 6–40 keV for four observing sessions and the corresponding variations in the hardness of the source; (b) the ratio of the count rates in the energy ranges 30–40 and 10–20 keV (the background is subtracted). The dashed lines mark the boundaries of the low and high states. Time in seconds from the beginning of the observing session is along the horizontal axis. Zeros correspond to the following times: 0^a, UT $18^h34^m05.502^s$ (January 9, 1991); 0^b, UT $09^h57^m32.519^s$ (August 13, 1991); 0^c, UT $17^h15^m16.208^s$ (January 29, 1992); 0^d, UT $18^h16^m06.201^s$ (February 7, 1992). The corresponding orbital phase is given in parentheses for each session. The errors correspond to one standard deviation.

its values were ~25 and ~35% for the low and high states, respectively. Near an orbital phase of ~0.3, the fractional rms was ~34%.

Table 1 gives the pulsation periods determined by a superposed-epoch analysis after correction of the photon arrival time for the motion of the neutron star in the binary system and for the motion of the Earth and the spacecraft. Throughout our observations (about 13 months), the period decreased by ~6 s, which corresponds to a mean value of $\dot{P}/P \approx -8.2 \times 10^{-3}$ yr^{-1}.

We analyzed the behavior of the pulse profile and the pulse fraction for the source as a function of its state and the energy range. Figure 2 shows the phase light curves of the pulsar averaged over each of the sessions in five energy ranges (3–6, 6–10, 10–20, 20–30, and 30–40 keV). The pulse profile has a double-peaked shape with a slight dominance of the first peak; the intensity of the second peak increases relative to the first peak as the energy increases. During the source's switches from one state to the other, the pulse shape remains virtually unchanged, only the intensity of the emission changes.

The pulse fraction, which is defined as $P = (I_{max} - I_{min})/(I_{max} + I_{min})$, where I_{max} and I_{min} are the background-corrected count rates at the maximum and minimum of the pulse profile, is given in Table 2 for all observing sessions in various energy ranges (6–10, 10–20, 20–30, 30–40, and 6–40 keV) as a function of the source's state. In view of the technical peculiarities of the third module described above, the pulse fraction in the energy range 3–6 keV was not calculated.

It follows from the table that the pulse fraction remains fairly high and depends weakly on the energy range and the source's intensity, although the pulsations in the energy range 30–40 keV are slightly blurred and the pulse fraction slightly decreases in the energy range 10–20 keV. As the source passed through the apoastron (February 7, 1992), its pulsations completely disappeared when it was in the low

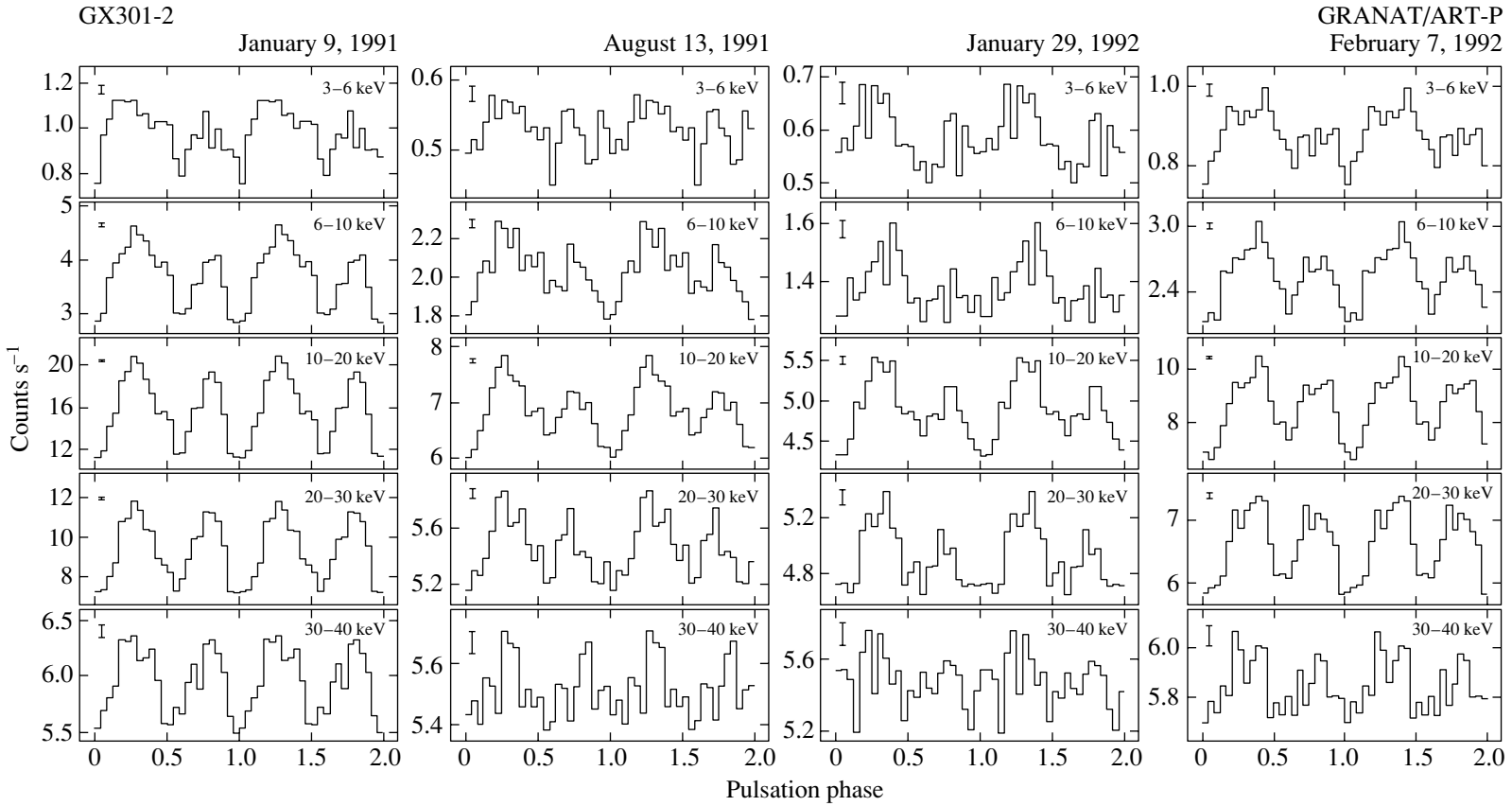

Fig. 2. ART-P pulse profiles for GX 301-2 in various energy ranges. The errors correspond to one standard deviation.

Table 2. Pulse fractions for GX 301–2

Date	Pulse fraction, %				
	6–10 keV	10–20 keV	20–30 keV	30–40 keV	6–40 keV
Jan. 9, 1991					
I	—[a]	—[a]	—[a]	—[a]	—[a]
II	60.9 ± 4.9	55.2 ± 2.1	61.5 ± 3.4	35.9 ± 7.1	54.9 ± 1.8
III	78.5 ± 10.6	63.0 ± 3.3	83.6 ± 8.9	35.6 ± 7.2	64.2 ± 3.2
IV	36.6 ± 2.2	32.6 ± 1.3	43.3 ± 2.9	33.9 ± 6.6	34.2 ± 1.1
Aug. 13, 1991	58.6 ± 7.7	47.4 ± 3.2	50.6 ± 7.9	20.9 ± 6.3	44.7 ± 3.0
Jan. 29, 1992	$91.1^{+8.9}_{-38.9}$	76.8 ± 13.4	—[b]	—[b]	82.8 ± 15.4
Feb. 7, 1992					
I	—[a]	—[a]	—[a]	—[a]	—[a]
II	44.3[c]	19.9[c]	24.9[c]	15.5[c]	15.2[c]
III	44.7 ± 3.4	53.5 ± 1.9	61.4 ± 4.1	82.1 ± 24.8	53.3 ± 1.8

[a] Cannot be determined because of poor statistics.
[b] Cannot be determined for technical reasons.
[c] The 3σ upper limit.

state. For this case, the table gives only upper limits on the pulse fraction.

SPECTRAL ANALYSIS

To study the properties of the pulsar GX 301-2 in detail, we performed a spectral analysis of its emission in different states. The main model used in our analysis was a simple power law that is most characteristic of X-ray pulsars at energies up to ~10–15 keV. However, we did not always use this simple model. As required, we used various modifications of the model that were specified in general form by the equation

$$I(E) = I_{10}\left(\frac{E}{10\ \mathrm{keV}}\right)^{-\alpha}\exp(-\sigma_A N_{\mathrm{H}}) \quad (1)$$
$$\times\begin{cases} 1, & \text{if } E < E_{\mathrm{c}} \\ \exp\left[-(E-E_{\mathrm{c}})/E_f\right], & \text{if } E \geq E_{\mathrm{c}}, \end{cases}$$

where E is the photon energy in keV, I_{10} is the normalization of the power-law component to 10 keV, α is the photon spectral index, E_{c} is the cutoff energy, E_f is the e-folding energy in the source's spectrum, N_{H} is the hydrogen column density, and $\sigma_A(E)$ is the interstellar absorption cross section.

This model includes both the low-energy cutoff attributable to photoabsorption and the purely empirical multiplicative component that is commonly used to describe the spectra of X-ray pulsars, the high-energy cutoff (White *et al.* 1983). Formally, photoabsorption was recorded only in one session on January 9, 1991, when the source was in the low state. In this case, the hydrogen column density was $N_{\mathrm{H}} = (7.9 \pm 3.2) \times 10^{23}$ cm^{-2}. Such a high value agrees well with the results by Haberl (1991), who performed a detailed analysis of the photoabsorption at various orbital phases. We failed to perform a more detailed analysis of this parameter due to the technical problems of the third ART-P module discussed above and obtained only upper limits for the remaining observing sessions (see Table 3).

Based on the $\Delta\chi^2$ test, we passed to a more complex model. The model was assumed to be acceptable if the probability that the χ^2 value did not improve by chance exceeded 95%. Table 3 gives the best-fit parameters for the pulsar's spectra averaged over the period of the observing session under consideration that corresponded a certain state of the source.

As we see from Table 3, the high-state spectrum of the source is slightly softer than its low-state spec-

Table 3. Best-fit parameters for the spectrum of GX 301-2[a]

Date	I_{10}[b],10^{-3}	α	E_c	E_f	N_H, 10^{23} cm^{-2}	$\chi^2_N(N)$[c]
Jan. 9, 1991						
(I)	1.26 ± 1.06	0.32 ± 0.73			8.4[d]	1.11(7)
(II)	15.76 ± 0.75	0.85 ± 0.10	22 ± 3	23 ± 13	0.4[d]	1.19(17)
(III)	13.15 ± 3.40	1.77 ± 0.34			7.9 ± 3.2	1.73(15)
(IV)	21.02 ± 0.76	0.71 ± 0.06	28 ± 2	11 ± 5	0.3[d]	2.72(13)
Jan. 29, 1992	1.66 ± 0.97	1.53 ± 0.65			2.9[d]	0.21(5)
Feb. 7, 1992						
(I)	9.10 ± 2.13	0.76 ± 0.31			3.0[d]	0.90(8)
(II)	1.46 ± 0.69	0.59 ± 0.39			4.7[d]	1.18(8)
(III)	10.22 ± 0.77	1.04 ± 0.24	16 ± 3	31 ± 13	0.7[d]	0.79(16)

[a] All errors are given at the 1σ level.
[b] The flux at 10 keV (phot. cm^{-2} s^{-1} keV^{-1}).
[c] The χ^2 value normalized to the number of degrees of freedom N.
[d] The 1σ upper limit on the atomic hydrogen column density.

trum. The cutoff energy E_c as well as the e-folding energy E_f remain constant, within the error limits, and are in good agreement with the results of other authors (Leahy *et al.* 1990). However, they show up only in the high state, which may be attributable to poor statistics when analyzing the emission from the source in its low state. Figure 3 shows how the energy spectrum changes with the source's state.

DISCUSSION

Despite the abundance of observational data, the precise accretion pattern in the binary system GX 301-2/Wray 977 that would account for the nature of its X-ray emission is not yet completely clear. The source exhibits variable emission, it behaves in a new fashion from orbit to orbit, and the intensity peaks and minima shift, occasionally replacing one another (except for the peaks near the periastron and apoastron, although their intensities also vary significantly).

Several models of the interaction of a compact object with interstellar matter in a binary system have been suggested to interpret the observational data. Pravdo *et al.* (1995) showed that the periodic outbursts were difficult to explain only by isotropic accretion from the stellar wind and explained this behavior of the source either by the interaction of the neutron star with an equatorially enhanced stellar wind typical of Be stars or by the formation of an accretion disk around the neutron star, which may also be a source of angular momentum, causing it to spin up. Leahy *et al.* (2002) presented the results of a long-term monitoring of GX 301-2 and considered several possible models for the generation of emission, with the wind+stream model yielding the best fit to the experimental data.

The hydrodynamic simulations of a nonaxisymmetric gas stream in the binary system GX 301-2/Wray 977 by Taam and Fryxell (1989) revealed significant aperiodic luminosity fluctuations (with a factor as large as 10) on time scales on the order of several thousand seconds. Tashiro *et al.* (1991) studied the aperiodic intensity variations of GX 301-2 that could be the result of plasma turbulence near the neutron-star surface and that manifest themselves on time scales of up to several tens of seconds.

The intensity variations considered here are also aperiodic in pattern and are observed on time scales from several tens of seconds to several hours (see Fig. 1). The observed intensity fluctuations of the source under study on short time scales are most likely attributable to local inhomogeneities in the stellar wind, its clumpy structure. Of particular interest is

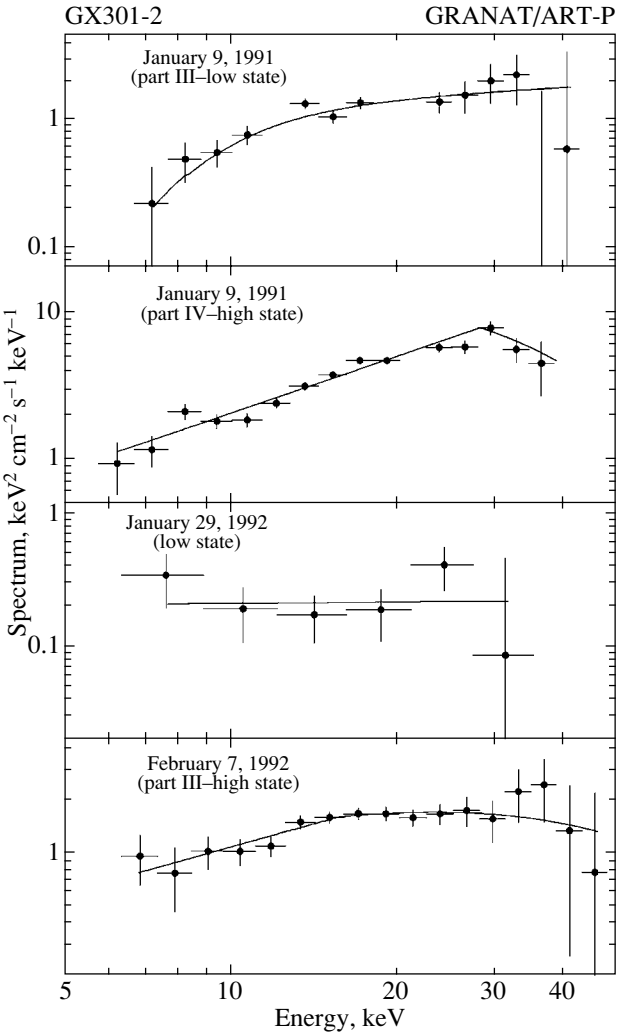

Fig. 3. ART-P energy spectra for GX 301-2. The solid lines represent the model fits to the spectra (see Table 3). The errors correspond to one standard deviation.

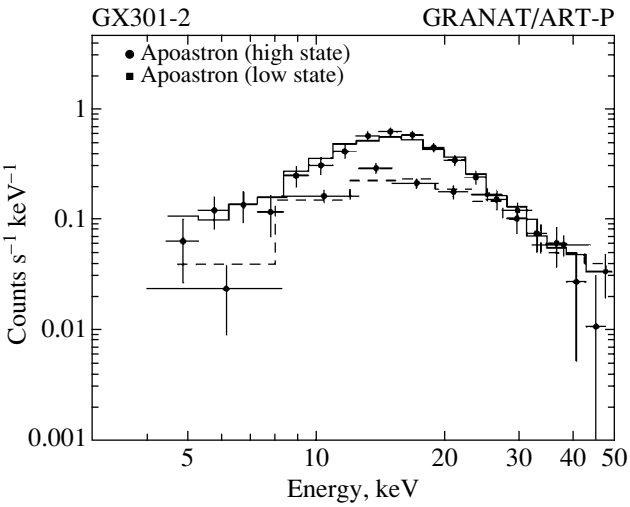

Fig. 4. Spectral evolution of the pulsar GX 301-2 near the apoastron, as inferred from the ART-P data obtained on February 7, 1992. The normalization of the low-state spectrum was multiplied by a factor of 2.6. The power law fits to the high-state (solid lines) and low-state (dashed lines) spectra are indicated by histograms. The errors correspond to one standard deviation.

the observing session near the apoastron on February 7, 1992, when a prolonged decrease in the intensity of the source and the disappearance of pulsations were recorded (part II of the last light curve in Fig. 1).

A plausible explanation of the observed intensity decrease is the eclipse of the neutron star by a substantial inhomogeneity in the stellar wind on the line of sight between the observer and the object. Let us attempt to estimate its characteristic parameters. Following Castor *et al.* (1975), we can write

$$v_w(r) = v_\infty \left(1 - \frac{R_c}{r}\right)^\beta, \qquad (2)$$

where v_∞ is the terminal velocity of the stellar wind, R_c is the radius of the optical companion, and $\beta = 0.5$. Assuming the characteristic time the source stays in its low state to be $\sim$10 ks and the range of possible wind terminal velocities to be from $v_\infty =$ 400 km s^{-1} (Kaper *et al.* 1995) to 1000 km s^{-1} (Parkes *et al.* 1980), we obtain the size of the inhomogeneity $l = 5{-}12R_\odot$ from formula (2). In our case, the terminal velocity of the stellar wind was calculated near the apoastron, which corresponds to a distance of $\sim 5R_c$ from the optical companion (Sato *et al.* 1986). Since the orbital velocity of the neutron star, $\leq$100 km s^{-1}, is low compared to the terminal velocity of the wind, we disregarded it. Note that the source switches to and from its low state not abruptly, but over several (4–5) exposures (Fig. 1); i.e., the duration of this switch is $\sim$800–1000 s. Thus, the boundaries of the inhomogeneity are slightly blurred and are $\sim$15–20% of its total size.

Figure 4 shows the pulse height spectra of the pulsar GX 301-2 obtained for its low and high states during the observations on February 7, 1992. The normalization of the low-state spectrum was multiplied by a factor of 2.6 to match it to the high-state spectrum at energies above $\sim$25 keV, where these spectra have approximately the same shape. We see that the low-state spectrum in softer energy channels exhibits a cutoff. Taking into account this spectral feature attributable to photoabsorption, we can estimate the atomic hydrogen column density at the time in question, $N_H \sim 1.7 \times 10^{24}$ atoms cm^{-2}. Assuming the size of the inhomogeneity to be $l \sim 10R_\odot$, we determined its electron density, $n = N_H/l \sim 2.4 \times 10^{12}$ cm^{-3}.

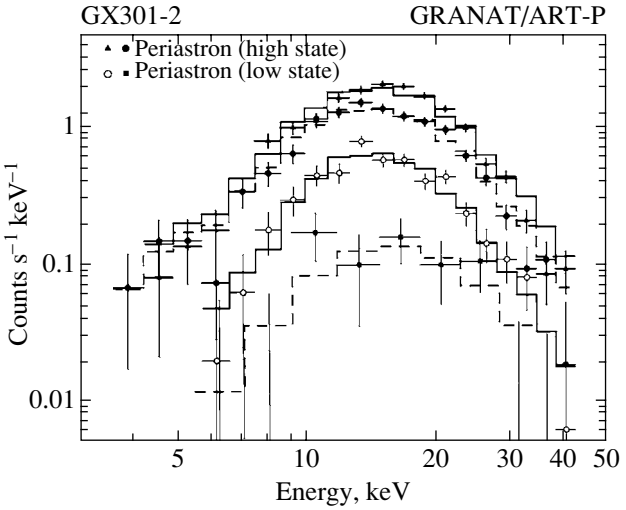

Fig. 5. Spectral evolution of the pulsar GX 301-2 near the periastron, as inferred from the ART-P data obtained on January 9, 1991. The power law fits to the high-state (solid lines) and low-state (dashed lines) spectra are indicated by histograms. The errors correspond to one standard deviation.

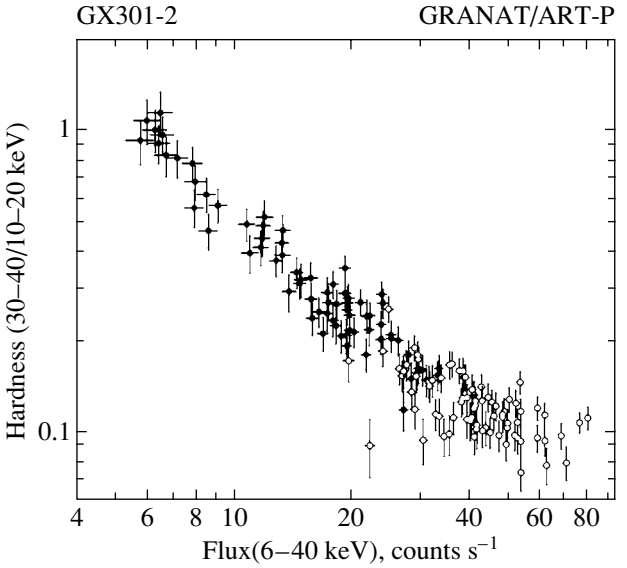

Fig. 6. Hardness of the source versus its intensity during periastron passage on February 7, 1992 (filled circles), and apoastron passage on January 9, 1991 (open circles).

For comparison, Fig. 5 shows the pulse height profiles of the pulsar GX 301-2 at orbital phase 0.03–0.04 near the periastron. We see that the shape of the spectra is almost constant and does not depend on the flux. Only their normalization changes, which is indicative of the absence of enhanced (additional) photoabsorption in the low state (although the upper limits given in Table 3 are significant, which is most likely due to the shortage of data in the soft spectral range).

The dipping in the source's spectrum at high energies observed at the apoastron may be attributable to Thomson scattering. The intensity ratio of 2.6 (see above) implies that the scattering optical depth of the condensation under consideration is $\sim$1. The corresponding electron density of the inhomogeneity is $n = \tau/l\sigma_T \sim 2 \times 10^{12}$ cm^{-3} (σ_T is the Thomson scattering cross section) at a size of $l \sim 10R_\odot$, which is in agreement with the above densities of the cloud estimated from the observed absorption at low energies.

Based on a model with an equatorially enhanced stellar wind, Waters *et al.* (1988) showed for several X-ray binary systems with Be stars that the density around such stars varies as

$$n(r) = n_0 \left(\frac{r}{R_c} \right)^{-\gamma}, \qquad (3)$$

where n_0 is the gas density near the surface of the optical star, r is the distance from the star, and γ is a parameter equal to $\sim$3 for most of the stars under consideration.

Using the values of n_0 from the same paper ($\sim 10^{-11}$ g cm^{-3}) and formula (3), we obtain the mean density of the stellar wind in the equatorial disk around the optical companion near the apoastron, $n(5R_c) \sim 8 \times 10^{-14}$ g cm^{-3}, which corresponds to an electron density of $\sim 5 \times 10^{10}$ cm^{-3}.

Our estimates indicate that the inhomogeneities of the scale under consideration are denser than the average equatorial stellar wind characteristic of stars of this spectral type by a factor of about 40–50.

Note that the disappearance of pulsations is rather difficult to explain in terms of our simple model in which the neutron star is eclipsed by an inhomogeneity in the stellar wind with an optical depth $\tau \sim 1$. Following Mendoz and van der Klis (2000), we can roughly estimate the optical depth of a cloud with a size of $l \sim 10R_\odot$ required to decrease the pulse fraction by a factor of $\sim$3 (see Table 2), $\tau \sim 4$. The derived spread in optical depths may be attributable to poor statistics when searching for pulsations and determining the pulse fraction in the low state (particularly in soft energy channels).

To conclude, we present the following interesting fact: the hardness of the source during periastron and apoastron passage is proportional to its intensity (Fig. 6) and can be formally described by the relation $H \propto F^{-\beta}$, where H is the hardness, and F is the flux from the source in mCrab. For the apoastron, this dependence is stronger ($\beta = -1.02 \pm 0.06$, filled circles)

than it is for the periastron ($\beta = -0.47 \pm 0.08$, open circles).

ACKNOWLEDGMENTS

This study was supported by the Russian Foundation for Basic Research (project nos. 02-02-17347 and 04-02-17276) and the Nonstationary Phenomena in Astronomy Program. We wish to thank K.G. Sukhanov, flight director; the staffs of the Lavochkin Research and Production Center, RNIIKP, and the Deep Space Communications Center in Evpatoria; the Evpatoria team of the Space Research Institute (Russian Academy of Sciences); and the team of I.D. Tserenin, and B.S. Novikov, S.V. Blagii, A.N. Bogomolov, V.I. Evgenov, N.G. Khavenson, and A.V. D'yachkov from the Space Research Institute who operated the Granat observatory, provided the scientific planning of the mission, and performed a preliminary telemetry data processing. We also wish to thank the team of M.N. Pavlinsky (Space Research Institute) and the staff of the former Research and Development Center of the Space Research Institute in Bishkek who designed and manufactured the ART-P telescope.

REFERENCES

1. J. I. Castor, D. C. Abbott, and R. I. Klein, Astrophys. J. **195**, 157 (1975).
2. M. A. Chichikov, R. A. Sunyaev, I. Yu. Lapshov, *et al.,* Pis'ma Astron. Zh. **21**, 491 (1995) [Astron. Lett. **21**, 435 (1995)].
3. F. Haberl, Astrophys. J. **376**, 245 (1991).
4. L. Kaper, H. J. G. L. M. Lamers, E. Ruymaerkers, *et al.*, Astron. Astrophys. **300**, 446 (1995).
5. D. Koh, L. Bildsten, D. Chakrabarty, *et al.*, Astrophys. J. **479**, 993 (1997).
6. D. A. Leahy, Astron. Astrophys. **391**, 219 (2002).
7. D. A. Leahy and M. Matsuoka, Adv. Space Res. **10** (2), 95 (1990).
8. A. A. Lutovinov, S. A. Grebenev, R. A. Sunyaev, and M. N. Pavlinsky, Pis'ma Astron. Zh. **20**, 631 (1994) [Astron. Lett. **20**, 538 (1994)].
9. M. Mendoz and M. van der Klis, Mon. Not. R. Astron. Soc. **318**, 938 (2000).
10. G. E. Parkes, K. O. Mason, P. G. Murdin, *et al.*, Mon. Not. R. Astron. Soc. **191**, 547 (1980).
11. S. H. Pravdo, C. S. R. Day, L. Angelini, *et al.*, Astrophys. J. **454**, 872 (1995).
12. S. H. Pravdo and P. Ghosh, Astrophys. J. **554**, 383 (2001).
13. N. Sato, F. Nagase, N. Kawai, *et al.*, Astrophys. J. **304**, 241 (1986).
14. R. A. Sunyaev, S. I. Babichenko, D. A. Goganov, *et al.*, Adv. Space Res. **10** (2), 233 (1990).
15. R. E. Taam and B. A. Fryxell, Astrophys. J. **339**, 297 (1989).
16. M. Tashiro, K. Makishima, T. Ohashi, *et al.*, Mon. Not. R. Astron. Soc. **252**, 156 (1991).
17. N. V. Vidal, Astrophys. J. **186**, 81 (1973).
18. L. B. F. M. Waters, A. R. Taylor, E. P. J. van den Heuvel, *et al.*, Astron. Astrophys. **198**, 200 (1988).
19. N. White, J. Swank, and S. Holt, Astrophys. J. **270**, 771 (1983).
20. N. E. White and J. H. Swank, Astrophys. J. **287**, 856 (1984).

Translated by V. Astakhov

Astronomy Letters, Vol. 30, No. 8, 2004, pp. 549–565. Translated from Pis'ma v Astronomicheskiĭ Zhurnal, Vol. 30, No. 8, 2004, pp. 605–622.

JHKLM Photometry for Carbon Stars

O. G. Taranova* and V. I. Shenavrin

Sternberg Astronomical Institute, Universitetskiĭ pr. 13, Moscow, 119992 Russia

Received February 24, 2004

Abstract—We discuss our *JHKLM* photometry for nine carbon Mira stars, eighteen carbon semiregular variables, and two oxygen Mira stars. For fourteen carbon stars, we present and analyze their infrared light and color curves. For all of the observed objects, we have estimated the optical depths of the circumstellar dust envelopes, the angular diameters of the stars, and their temperatures. © *2004 MAIK "Nauka/Interperiodica"*.

Key words: *stars—variable and peculiar; carbon stars; infrared photometry; circumstellar dust envelopes.*

INTRODUCTION

Since the mid-1980s, we have included several carbon stars in our program of research on circumstellar dust envelopes, among which are two symbiotic systems (UV Aur and NQ Gem), whose cool components are carbon stars, and bright (in the infrared) single objects. An analysis of our *JHKLM* photometry for these stars (Taranova and Shenavrin 1999; Taranova 2000) allowed us, in particular, to estimate the parameters of the carbon stars themselves and their dust envelopes. Our infrared photometry for the unique carbon star RW LMi showed that its radiation matches the radiation of a star similar to a normal M5 giant surrounded by a dust envelope with a (graphite) grain temperature of ~1000 K and an optical depth of at least 1.7 at a wavelength of 1.25 μm. The infrared radiation of the symbiotic system UV Aur can be represented as the radiation of a star similar to a normal M5 giant surrounded by a dust envelope with a (graphite) grain temperature of ~750 K and an optical depth of about 0.35 at 1.25 μm.

In 2000, to further study cool stars and circumstellar dust envelopes, we expanded our list to include twenty nine objects: twenty seven carbon stars and two oxygen Mira stars.

In this paper, we present our *JHKLM* photometry for these stars performed from 2000 until 2003.

OBSERVATIONS

The infrared photometry of carbon stars was performed on the 1.25-m telescope at Crimean Station of the Sternberg Astronomical Institute using a photometer with a liquid nitrogen–cooled photovoltaic InSb detector (Nadzhip *et al.* 1986). The photometer was mounted at the Cassegrain focus of the telescope; the exit aperture was ~12″, and the spatial east–west beam separation after modulation was ~30″. The program stars are listed in Table 1. Column 3 gives the range of V-magnitude variations, column 4 gives the spectral and variability types, and column 5 gives the variability period. These data were taken from the General Catalogue of Variable Stars (GCVS) (Kholopov *et al.* 1985–1990). The standard stars were chosen from the catalog by Johnson *et al.* (1966); their *HLM* magnitudes were estimated using their spectral types and relations from the paper by Koorneef (1983). The error of a single photometric measurement for the carbon stars did not exceed $0^m.01$–$0^m.03$.

Accordingly, the errors in the estimated infrared color indices did not exceed $0^m.1$ for $L-M$ and $0^m.05$ for the color indices that did not include the M-band observations.

Thus, the list of observed stars includes twenty seven carbon stars and two oxygen Mira stars. Among the carbon stars are nine Mira stars, four irregular variables, and fourteen semiregular variables, two of which (UV Aur and NQ Gem) are the cool components of symbiotic systems. Twenty four objects are periodic.

LIGHT AND COLOR CURVES FOR INDIVIDUAL OBJECTS

For each object, we determined the *JHKLM* magnitudes and infrared color indices averaged over the observing period from our observations[1]. Their values

*E-mail: taranova@sai.msu.ru

[1] *JHKLM* photometry can be requested at the following E-mail address: taranova@sai.msu.ru

1063-7737/04/3008-0549$26.00 © 2004 MAIK "Nauka/Interperiodica"

Table 1. List of the observed objects

No.	Object	V	Sp; Variability type	Period
1	ST And	7.7–11.8	C4.3–C6; SRA	328.34
2	VX And	7.6–9.3	C4.5; SRA	369
3	S Aur	8.2–13.3	C4.5; SR	590.1
4	UV Aur	7.4–10.6	C6.2–C8; M	394.42
5	UU Aur	7.83–10	C5.3–C7.4; SRB	234
6	W Cas	7.8–12.5	C7.1; M	405.57
7	X Cas	9.45–13.2	C5.4; M	422.84
8	V CrB	6.9–12.6	C6.2; SR	357.63
9	U Cyg	5.9–12.1	C7.2–C9.2; M	463.24
10	V1426 Cyg	10.8–13.8	C7.2; M	470
11	NQ Gem	7.4–7.99	C6.2; SR+ZAND	70:
12	TU Gem	9.4–12.5	C6.4; SRB	230
13	CW Leo	10.96–14.8	C9.5; M	630
14	RW LMi	12.8–16.5	C4.3; SRA	640
15	T Lyn	8.8–13.5	C5.2–7.1; M	406.0
16	U Lyr	8.3–13.5	C4.5; M	451.72
17	RX Peg	9.7–11.6	C4.4; SRB	629:
18	DY Per	10.6–13.2	C4.5; SRB	792*
19	SY Per	8.7–?	C6.4E; SRA	474
20	X Sge	7–9.7	C6–5; SR	196
21	TU Tau	5.9–9.2	C5.4+A2 III; SRB	190
22	Y Tau	6.5–9.2	C6.5; SRB	241.5
23	BD Vul	9.3–12.7	C6–7.3; M	430
24	SU And	8.0–8.5	C6.4; LC	–
25	UY And	7.4–12.3	C5.4; LB	–
26	TX Aur	8.5–9.2	C5.4 (N3); LB	–
27	NQ Cas	10.6–11.5	C4.5; LB	–
28	EH And	11.2–12.3	M7	187
29	V2108 Oph	6.6–8.8	M7–M9	–

* The periods were taken from the paper by Alksnis *et al.* (2002).

Note: LB—slowly varying irregular late-type variables (as a rule, giants); LC—irregular variable late-type supergiants with a variability amplitude of $\sim 1^m(V)$; M—Mira Ceti variables; SR—semiregular variables (intermediate- and late-type giants or supergiants with a noticeable periodicity); SRA—semiregular variable late-type giants with a stable periodicity; SRB—semiregular variable late-type giants with an indistinct periodicity; ZAND—symbiotic Z And variables.

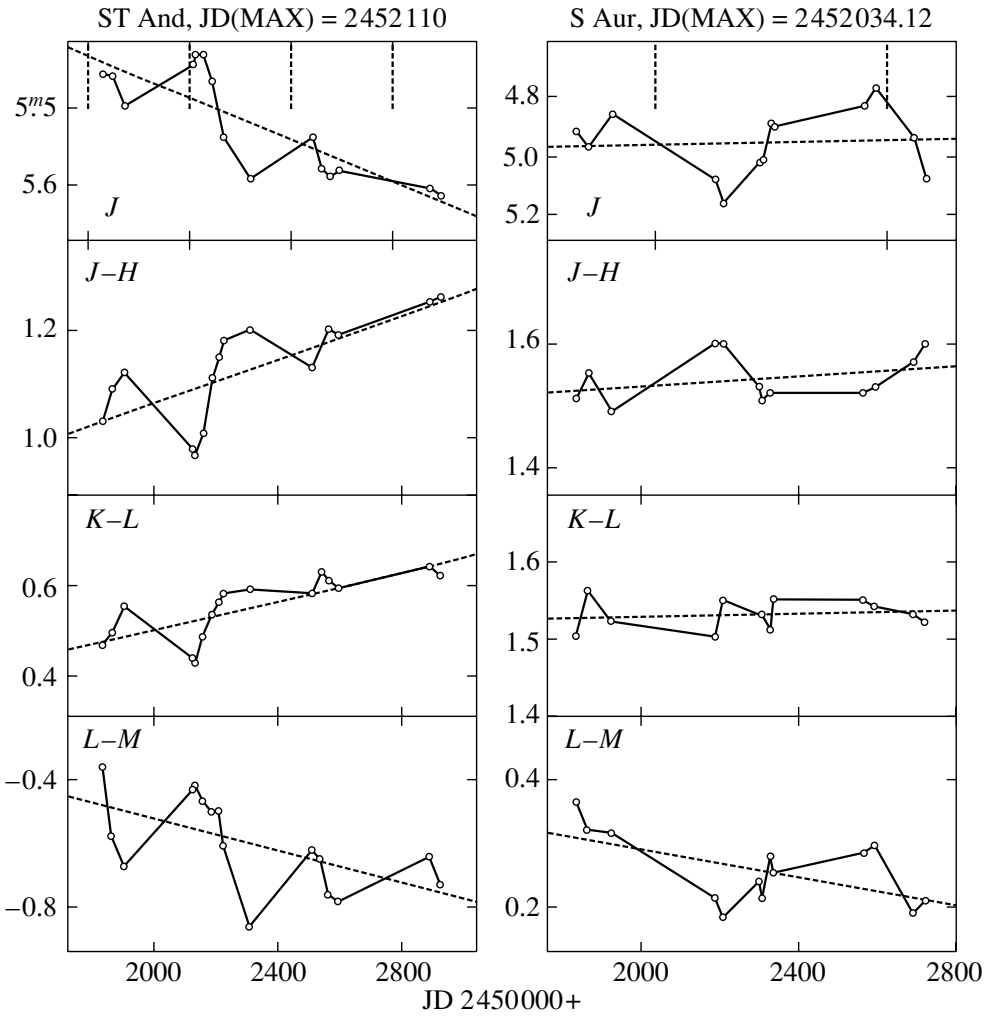

Fig. 1. J light and $J-H$, $K-L$, and $L-M$ color curves for thirteen carbon stars and one oxygen Mira star. The object's name and the epoch of maximum or minimum J brightness are given at the top of each group of panels. The vertical lines indicate the positions of the J-brightness maxima and minima. The dashed straight lines are the regression lines.

are listed in Table 2 together with their standard deviations (sd) and errors (se) and the number of averaged values N (the number of nights on which the object was observed). The asterisk in the first column of Table 2 marks the parameters for which the number of averaged values N is smaller by one.

Analyzing the data of Table 2, we can note the following. The amplitude of the J-magnitude variations in the infrared object CW Leo ($\sigma J \sim 0\overset{m}{.}7$) and the semiregular variable RW LMi ($\sigma J \sim 0\overset{m}{.}7$), which is also an infrared object, was largest among the carbon Mira stars. The oxygen Mira star V2108 Oph exhibited J-magnitude variations within $\sigma J \sim 0\overset{m}{.}7$. For the remaining objects, the J magnitude varied within $\sigma J \sim 0\overset{m}{.}04-0\overset{m}{.}6$

Relatively long series of observations were obtained for fourteen objects from Table 1. Their J light and $J-H$, $K-L$, and $L-M$ color curves are shown in Fig. 1.

ST And. The observations for this object spanned more than three periods. Periodic J-magnitude variations were observed against the background of a linear trend. Over the period of our observations, the J brightness fell by about $0\overset{m}{.}6$, and the star reddened—its $J-H$ ($\Delta(J-H) \sim 0\overset{m}{.}2$) and $K-L$ ($\Delta(K-L) \sim 0\overset{m}{.}15$) color indices increased. The $L-M$ color index decreased. Approximately the same amplitudes of the magnitude and color variations were also observed in the periodic variations; the object reddened at the minimum of the periodic J-magnitude variations. The variations of $L-M$ were in antiphase with those of $J-H$ and $K-L$.

S Aur. The observations spanned slightly more than one period. Periodic J-magnitude variations

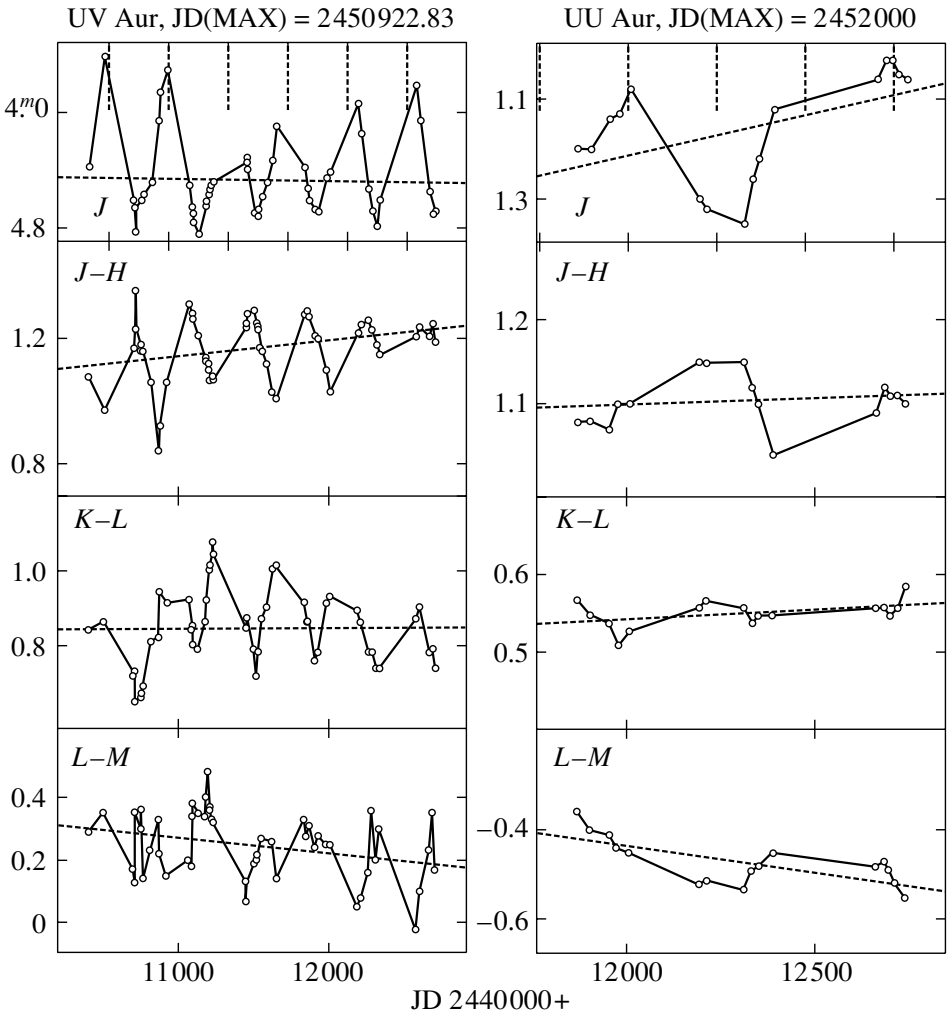

Fig. 1. (Cont.)

were clearly seen; there was no linear trend. The $J-H$ and $K-L$ color indices varied within the error limits. The $L-M$ color index decreased.

UV Aur. The observations spanned about six periods. The J magnitude ($\Delta J \sim 1^m$) and the color indices clearly showed periodic variations. The star reddened at minimum brightness. No trend was observed.

UU Aur. The observations spanned about three periods. The J-magnitude variations were $\sim 0\overset{m}{.}2$, but the 234-day period was not traceable. The positions of the maxima in the J light curve were plotted with the initial epoch JD 2452000 (the presumed J-brightness maximum in Fig. 1). There may be a linear trend in the J-magnitude variations. The color variations were almost within the error limits.

V CrB. The observations spanned about five periods. The star is similar in the pattern of its J-magnitude and $J-H$ and $K-L$ color variations to UV Aur. The variations of $L-M$ were in antiphase with those of $J-H$ and $K-L$ (as in ST And).

T Lyn. The object was observed for about three periods, but all observations were performed at phases close to the minimum. Over the period of our observations, the mean J brightness fell by about $1\overset{m}{.}1$, $J-H$ and $K-L$ were almost constant, and $L-M$ increased.

W Cas. The observations spanned more than two periods. Over the period of our observations, $J-H$ increased from about $0\overset{m}{.}95$ to $1\overset{m}{.}15$, $K-L$ decreased by $0\overset{m}{.}15$, and $L-M$ varied within the error limits.

TU Gem. The observations spanned about four periods. The J-magnitude variations were about $0\overset{m}{.}2$, and the color variations were within the error limits. The positions of the minima in the J light curve were plotted with the initial epoch JD 2452580 (the presumed J-brightness minimum in Fig. 1).

V2108 Oph (an oxygen Mira star). A periodicity of ~600–640 days is clearly seen in Fig. 1. The

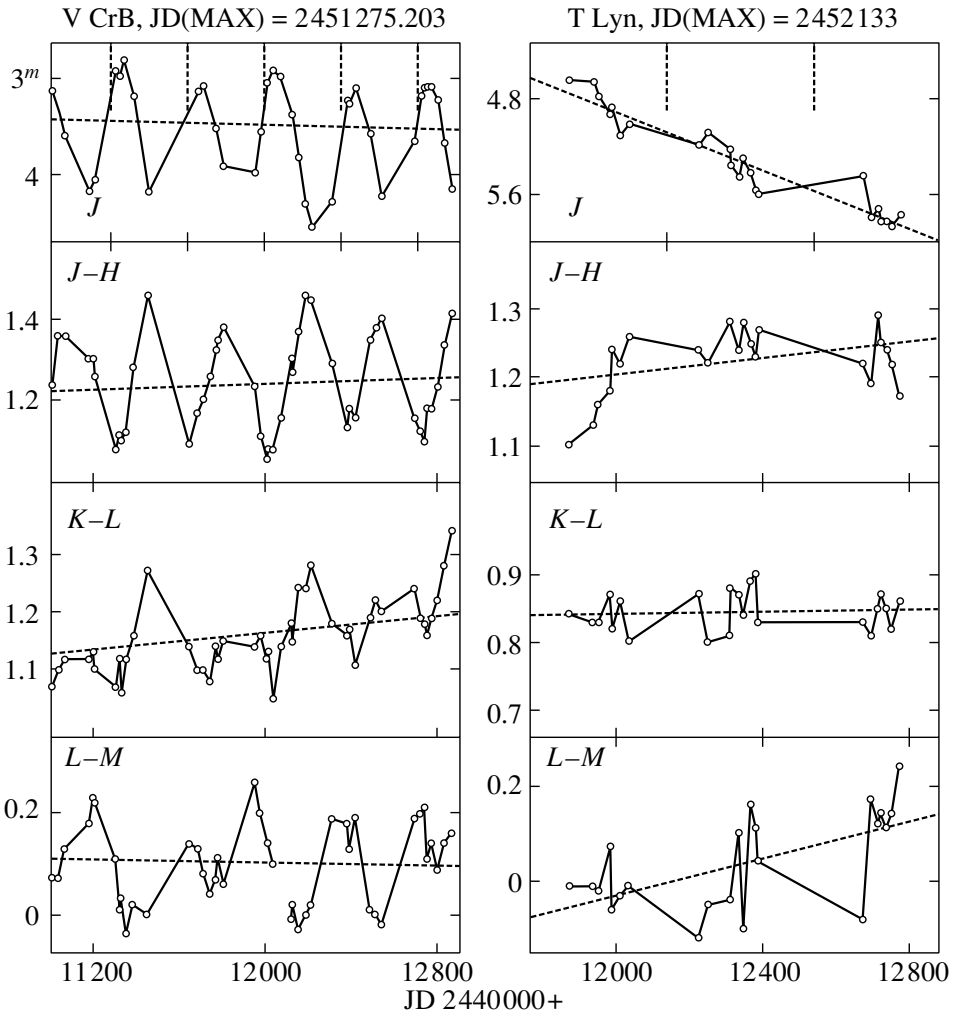

Fig. 1. (Cont.)

positions of the minima in the J light curve were plotted with the initial epoch JD 2452107 (the presumed J-brightness maximum in Fig. 1) and a period of 620 days. The amplitude of the J-magnitude variations was about $1^m.7$. At maximum brightness, the star became hotter. The $J-H$ color index was significantly larger than its values for normal stars; i.e., the star is embedded in a dense dust envelope. If the central star is assumed to be a late-type red star, then the $J-H$ color excess was no less than $0^m.4$ (at maximum J brightness), and the absorption in the dust envelope (with dust grains similar to the interstellar ones) corresponded to $A'_V \sim 4^m$ (or $\tau(1.25\ \mu\text{m}) \sim 0.9$). The color temperature of the star estimated from its $K-L$ color index was ~1100 K at minimum brightness and ~1200 K at maximum. The J brightness averaged over the period of our observations may have increased by about $0^m.3$–$0^m.4$.

CW Leo (IRC+10216). This object has been repeatedly and comprehensively studied over a wide spectral range (see, e.g., Groenewegen 1997). Here, we briefly note some of the photometric features of the object that were observed in the spectral range 1.25–5 μm during 1999–2003 (about two periods). The observed J-magnitude variations were $\sim 1^m.7$ and had a period close to 630 days. The positions of the maxima in the J light curve were plotted with the initial epoch JD 2452000 (the presumed J-brightness maximum in Fig. 1). At minimum J brightness, the star became redder in $K-L$ and $L-M$. The $J-H$ color index decreased from $2^m.4$ to $2^m.3$, and this decrease may have occurred from the mid 2001 to the early 2002; before and after this period, the color index was almost constant.

DY Per. This object was classified by Alksnis *et al.* (1994) as an R CrB star. Alksnis *et al.* (2002) analyzed the long-term optical and infrared photometry for this star and confirmed that it is an R CrB

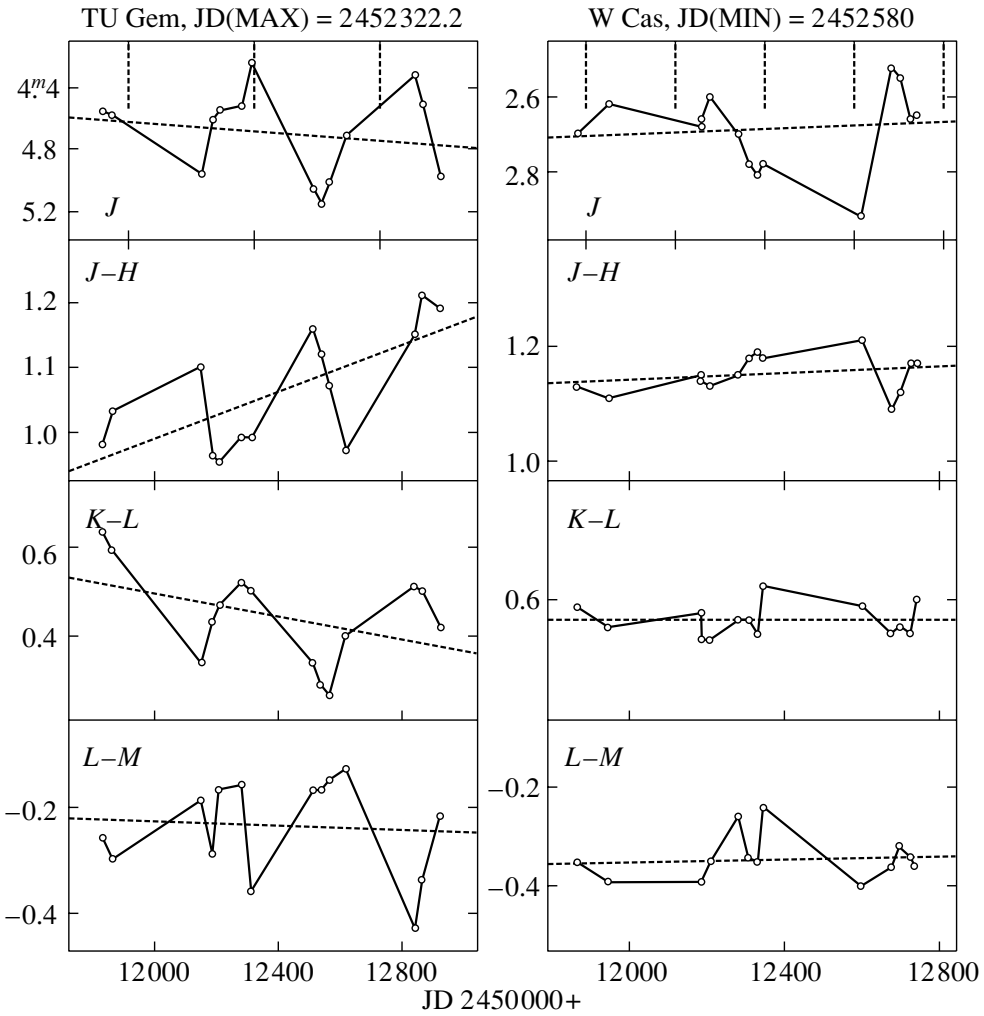

Fig. 1. (Cont.)

star. In August 2000, the object exhibited a decline in its infrared brightness together with its reddening at a variability phase of ~0.66 (Alksnis *et al.* 2002). If this effect is attributed to the formation of a circumstellar dust envelope (as in R CrB stars), then the observed color variation $J-H \sim 0^m.2$ corresponded to an optical depth of the dust envelope on the line of sight $\tau(J) \sim 0.4$ at $\lambda = 1.25$ μm (if the dust grains in the envelope are graphite ones). In February 2003, the dust envelope dispersed almost completely, and $\tau(J)$ did not exceed 0.06.

U Lyr. The observations spanned two periods, but they were performed at short intervals. At maximum J brightness, the star became hotter in $J-H$ and $K-L$. The variations of $L-M$ were in antiphase with those of $J-H$ and $K-L$ (as in ST And and V CrB). The magnitude and color variations exhibited a linear trend. The mean J brightness increased, and the object became hotter.

Y Tau and TU Tau. Their infrared photometry was performed over four and five periods, respectively. The observed J-magnitude variations for these stars were $\sim 0^m.2$; the color variations did not exceed the photometric errors. For Y Tau, the positions of the minima in the J light curve were plotted with the initial epoch JD 2452250 (the possible J-brightness minimum in Fig. 1). For TU Tau, the positions of the maxima were plotted with the initial epoch JD 2451926 (the possible J-brightness maximum in Fig. 1).

RW LMi. We have been performing the *JHKLM* photometry for this object since 1986. Step-by-step results of the analysis of our observations were presented in our previous papers (Taranova 1987; Taranova and Shenavrin 1999; Bogdanov and Taranova 1999). After 1994, a dense series of observations was obtained for the object; the circles in Fig. 2 indicate the J-magnitude and $J-H$, $K-L$, and $L-M$ color variations observed during the period 1994–

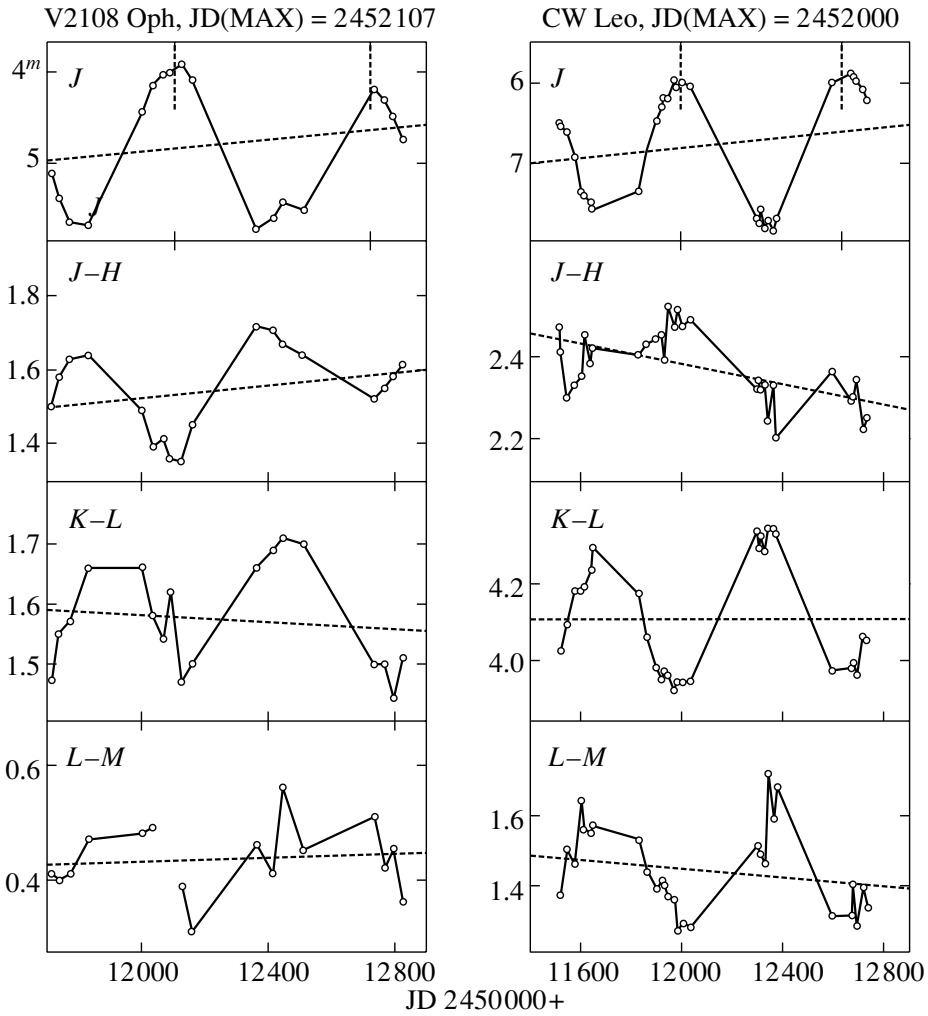

Fig. 1. (Cont.)

2003. The variability period of the infrared brightness of the star (605 days) marked by the vertical dashed lines as most reliable was determined from the 1996–2003 observations. The most probable period of the infrared brightness variations was estimated from our observations of RW LMi from 1986 until January 1999 (Taranova and Shenavrin 1999) to be 626 days. We see from Fig. 2 that from 1999 until the summer of 2003 (the end of our observations), periodic magnitude and color variations occurred against the background of a slow increase in the J brightness of RW LMi. Simultaneously, the color indices decreased; i.e., the object became hotter. For example, the observed decrease in the mean $K-L$ color index from $2\overset{m}{.}8$ (1999) to $2\overset{m}{.}4$ (2003) corresponds to an increase in the color temperature by about 120 K ($T_C(1999) \sim 750$ K, $T_C(2003) \sim 870$ K).

To see what the long-term infrared magnitude variations of the star are, Fig. 3a shows its JK light curves for the entire period of our observations (1986–2003), and Fig. 3b shows the same curves after the subtraction of the linear trend.

In Figs. 3a and 3b, at least three components can be distinguished in the observed magnitude and color variations:

(1) Infrared magnitude and color variations with a period of 605 ± 15 days. The observations after 1996 are in better agreement with the period of 605 days. The amplitude of the J-magnitude variations is $\sim 1\overset{m}{.}5$. At maximum J brightness, the star became hotter (see also Fig. 2).

(2) Long-term, possibly periodic, infrared magnitude and color variations. Their periods (the vertical lines in Fig. 3b) may be ~5200 days (~14.2 years). The amplitude of the J-magnitude variations is $\sim 1^m$. Here, just as in the infrared magnitude variations with a period of 605 days, the star becomes cooler at minimum brightness. Based on their red and infrared

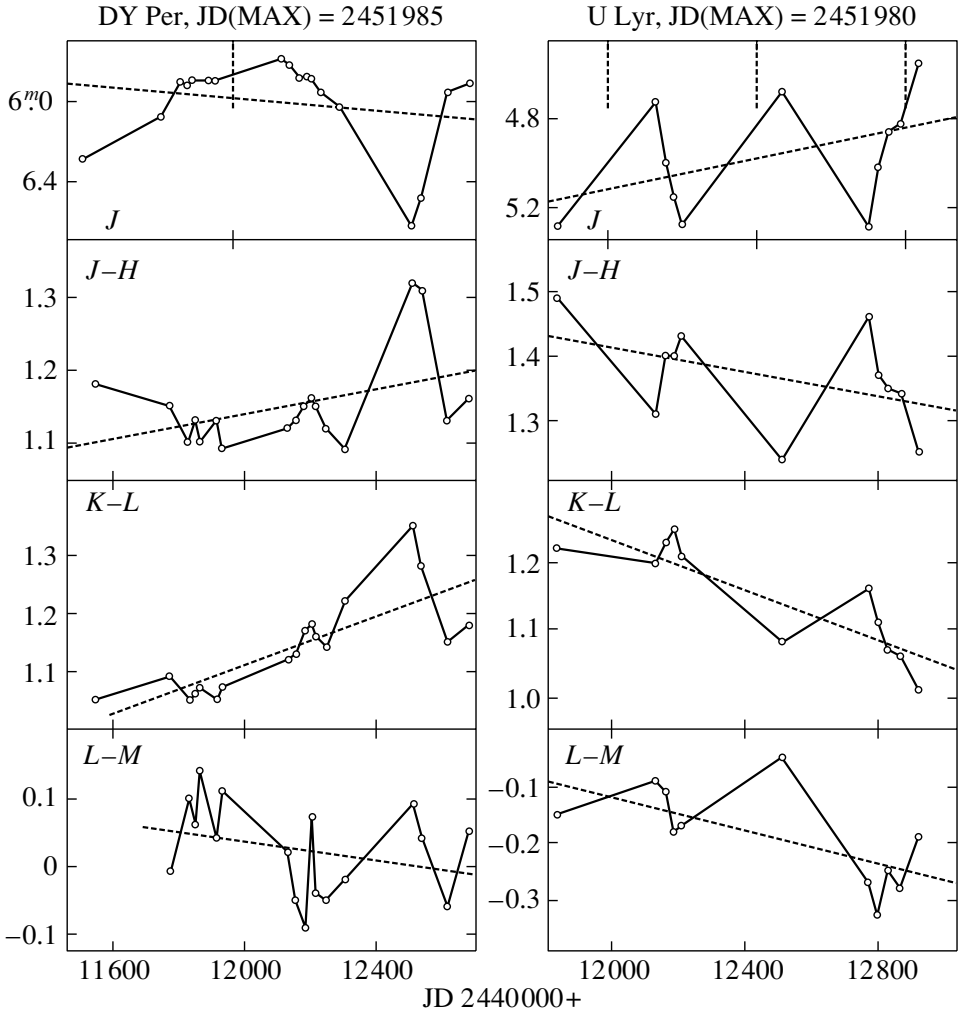

Fig. 1. (Cont.)

observations, Alksnis and Platais (1997) and Zacs *et al.* (2002) found a possible cycle in the magnitude variations of RW LMi with a characteristic time scale of more than 15 years.

(3) A linear trend. From 1986 until the summer of 2003 (the end of our observations), the J brightness gradually increased. The $JHKL$ brightnesses averaged over the seventeen years increased by $\sim -0^m.45$ (Fig. 3a), $-0^m.75$, $-0^m.60$ (Fig. 3a), and $-0^m.04$, respectively. At a wavelength of 5 μm, the brightness declined, and the linear trend was $0^m.1$ over the seventeen years. The maximum increase in brightness was observed at 1.65 μm (the H band). There is no synchronism in the color variations: the $J-H$ color index increased with infrared brightness, while $K-L$ decreased. The increase in $JHKL$ brightnesses and the decrease in M brightness together with the decrease in $K-L$ from 1986 until 2003 are indicative of a possible decrease in the optical depth of the dust envelope (its dispersal).

CIRCUMSTELLAR DUST ENVELOPES

The existence of relatively hot circumstellar dust envelopes around the carbon stars under study can be judged by their absorption at $\lambda < 2.2$ μm and by their emission at $\lambda > 2.2$ μm. For normal cool stars with relatively hot dust envelopes, the $J-H$, $K-L$, and $L-M$ color indices generally exceed 1^m, $0^m.40$, and $-0^m.2$, respectively. This criterion is valid for oxygen red stars (Johnson 1966; Koorneef 1983; Perrin *et al.* 1998). For carbon stars, the infrared color indices differ from their values for the so-called normal stars, because the spectra of the carbon stars in the wavelength range 1.25–5 μm exhibit spectral features attributable to carbon compounds in their atmospheres. For example, $K-L$ for carbon stars without noticeable infrared excesses can be much larger

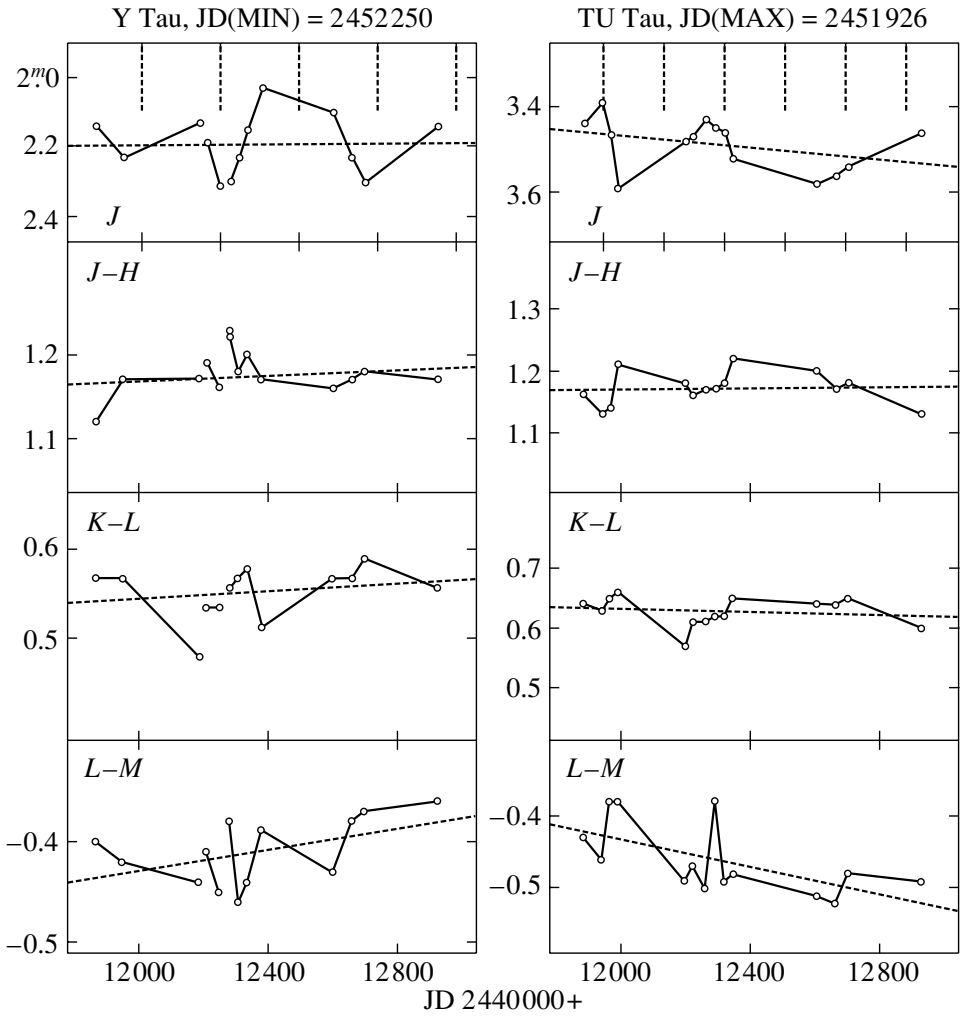

Fig. 1. (Cont.)

than $0^m.4$, while $L-M$ is smaller ($-0^m.2$). In the two-color infrared diagrams, the carbon stars occupy a special place (see, e.g., Kerschbaum and Hron 1994).

In this study, the $K-L$ and $L-M$ color indices served as a criterion for the existence of relatively hot dust envelopes around the observed carbon stars. If $K-L > 0^m.5$ and/or $L-M > -0^m.4$ for the observed object (Table 2), then an infrared excess was assumed to be possible in its LM radiation. As a result, based on the data of Table 2, we may assume that infrared excesses are observed in all carbon Mira stars. The Mira stars W Cas, X Cas, and BD Vul exhibit insignificant excesses. Infrared excesses were definitely observed in four of the fourteen semiregular (SR) variables. Small excesses may also be present in four more SR variables: TU Gem, RX Peg, TU Tau, and Y Tau. Two of the four irregular (L) variables clearly show infrared excesses. The $J-H$ color indices for the remaining carbon stars (except NQ Gem and NQ Cas) are larger than unity; i.e., cold dust envelopes are most likely to be also present around them, but we failed to detect their emission at 3.5 and 5 μm.

To estimate the basic parameters of the dust envelopes associated with the observed objects, we computed several simple models for the emission of a star + dust envelope system. The computations were performed for a spherically symmetric, physically thin dust envelope whose emission was in radiative equilibrium with the emission from the central star. Basic relations can be found in our previous paper (Taranova 2000). In our computations, the dust grains in the envelopes were assumed to be graphite ones, i.e., the absorption efficiency factor for a dust grain $Q(\lambda) \infty \lambda^{-\beta}$, $\beta = 2$.

If the parameters of the central source (its radius and temperature) are assumed to be constant, then the observed magnitude (and color) variations depend

Table 2. Mean magnitudes and color indices for twenty-seven carbon stars and two oxygen Mira stars

Parameter	Mean	sd	se	Parameter	Mean	sd	se	Parameter	Mean	sd	se
ST And, $N = 16$				**UV Aur, $N = 53$**				**X Cas, $N = 2$**			
J	5.286	0.267	0.067	J	4.469	0.284	0.039	J	5.030	0.170	0.120
H	4.158	0.184	0.046	H	3.297	0.248	0.034	H	3.610	0.156	0.110
K	3.497	0.092	0.023	K	2.359	0.190	0.026	K	2.610	0.071	0.050
L	2.939	0.060	0.015	L	1.516	0.219	0.030	L	1.690	0.014	0.010
M	3.538	0.163	0.041	M	1.269	0.192	0.027	M	2.185	0.120	0.085
$J-H$	1.128	0.091	0.023	$J-H$	1.172	0.105	0.014	$J-H$	1.420	0.014	0.010
$J-K$	1.789	0.188	0.047	$J-K$	2.110	0.196	0.027	$J-K$	2.420	0.099	0.070
$K-L$	0.558	0.071	0.018	$K-L$	0.843	0.100	0.014	$K-L$	0.920	0.057	0.040
$L-M$	−0.599	0.143	0.036	$L-M$	0.246	0.104	0.014	$L-M$	−0.495	0.106	0.075
$H-K$	0.661	0.101	0.025	$H-K$	0.938	0.107	0.015	$H-K$	1.000	0.085	0.060
VX And, $N = 3$				**UU Aur, $N = 16$**				**V CrB, $N = 48$**			
J	3.027	0.142	0.082	J	1.158	0.109	0.027	J	3.479	0.460	0.066
H	1.780	0.115	0.067	H	0.054	0.098	0.025	H	2.247	0.382	0.055
K	0.960	0.078	0.045	K	−0.558	0.077	0.019	K	1.377	0.276	0.040
L	0.230	0.020	0.012	L	−1.111	0.081	0.020	L	0.218	0.247	0.036
M	1.193	0.025	0.015	M	−0.639	0.081	0.020	M^*	0.120	0.242	0.035
$J-H$	1.247	0.032	0.019	$J-H$	1.104	0.030	0.008	$J-H$	1.232	0.104	0.015
$J-K$	2.067	0.071	0.041	$J-K$	1.716	0.052	0.013	$J-K$	2.102	0.207	0.030
$K-L$	0.730	0.061	0.035	$K-L$	0.553	0.018	0.005	$K-L$	1.159	0.063	0.009
$L-M$	−0.963	0.006	0.003	$L-M$	−0.472	0.052	0.013	$L-M^*$	0.104	0.081	0.012
$H-K$	0.820	0.040	0.023	$H-K$	0.612	0.029	0.007	$H-K$	0.870	0.115	0.017
S Aur, $N = 13$				**W Cas, $N = 14$**				**U Cyg, $N = 7$**			
J	4.956	0.111	0.031	J	4.696	0.284	0.076	J	3.391	0.596	0.211
H	3.414	0.087	0.024	H	3.634	0.262	0.070	H	2.134	0.537	0.190
K	2.178	0.062	0.017	K	2.938	0.175	0.047	K	1.274	0.361	0.128
L	0.648	0.066	0.018	L	2.494	0.238	0.064	L	0.326	0.356	0.126
M	0.428	0.126	0.035	M	2.733	0.162	0.043	M^*	0.467	0.254	0.096
$J-H$	1.542	0.038	0.011	$J-H$	1.062	0.092	0.025	$J-H$	1.258	0.121	0.043
$J-K$	2.778	0.063	0.018	$J-K$	1.758	0.217	0.058	$J-K$	2.118	0.287	0.101
$K-L$	1.530	0.020	0.005	$K-L$	0.444	0.108	0.029	$K-L$	0.948	0.109	0.039
$L-M$	0.220	0.090	0.025	$L-M$	−0.239	0.092	0.025	$L-M^*$	−0.106	0.122	0.046
$H-K$	1.236	0.033	0.009	$H-K$	0.696	0.149	0.040	$H-K$	0.860	0.194	0.068

Table 2. (Cont.)

Parameter	Mean	sd	se	Parameter	Mean	sd	se	Parameter	Mean	sd	se
V1426 Cyg, $N = 4$				**CW Leo, $N = 31$**				**U Lyr, $N = 11$**			
J	3.320	0.397	0.198	J	6.760	0.712	0.128	J	4.967	0.259	0.078
H	1.855	0.406	0.203	H	4.388	0.743	0.134	H	3.600	0.184	0.055
K	0.720	0.308	0.154	K	1.387	0.744	0.134	K	2.661	0.095	0.029
L	−0.625	0.324	0.162	L	−2.718	0.599	0.108	L	1.515	0.089	0.027
M	−0.885	0.271	0.136	M	−4.161	0.496	0.089	M	1.704	0.161	0.049
$J-H$	1.465	0.061	0.031	$J-H$	2.372	0.086	0.016	$J-H$	1.367	0.080	0.024
$J-K$	2.600	0.100	0.050	$J-K$	5.373	0.071	0.013	$J-K$	2.306	0.171	0.052
$K-L$	1.345	0.017	0.009	$K-L$	4.105	0.151	0.027	$K-L$	1.145	0.082	0.025
$L-M$	0.260	0.088	0.044	$L-M$	1.443	0.121	0.022	$L-M$	−0.188	0.087	0.026
$H-K$	1.135	0.100	0.050	$H-K$	3.001	0.036	0.007	$H-K$	0.939	0.095	0.029
NQ Gem, $N = 36$				**RW LMi, $N = 65$**				**RX Peg, $N = 6$**			
J	4.457	0.049	0.008	J	6.058	0.695	0.086	J	4.068	0.145	0.059
H	3.568	0.045	0.007	H	3.703	0.669	0.083	H	2.905	0.125	0.051
K	3.214	0.040	0.007	K	1.541	0.583	0.072	K	2.290	0.083	0.034
L	2.877	0.037	0.006	L	−1.173	0.473	0.059	L	1.652	0.074	0.030
M	3.299	0.054	0.009	M	−2.057	0.401	0.050	M	2.192	0.108	0.044
$J-H$	0.889	0.032	0.005	$J-H$	2.356	0.068	0.008	$J-H$	1.163	0.029	0.012
$J-K$	1.242	0.035	0.006	$J-K$	4.517	0.153	0.019	$J-K$	1.778	0.064	0.026
$K-L$	0.338	0.025	0.004	$K-L$	2.714	0.193	0.024	$K-L$	0.638	0.012	0.005
$L-M$	−0.422	0.041	0.007	$L-M$	0.884	0.177	0.022	$L-M$	−0.540	0.036	0.015
$H-K$	0.354	0.021	0.003	$H-K$	2.162	0.111	0.014	$H-K$	0.615	0.044	0.018
TU Gem, $N = 14$				**T Lyn, $N = 23$**				**DY Per, $N = 18$**			
J	2.688	0.107	0.029	J	5.316	0.387	0.081	J	6.007	0.227	0.054
H	1.536	0.078	0.021	H	4.096	0.371	0.077	H	4.856	0.174	0.041
K	0.923	0.049	0.013	K	3.141	0.234	0.049	K	4.096	0.130	0.031
L	0.354	0.042	0.011	L	2.296	0.229	0.048	L	2.956	0.126	0.030
M	0.699	0.068	0.018	M	2.260	0.178	0.037	M^*	2.915	0.086	0.021
$J-H$	1.151	0.034	0.009	$J-H$	1.220	0.057	0.012	$J-H$	1.151	0.065	0.015
$J-K$	1.765	0.062	0.017	$J-K$	2.175	0.161	0.034	$J-K$	1.911	0.114	0.027
$K-L$	0.569	0.024	0.006	$K-L$	0.845	0.029	0.006	$K-L$	1.140	0.083	0.020
$L-M$	−0.346	0.047	0.013	$L-M$	0.036	0.100	0.021	$L-M^*$	0.024	0.068	0.016
$H-K$	0.614	0.033	0.009	$H-K$	0.955	0.143	0.030	$H-K$	0.759	0.057	0.013

Table 2. (Cont.)

Parameter	Mean	sd	se	Parameter	Mean	sd	se	Parameter	Mean	sd	se
SY Per, $N = 5$				**BD Vul, $N = 7$**				**NQ Cas, $N = 2$**			
J	4.186	0.259	0.116	J	5.001	0.123	0.046	J	5.45	0.07	0.05
H	2.846	0.182	0.082	H	3.836	0.077	0.029	H	4.59	0.04	0.03
K	1.970	0.079	0.036	K	3.069	0.064	0.024	K	4.12	0.04	0.03
L	1.176	0.061	0.027	L	2.216	0.072	0.027	L	3.51	0.03	0.02
M	1.800	0.105	0.047	M	2.569	0.094	0.036	M	3.90	0.05	0.04
$J-H$	1.340	0.081	0.036	$J-H$	1.166	0.073	0.028	$J-H$	0.87	0.04	0.03
$J-K$	2.216	0.187	0.084	$J-K$	1.933	0.116	0.044	$J-K$	1.33	0.03	0.02
$K-L$	0.794	0.073	0.033	$K-L$	0.853	0.050	0.019	$K-L$	0.61	0.01	0.01
$L-M$	−0.624	0.117	0.053	$L-M$	−0.353	0.134	0.051	$L-M$	−0.39	0.02	0.02
$H-K$	0.876	0.107	0.048	$H-K$	0.767	0.052	0.020	$H-K$	0.47	0.03	0.03
X Sge, $N = 7$				**SU And, $N = 4$**				**EH And, $N = 7$**			
J	3.799	0.056	0.021	J	4.05	0.04	0.02	J	4.01	0.05	0.02
H	2.627	0.037	0.014	H	2.97	0.04	0.02	H	3.08	0.04	0.01
K^*	1.982	0.026	0.010	K	2.46	0.05	0.02	K	2.74	0.04	0.02
L^*	1.303	0.025	0.010	L	1.98	0.02	0.01	L	2.40	0.05	0.02
M	1.864	0.039	0.015	M	2.50	0.02	0.01	M	2.61	0.05	0.02
$J-H$	1.171	0.034	0.013	$J-H$	1.08	0.01	0.01	$J-H$	0.93	0.02	0.01
$J-K^*$	1.825	0.041	0.017	$J-K$	1.59	0.01	0.00	$J-K$	1.27	0.03	0.01
$K-L^*$	0.678	0.024	0.010	$K-L$	0.48	0.04	0.02	$K-L$	0.34	0.01	0.01
$L-M^*$	−0.562	0.041	0.017	$L-M$	−0.51	0.04	0.02	$L-M$	−0.22	0.03	0.01
$H-K^*$	0.643	0.033	0.013	$H-K$	0.51	0.02	0.01	$H-K$	0.35	0.02	0.01
TU Tau, $N = 14$				**UY And, $N = 4$**				**V2108 Opt, $N = 18$**			
J	3.489	0.060	0.016	J	6.04	0.12	0.06	J	4.81	0.69	0.16
H	2.317	0.045	0.012	H	5.01	0.08	0.04	H	3.27	0.59	0.14
K	1.669	0.042	0.011	K	4.51	0.05	0.02	K	2.11	0.52	0.12
L	1.041	0.032	0.008	L	4.02	0.03	0.01	L	0.54	0.48	0.11
M	1.502	0.063	0.017	M	4.41	0.03	0.02	M^*	0.15	0.45	0.11
$J-H$	1.171	0.027	0.007	$J-H$	1.03	0.06	0.03	$J-H$	1.54	0.12	0.03
$J-K$	1.820	0.032	0.008	$J-K$	1.53	0.09	0.04	$J-K$	2.70	0.19	0.04
$K-L$	0.628	0.025	0.007	$K-L$	0.49	0.03	0.01	$K-L$	1.57	0.09	0.02
$L-M$	−0.461	0.049	0.013	$L-M$	−0.39	0.05	0.03	$L-M^*$	0.42	0.10	0.02
$H-K$	0.649	0.020	0.005	$H-K$	0.50	0.07	0.03	$H-K$	1.16	0.14	0.03
Y Tau, $N = 13$				**TX Aur, $N = 7$**							
J	2.191	0.085	0.024	J	4.07	0.12	0.05				
H	1.017	0.081	0.022	H	2.87	0.10	0.04				
K	0.363	0.049	0.014	K^*	2.26	0.09	0.04				
L	−0.233	0.040	0.011	L	1.62	0.05	0.02				
M	0.177	0.055	0.015	M	2.16	0.10	0.04				
$J-H$	1.174	0.023	0.006	$J-H$	1.20	0.03	0.01				
$J-K$	1.828	0.043	0.012	$J-K^*$	1.83	0.04	0.02				
$K-L$	0.596	0.027	0.008	$K-L^*$	0.64	0.04	0.01				
$L-M$	−0.410	0.033	0.009	$L-M$	−0.55	0.05	0.02				
$H-K$	0.654	0.040	0.011	$H-K^*$	0.61	0.03	0.01				

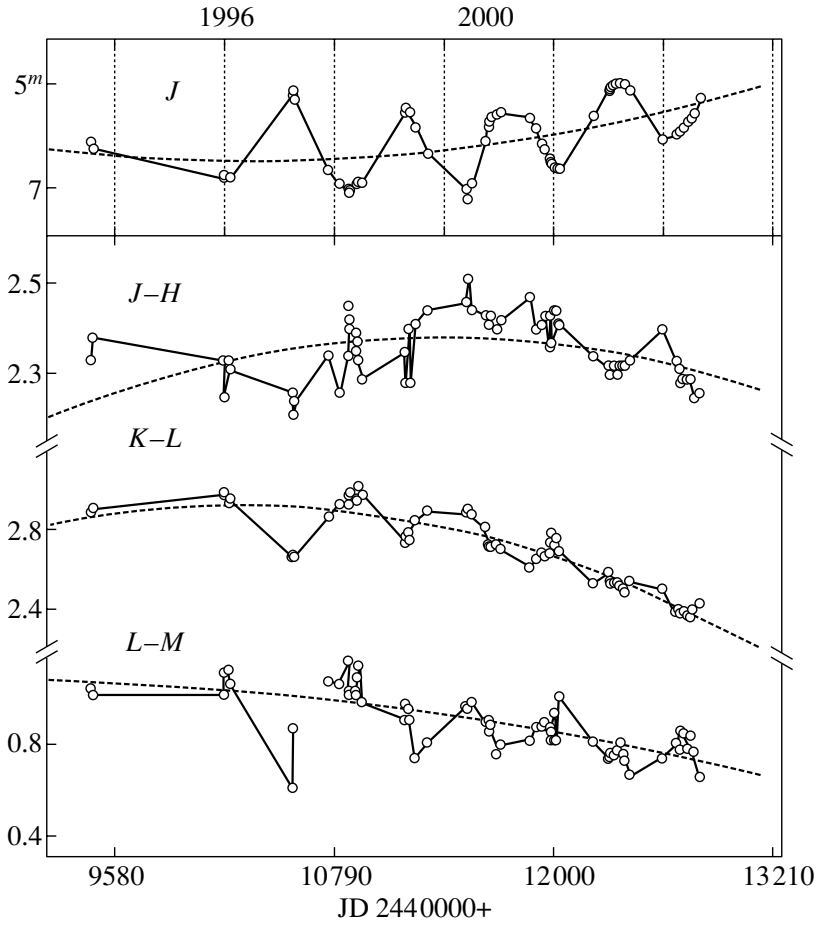

Fig. 2. J-magnitude and $J-H$, $K-L$, and $L-M$ color variations of RW LMi during 1994–2003. The vertical lines in the upper panel indicate the 605 day intervals. The dashed lines represent the second-order curves.

only on the type of dust grains (in our case, the grains are graphite ones), their temperature, and the optical depth of the dust envelope.

For graphite grains, the following relations were used to estimate the attenuation of the emission from the central source by the dust envelope: $A_J/A_H/A_K/A_L/A_M = 1.0/0.57/0.32/0.13/0.06$.

For several sets of parameters (T_*, T_d, [from $\tau_1(1.25\ \mu\mathrm{m})$ to $\tau_2(1.25\ \mu\mathrm{m})$], β), we obtained model spectral energy distributions for a source surrounded by a dust envelope with a variable optical depth. The temperature of the central star was varied over the range $T_* = 2500$–3500 K, and the dust temperature was within $T_\mathrm{d} = 500$–1000 K. The range of optical depths at $\lambda = 1.25\ \mu\mathrm{m}$ (J band) was $\tau(1.25\ \mu\mathrm{m}) = 0$ (0.4)4.

Figure 4 shows two-color ($J-H$, $K-L$) and ($J-H$, $L-M$) diagrams for the mean color indices from Table 2 (filled circles). The names of some of the objects are given above these circles. The model curves *1*–*3* correspond to the following sets of parameters:

curve *1*—$T_* = 2800$ K, $T_\mathrm{d} = 550$, $\tau(1.25\ \mu\mathrm{m}) = 0$ (0.4) 4;

curve *2*—$T_* = 2800$ K, $T_\mathrm{d} = 600$, $\tau(1.25\ \mu\mathrm{m}) = 0$ (0.4) 4;

curve *3*—$T_* = 2800$ K, $T_\mathrm{d} = 600$, $\tau(1.25\ \mu\mathrm{m}) = 0$ (0.4) 1.2.

The computed curves shown in Fig. 4 were obtained for an effective temperature of the central star of 2800 K. For curve *1*, the color indices were assumed to be equal to their values for a blackbody with $T = 2800$ K, i.e., $(J-H)_0 = 0^m.66$, $(K-L)_0 = 0^m.44$, $(L-M)_0 = 0^m.26$; for curve *2*, $(J-H)_0 = 1^m.0$, $(K-L)_0 = 0^m.44$, $(L-M)_0 = 0^m$; and for curve *3*, the unreddened colors were $(J-H)_0 = 1^m.2$, $(K-L)_0 = 0^m.4$, $(L-M)_0 = -0^m.9$. The initial color indices for curves *2* and *3* correspond to the extreme values on the straight line NC. The observed deviations of the initial color indices (line NC) from their values for

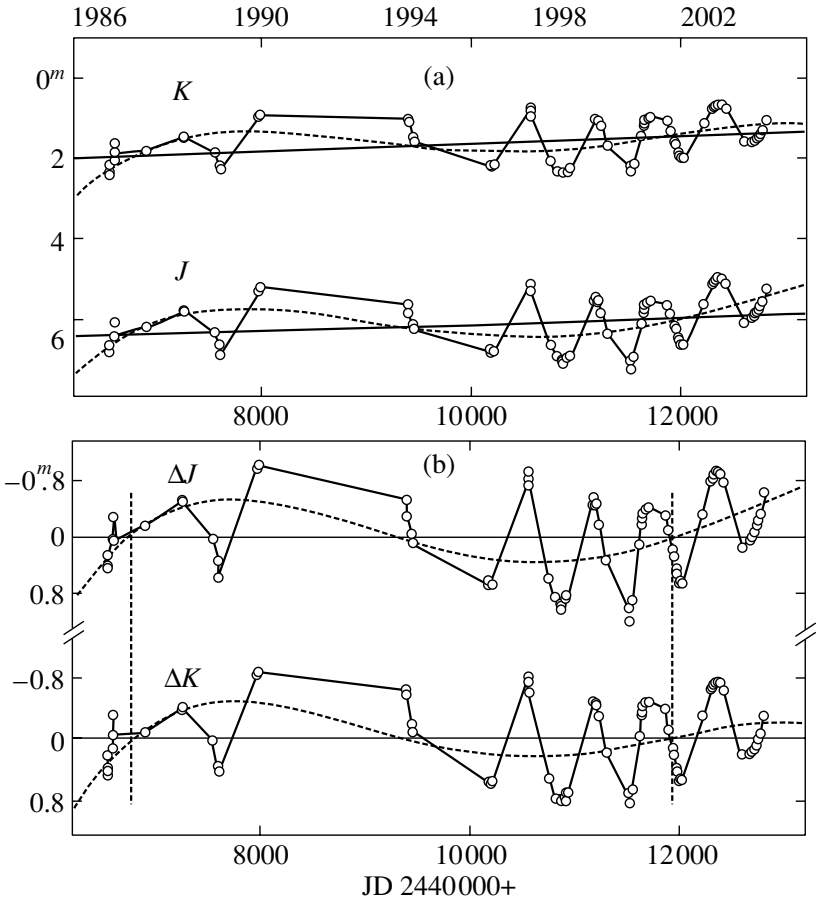

Fig. 3. (a) J- and K-magnitude variations of RW LMi during the period 1986–2003: the solid straight lines are the regression lines (linear trend); the dashed lines represent the fourth-order curves. (b) The residual J- and K-magnitude variations of RW LMi during the period 1994–2003 after the subtraction of the linear trend; the dashed lines represent the fourth-order curves.

a blackbody at the same stellar temperature can be attributed to the existence of molecular absorption bands in the infrared, particularly in the M (5 μm) and L (3.5 μm) bands.

Judging by their mean $J-H$ and $K-L$ color indices (see Fig. 4a), a significant fraction of the objects lie between the model curves *2* and *3*. The pattern in Fig. 4b is similar: the mean color indices for all of the objects (except RW LMi and CW Leo) lie within the regions bounded by curves *2* and *3* for optical depths of the dust envelopes within the range 0–1.2. Only the carbon stars NQ Gem and NQ Cas and the oxygen Mira star EH And remained near the line of normal stars.

The largest excesses were observed in the infrared sources CW Leo and RW Lmi; for CW Leo, we failed to represent the observed mean color indices by our simple model. The oxygen Mira star V2108 Oph, the carbon Mira stars V1426 Cyg, S Aur, and UV Aur, etc. follow next in order of decreasing excesses.

By comparing the observed and computed mean color indices for each object, we estimated the mean optical depths of their dust envelopes at a wavelength of 1.25 μm, which are given in column 3 of Table 3. Column 4 gives the mean J magnitudes corrected for the absorption by the dust envelope, i.e., $J_0 = J_{\text{mean}} - 1.086\tau J$. We took J_{mean} from Table 2.

Columns 6 and 7 of Table 3 list, respectively, the temperatures of the objects and their standard deviations that were determined using the mean $J-K$ color indices from Table 2 and relations from the paper by Bergeat *et al.* (2001). The $J-K$ color indices were first corrected for the absorption in the circumstellar envelopes; their values of $(J-K)_0$ are given in column 5 of Table 3. Column 8 of Table 3 gives the temperatures of the objects from the paper by Bergeat *et al.* (2001).

Columns 9 and 10 list, respectively, the angular diameters of the objects and their standard deviations

Table 3. Mean parameters for the observed carbon stars and two oxygen Mira stars and their dust envelopes

No.	Object	$\tau(J)$	J_0	$(J-K)_0$	T, K	sd(T)	T, K	Θ, 10^{-3} arcsec (relation (1))	sd(Θ)	Θ, 10^{-3} arcsec (data by Bergeat *et al.* (2001))
1	ST And	0	5.286	1.79	2575	197		1.78	0.18	
2	VX And	0	3.027	2.07	2316	41		6.44	0.27	
3	S Aur	1.1	3.768	1.97	2385	63	1845 ± 70	4.25	0.15	8.9 ± 0.6
4	UV Aur	0.35	4.091	1.85	2506	200		3.28	0.34	
5	UU Aur	0	1.158	1.72	2656	58	2790 ± 40	11.1	0.50	12.1 ± 0.2
6	W Cas	0.05	4.642	1.72	2650	233		2.24	0.26	
7	X Cas	0.5	4.49	2.05	2324	57		3.25	0.17	
8	V CrB	0.4	3.047	1.81	2554	214	2020 ± 40	5.16	0.88	7.26 ± 0.23
9	U Cyg	0.4	2.959	1.82	2537	290	2410 ± 90	5.54	1.20	6.96 ± 0.5
10	V1426 Cyg	0.9	2.348	1.94	2417	100	1970 ± 45	8.05	1.05	10.8 ± 0.4
11	NQ Gem	0	4.457	1.24	3247	48		1.61	0.05	
12	TU Gem	0.12	2.558	1.68	2701	70		5.59	0.26	
13	CW Leo	~ 3	3.52	3.17	1756	31		12.0	1.11	
14	RW LMi	3.1	2.723	2.24	2217	84		8.70	1.56	
15	T Lyn	0.4	4.888	1.88	2477	163		2.35	0.32	
16	U Lyr	0.5	4.427	1.94	2417	169	2504 ± 55	3.06	0.26	3.58 ± 0.09
17	RX Peg	0.1	3.96	1.70	2669	71		3.00	0.18	
18	DY Per	0.32	5.661	1.68	2702	127		1.34	0.13	
19	SY Per	0.3	3.862	2.00	2359	180	2890 ± 340	4.21	0.34	3.4 ± 0.8
20	X Sge	0.05	3.745	1.79	2576	44		3.58	0.08	
21	TU Tau	0.1	3.381	1.75	2622	35	2911 ± 50	4.08	0.10	3.82 ± 0.08
22	Y Tau	0.1	2.083	1.75	2613	47	2690 ± 90	7.48	0.25	8.18 ± 0.5
23	BD Vul	0.15	4.839	1.82	2539	122		2.24	0.10	
24	SU And	0	4.047	2.20	2240	299		4.37	0.05	
25	UY And	0	6.037	2.11	2291	110		1.65	0.06	
26	TX Aur	0.1	3.958	2.13	2281	305		4.35	0.15	
27	NQ Cas	0	5.45	2.20	2240	299		2.29	0.04	
28	EH And	0	4.009	1.27	3205	42		2.03	0.06	
29	V2108 Oph	1.15	3.567	1.36	3095	665		2.79	1.05	

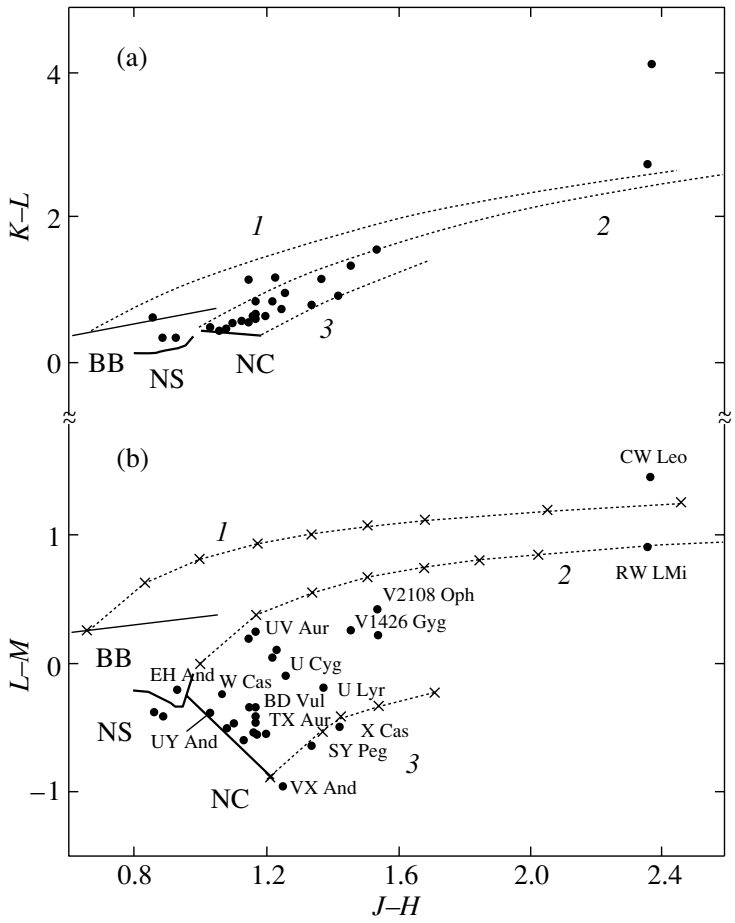

Fig. 4. Two-color ($J-H$, $K-L$) (a) and ($J-H$, $L-M$) (b) diagrams. The circles indicate the mean color indices for the program stars. Lines NS represent the color indices for late-type red giants (Koorneef 1983; Perrin *et al.* 1998). Lines BB represent the variations in the corresponding color indices of a blackbody as its temperature varies between 3000 and 2000 K. Lines NC represent the color variations of carbon stars with normal colors (without any noticeable infrared excesses). The dotted lines *1–3* represent the model curves; the color variations along these curves reflect the variations in the optical depths of the corresponding dust envelopes. The crosses in curves *1–3* are plotted at equally spaced optical depths of the dust envelope at $\lambda = 1.25$ μm, $\Delta\tau(1.25) = 0.4$.

calculated from the relation

$$\Theta = 2[F(J_0)/\pi B(J, T_*)]^{0.5} =$$
$$1.08 \times 10^{-3}(e^{11512/T_*} - 1)^{0.5} \times 10^{-0.2J_0} \text{ arcsec},$$

where $F(J_0)$ is the J-band flux from the object, and $\pi B(J, T_*)$ is the radiation flux from a blackbody at a wavelength of 1.25 μm at temperature T_*. We used the temperatures from column 6 of Table 3. The last column gives the angular diameters of the objects from the paper by Bergeat *et al.* (2001).

As follows from the data of Table 3, our estimates of the temperatures and angular diameters for the program stars are in good agreement with those from the paper by Bergeat *et al.* (2001) for objects with optically thin dust envelopes. Note that, we estimated the diameters from the fluxes in the J band, in which the contribution of the emission from dust envelopes with temperatures of 500–800 K does not exceed a few fractions of a percent. Bergeat *et al.* (2001) used wavelengths of 1.65 and 2.2 μm at which this contribution is already noticeable.

CONCLUSIONS

Our infrared photometry for twenty-seven carbon stars and two oxygen Mira stars have revealed the following:

In general, the J-magnitude variations of the periodic carbon stars for which relatively long series of observations were obtained agree with their periods given in the GCVS (Kholopov *et al.* 1985–1990). A periodicity of ~600–640 days was clearly seen in the J-magnitude variations of the oxygen Mira star V2108 Oph.

For all of the observed stars, the $J-H$ color index generally increased at minimum J brightness.

For seven carbon stars, the J-magnitude variations exhibited a linear trend.

The J-magnitude variations of the infrared object CW Leo and the semiregular variable RW LMi had the largest amplitude among the carbon Mira stars.

The amplitude of the J-magnitude variations for the oxygen Mira star V2108 Oph was about $1\overset{m}{.}7$. The stars is embedded in a dense dust envelope and $A'_V \sim 4^m$ (or $\tau(1.25\ \mu\text{m}) \sim 0.9$). The color temperature of the star was ~1100 and ~1200 K at minimum and maximum brightness, respectively.

The observed J-magnitude variations of the infrared object CW Leo were $\sim 1\overset{m}{.}7$ and had a period close to 630 days. At minimum J brightness, the star became redder in $K-L$ and $L-M$. Its $J-H$ color index decreased from $2\overset{m}{.}4$ to $2\overset{m}{.}3$, and this decrease may have occurred in the period from the mid 2001 until the early 2002; before and after this period, the color index was almost constant.

It follows from the 1999–2003 observations of RW LMi that its periodic infrared magnitude and color variations took place against the background of a slow increase in the J brightness of RW LMi. Simultaneously, the color indices decreased; i.e., the object became hotter. The following three components can be distinguished in the observed magnitude and color variations of RW LMi:

(1) Infrared magnitude and color variations with a period of 600–630 days. The observations after 1996 are in better agreement with the period of 605 days. At maximum J brightness, the star became hotter.

(2) Long-term, possibly periodic, infrared magnitude and color variations. The period of these variations may be ~5200 days (~14.2 years). The amplitude of the J-magnitude variations is $\sim 1^m$.

(3) A linear trend. From 1986 until the summer of 2003, the J brightness gradually increased. The mean *JHKL* brightnesses increased over the seventeen years by $\sim -0\overset{m}{.}45$, $-0\overset{m}{.}75$, $-0\overset{m}{.}60$, and $-0\overset{m}{.}04$, respectively. At a wavelength of 5 μm, the brightness declined, and the linear trend was $0\overset{m}{.}1$ over the seventeen years. The maximum rise in brightness was observed at 1.65 μm. The increase in *JHKL* brightnesses and the decrease in M brightness together with the decrease in $K-L$ color index from 1986 until 2003 are indicative of a possible decrease in the optical depth of the circumstellar dust envelope (its dispersal).

All of the carbon Mira stars exhibit infrared excesses. The excesses in the Mira stars W Cas, X Cas, and BD Vul are insignificant. Infrared excesses were observed in four of the fourteen semiregular (SR) variables. Small excesses may be present in four more SR variables: TU Gem, RX Peg, TU Tau, and Y Tau. Infrared excesses are clearly seen in two of the four irregular (L) variables.

In the simple "star + dust envelope" model, the optical depths of the circumstellar dust envelopes at a wavelength of 1.25 μm lie within the range 0–1.2 for a significant fraction of the observed stars. No hot dust envelopes were found around the carbon stars NQ Gem and NQ Cas and the oxygen Mira star EH And. For the infrared source CW Leo, we failed to represent the observed mean color indices by the simple model.

For each object, we estimated the mean optical depths of their dust envelopes at a wavelength of 1.25 μm, the angular diameters of the objects, and their temperatures.

ACKNOWLEDGMENTS

We are grateful to the referees for several helpful remarks. This study was supported in part by the Ministry of Industry, Technology, and Science (The Astronomy program) and the Russian Foundation for Basic Research (project no. 03-02-17123).

REFERENCES

1. A. Alksnis, Baltic Astron. **3**, 410 (1994).
2. A. Alksnis and I. Platais, Baltic. Astron. **6**, 471 (1997).
3. A. Alksnis, V. M. Larionov, L. V. Larionova, and V. I. Shenavrin, Baltic. Astron. **11**, 487 (2002).
4. J. Bergeat, A. Knapik, and B. Rutily, Astron. Astrophys. **369**, 178 (2001).
5. M. A. T. Groenewegen, Astron. Astrophys. **317**, 503 (1997).
6. H. L. Johnson, Annu. Rev. Astron. Astrophys. **4**, 193 (1966).
7. H. L. Johnson, R. I. Mitchel, B. Iriarte, and W. Z. Wisniewski, Comm. Lunar Planet. Lab. **4**, 99 (1966).
8. F. Kerschbaum and J. Hron, Astron. Astrophys., Suppl. Ser. **106**, 397 (1994).
9. P. N. Kholopov, N. N. Samus', V. P. Goranskiĭ, *et al., General Catalogue of Variable Stars* (Nauka, Moscow, 1985–1990) [in Russian].
10. J. Koorneef, Astron. Astrophys., Suppl. Ser. **51**, 489 (1983).
11. A. É. Nadzhip, V. I. Shenavrin, and V. G. Tikhonov, Tr. Gos. Astron. Inst. Sternberg **58**, 119 (1986).
12. G. Perrin, V. Coude du Foresto, S. T. Ridgway, *et al.*, Astron. Astrophys. **331**, 619 (1998).
13. O. G. Taranova, Astrofizika **27**, 29 (1987).
14. O. G. Taranova, Pis'ma Astron. Zh. **26**, 472 (2000) [Astron. Lett. **26**, 404 (2000)].
15. O. G. Taranova and V. I. Shenavrin, Pis'ma Astron. Zh. **25**, 860 (1999) [Astron. Lett. **25**, 750 (1999)].
16. L. Zacs, R. Spelmanis, A. Alksnis, and F. Musaev, *IAU Symp. No. 210: Modelling of Stellar Atmosphere* (Uppsala, Sweden, 2002) (in press).

Translated by V. Astakhov

Astronomy Letters, Vol. 30, No. 8, 2004, pp. 566–576. Translated from Pis'ma v Astronomicheskiĭ Zhurnal, Vol. 30, No. 8, 2004, pp. 623–634.

Influence of Uncertainties in the Rate Constants of Chemical Reactions on Astrochemical Modeling Results

A. I. Vasyunin[1*], A. M. Sobolev[1], D. S. Wiebe[2***], and D. A. Semenov[3****]**

[1] *Ural State University, ul. Lenina 51, Yekaterinburg, 620083 Russia*

[2] *Institute of Astronomy, Russian Academy of Sciences, ul. Pyatnitskaya 48, Moscow, 119017 Russia*

[3] *Max Planck Institute of Astronomy, Heidelberg, Germany*

Received September 19, 2003

Abstract—We analyze the influence of errors in the rate constants of gas-phase chemical reactions on the model abundances of molecules in the interstellar medium using the UMIST 95 chemical database. By randomly varying the rate constants within the limits of the errors given in UMIST 95, we have estimated the scatters in theoretical abundances for dark and diffuse molecular clouds. All of the species were divided into six groups by the scatter in their model equilibrium abundances when varying the rate constants of chemical reactions. The distribution of the species in groups depends on the physical conditions. The scatters in the abundances of simple species lie within 0.5–1 order of magnitude, but increase significantly as the number of atoms in the molecule increases. We suggest a simple method for identifying the reactions whose rate constants have the strongest effect on the abundance of a selected species. This method is based on an analysis of the correlations between the abundance of species and the reaction rate constants and allows the extent to which an improvement in the rate constant of a specific reaction reduces the uncertainty in the abundance of the species concerned to be directly estimated.

Key words: *astrochemistry, stars: formation, molecular processes, interstellar medium, chemical composition.*

INTRODUCTION

Studies of the chemical processes in the interstellar medium (ISM) are of great interest and have been carried out for more than forty years. More than 120 various species have been found to date in molecular clouds, among which are both inorganic molecules and simple organic compounds. Astrochemistry, the science concerned with the chemical processes in the interstellar medium and their influence on its evolution and physical properties, has emerged. Progress in observational astrochemistry poses new problems to theorists and requires constructing more complex and better models for the chemical evolution of the ISM that could explain observed facts and link the chemistry and physics of the objects being studied.

One of the most important problems in modeling the interstellar chemistry is to reproduce the observed abundances of chemical species and to reveal their dependence on the physical and evolutionary parameters of the ISM. This modeling is based on the solution of the chemical network equations. At present, a number of models have been developed for the chemical and chemical–dynamical evolution of molecular clouds (see the review by van Dishoeck and Blake 1998) in which reasonable agreement was achieved between theoretical and observational data. At the same time, it is too early to say that the chemical evolution models are completely adequate.

Significant errors in the rate constants of chemical reactions are among the most important difficulties on this road. According to Millar *et al.* (1997), the uncertainties in the rate constants of many gas-phase reactions exceed an order of magnitude. Clearly, such significant uncertainties affect the modeling results for the interstellar chemistry and, hence, our understanding of the physical processes in the ISM as a whole. However, there are virtually no published estimates of this influence as yet.

In this paper, we statistically analyze the influence of errors in the reaction rate constants in the UMIST 95 database on the abundances calculated in time-independent gas-phase chemical models. In the next section, we briefly describe the aspects of

[*] E-mail: vasyunin@mail.ru
[**] E-mail: andrej.sobolev@usu.ru
[***] E-mail: dwiebe@inasan.ru
[****] E-mail: semenov@mpia-hd.mpg.de

1063-7737/04/3008-0566$26.00

modeling the chemical evolution of the ISM that are important for our study. Next, we describe the method of analyzing the distribution functions of the model abundances determined by statistically varying the reaction rate constants and present the results of our analysis. Particular attention is paid to the statistics of abundance scatters for molecules with various numbers of atoms. We consider some of the aspects of applying the method in astrophysically interesting cases. We propose a technique that allows the role of various reactions in the abundance evolution of a specific chemical species to be determined and formulate our conclusions.

THE CHEMICAL NETWORK EQUATIONS AND THE RATE CONSTANTS OF CHEMICAL REACTIONS

The chemical evolution of the ISM in the gas-phase approximation (i.e., with the gas–dust interaction disregarded) is described by the system of chemical network equations

$$\frac{dn_i}{dt} = \sum_{l,m} K_{lm} n_l n_m - n_i \sum_s K_{is} n_s, \qquad (1)$$

where n_i is the number density of the ith chemical species, t is the time, K_{lm} and K_{is} are the rate coefficients of the chemical reactions. The expression for calculating the rate coefficient depends on the type of reaction, for example,

$$K = \begin{cases} \alpha\,(T/300)^{\beta}\exp(-\gamma/T)\text{—two-particle reactions} \\ \alpha\text{—reactions with cosmic rays} \\ \alpha\exp(-\gamma A_V)\text{—photoreactions.} \end{cases} \qquad (2)$$

Here, T is the gas temperature, and A_V is the visual extinction. As we see, the rate coefficient is determined by the physical conditions in the ISM and by the constants α, β, and γ. To calculate the reaction rate in Eqs. (1), the coefficient K is multiplied by the number densities of the reagents (molecular number densities) or, depending on the type of reaction, by the cosmic-ray ionization rate ζ or the intensity of the ultraviolet radiation G expressed in terms of the mean interstellar ultraviolet radiation field. The chemical evolution of the ISM is calculated by specifying the initial number densities n_i and physical conditions and by integrating Eqs. (1) in the required time interval. The physical conditions can change with time (nonstationary models) or remain constant (stationary models). Data on the chemical reactions—the reagents, the products, and the constants α, β, and γ—are summarized in several databases; the best-known databases are UMIST 95 (Millar *et al.* 1997), UMIST 99 (Le Teuff *et al.* 2000), and NSM (Lee *et al.* 1998). The reactions and reagents in them number in thousands and hundreds, respectively.

Apart from the choice of reactions to be included in the database and the formula for calculating the rate coefficient K, the constants α, β, and γ, which are measured experimentally or derived theoretically, are the main source of uncertainties in such calculations. The errors in these constants are often large, which affect the reliability of the chemical modeling results. To analyze the role of such errors, we use the UMIST 95 database. The latter is widely used to model the chemical evolution of various astronomical objects; in addition, it contains a rough estimate of the accuracy with which the reaction parameters were determined for each reaction. The UMIST 95 database includes 3864 reactions that combine 394 chemical species. Below, for brevity, we occasionally use the general terms "species" or "molecules" for them, which also always imply neutral and ionized atoms.

When the chemical evolution of dense molecular cloud cores is studied, the gas–dust interaction (including the grain surface reactions) should be included in the model. It is probably impossible to explain the onion-like chemical structure of these cores without including this interaction (Li *et al.* 2002; Aikawa *et al.* 2001). Clearly, including the gas–dust interaction is a source of additional uncertainties. This is particularly true for the surface reactions for which it may be impossible in principle to apply equations of form (1) (Herbst and Shematovich 2003). In this paper, we restrict our analysis to a simpler

Table 1. Physical parameters of the models

Parameter	Dark cloud	Diffuse cloud
Number density of hydrogen nuclei, n	2×10^4 cm^{-3}	5×10^3 cm^{-3}
Gas temperature, T	10 K	30 K
Ultraviolet radiation field, G	0.0	1.0
Extinction, A_V	–	0.5

Table 2. Initial abundances of species in the chemical model

Species	Abundance
C	7.31(−5)
N	2.14(−5)
O	1.76(−4)
Na	2.0(−9)
Mg	3.0(−9)
Fe	3.0(−9)
S	2.0(−8)
Si	3.0(−9)
P	3.0(−9)
Cl	4.0(−9)
The rest	0

case and consider only gas-phase chemical reactions by limiting the densities to values characteristic of molecular clouds as a whole rather than their cores. The gas-phase chemistry can be quite adequate for such objects, as was pointed out, for example, by Terzieva and Herbst (1998) and Turner (2000).

THE METHOD OF CALCULATION AND ANALYSIS OF THE DISTRIBUTION FUNCTIONS FOR MODEL ABUNDANCES

For the UMIST 95 reactions, Millar *et al.* (1997) proposed the following division into classes by the accuracy of the rate constants:

1) an error $< 25\%$;

2) an error $< 50\%$;

3) an error of a factor of 2;

4) an order-of-magnitude error (no more than a factor of 10);

5) a very large error (more than a factor of 10).

Most of the reactions (907) with measured rate constants belong to the first class. The second, third, and fourth classes include 40, 12, and 4 reactions, respectively. None of the reactions belongs to the fifth class. For 2901 reactions, the rate constants were not measured, but estimated theoretically or derived from the known rate constants of similar reactions. The ion–molecular reactions that Millar *et al.* (1997) attributed to the third class constitute a significant fraction of them (1951). For the remaining 950 reactions, the UMIST 95 database gives no class of accuracy, but similar reactions in the UMIST 99 database were generally also included in the third class, with the exception of several reactions attributed to the first class. We assumed all of the reactions with unmeasured rate constants to belong to the third class.

The method of analysis involved creating a large sample of stationary gas-phase chemical evolution models calculated under the same physical conditions with the same set of chemical reactions between the same species, but with different rate constants. For definiteness, we restricted our analysis to the influence of errors in α. Varying this constant results in a linear change of the rate coefficient and does not change such reaction properties as the temperature barrier and others. We chose α in an equiprobable way within the corresponding error interval centered on the constant given in UMIST 95. We generated a total of 10 000 sets of constants α. In our calculations, we used a Mersenne Twister uniform pseudo-random number generator (Matsumoto and Nishimura 1998).

We calculated the chemical evolution models with physical parameters typical of dark molecular clouds and less dense clouds affected by the interstellar radiation field (below, these are called diffuse clouds for short). The physical parameters of the models are given in Table 1. The initial elemental abundances are listed in Table 2. We assumed that all of the hydrogen was initially in molecular form. The physical conditions in the models were assumed to be constant. Integration was performed until the ISM reached a chemical equilibrium. As a result, for each of the two variants of physical conditions, we obtained 10 000 sets of the abundances of chemical species for several times calculated using various realizations of α. Below, the abundances at the end of our calculations are called equilibrium abundance, although it should be borne in mind that these were calculated using the nonequilibrium equations (1).

Pineau des Forets and Roueff (2000) used a technique of varying the rate constants similar to that described in this section to study the conditions for the onset of bistability in the equilibrium abundances of electrons and several carbon-containing species. These authors did not analyze in detail the abundance variations for all of the species from the UMIST 95 database.

RESULTS

Sensitivity Groups

Figure 1 shows the histograms of abundances for some of the molecules constructed from all of the 10 000 realizations for dark and diffuse clouds. Notice the asymmetry in the distribution, which is particularly large for HCO^+ and SO in the case of a dark cloud. For HCO^+, this asymmetry, for example, implies that correcting the rate constants (within the limits specified in UMIST 95) will most likely lead only to a *decrease* in the calculated abundance of this molecule in dark clouds, not to its increase. The N_2H^+ abundance distribution for a diffuse cloud shows a reverse (although not so distinct) tendency: correcting the rate constants will lead to an *increase* in the calculated abundance of this ion with a higher probability.

An analysis of similar histograms for all of the molecules from the UMIST 95 set suggests that the width of the histogram (the scatter in values) depends on the complexity of the molecule (the number of its constituent atoms). To describe this dependence quantitatively, we divided all of the species into the following groups of abundance sensitivity to variations in the reaction rate constants according to the full width at half maximum (FWHM) of the histogram:

(1) Spread in abundances is <0.25 order of magnitude.

(2) Spread in abundances is 0.25–0.5 order of magnitude.

(3) Spread in abundances is 0.5–1.0 order of magnitude.

(4) Spread in abundances is 1.0–2.0 orders of magnitude.

(5) Spread in abundances is 2.0–3.0 orders of magnitude.

(6) Spread in abundances is >3.0 orders of magnitude.

For various sensitivity groups, Fig. 2 shows the histograms that reflect the number of chemical species in the group as a function of the number of atoms in their molecules. For both variants of the ISM physical parameters, there is a clear tendency for more complex species to fall into a sensitivity group with a larger number. The reason is that longer sequences of chemical reactions lead to the formation of more complex species rather than to the formation of simple species. The accumulating errors in the rate constants of the chemical reactions in long sequences significantly reduce the accuracy with which the abundance of the end product, the complex molecule under consideration, is calculated.

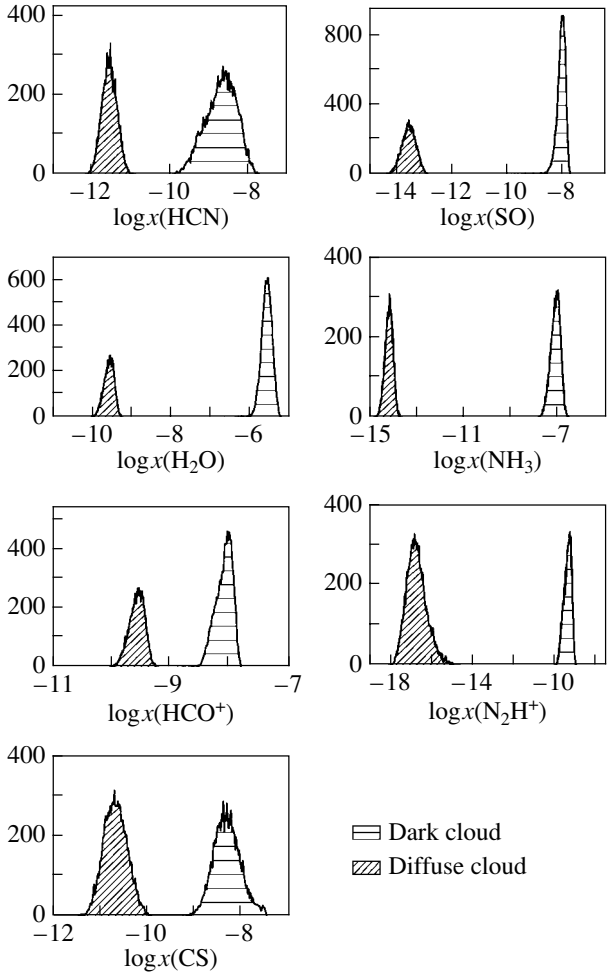

Fig. 1. Abundance distributions for some of the observed molecules constructed from 10 000 realizations of constants α.

A dark cloud. In this case, we considered a medium in which the physical conditions were typical of most of the observed molecular clouds. Table 3 gives the distribution of most of the observed atomic and molecular species in sensitivity groups (the full table for all of the 394 species would be too large; when constructing the histograms in Fig. 2, we took into account all species). Twelve chemical species fell into group 1 (apart from those listed in the table, it also includes N_2 and O_2). The absolute majority of the 394 species fell into groups 2, 3, and 4 (34, 111, and 146 species, respectively). Groups 2 and 3 include most of the commonly observed molecules (CS, H_2CO, NH_3, CH_3OH, H_2O, CH_4, HCN, and others). Some of the observed species, in particular, HC_3N and C_2S, fell into group 4. Groups 5 and 6 include mostly complex molecules with long carbon chains formed at the end of a complex sequence of chemical reactions. There are almost no observed molecules among these. The dominant ion is HCO^+,

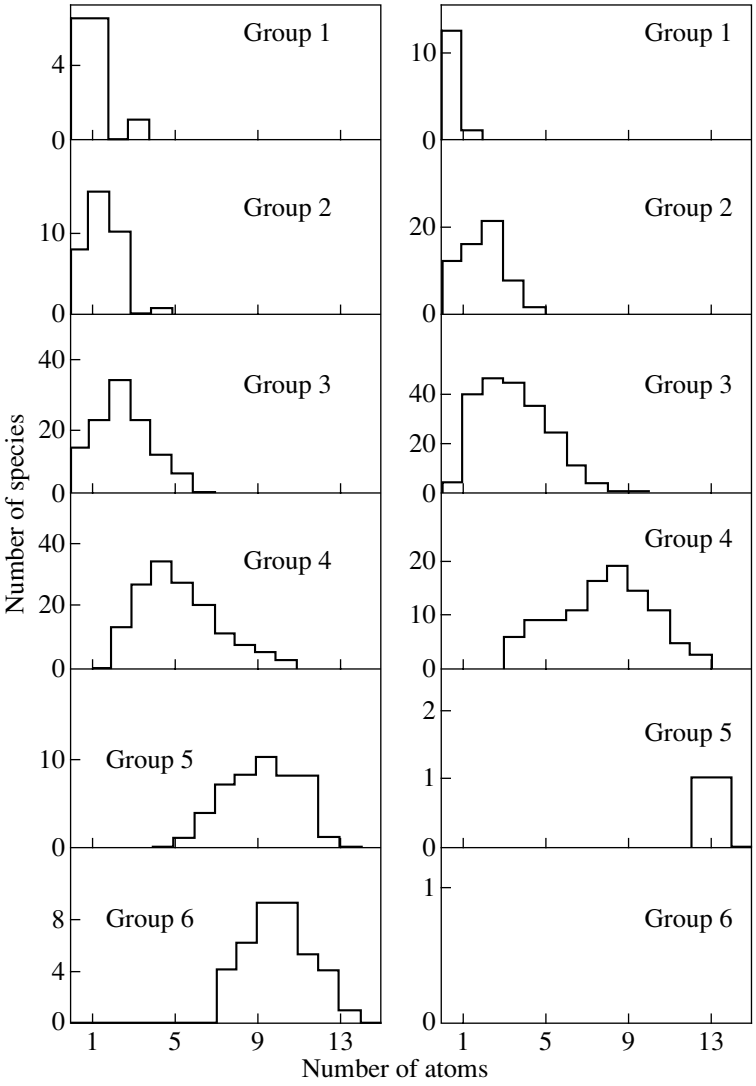

Fig. 2. Distributions of molecules in the number of atoms separately for each sensitivity group. The left and right columns correspond to dark and diffuse clouds, respectively.

which belongs to the second group, but the contribution of metal ions from the first group to the degree of ionization is also very large. As a result, the electrons fell into the first group.

A diffuse cloud. The physical conditions in a diffuse cloud differ from those in a dark cloud by the lower gas density and the presence of an ultraviolet background, a factor that prevents the formation of complex species. As we see from Fig. 2, the distribution of molecules in sensitivity groups changed somewhat, but the tendency mentioned above was retained. The distribution of observed atomic and molecular species in sensitivity groups is illustrated in Table 4. Most of the species (213) fell into group 3. The number of them in group 4 is 105, less than that in a dark cloud. As in the previous case, group 5 includes complex molecules with long carbon chains; this time there are only two such molecules, $C_9H_5^+$ and $C_8H_5^+$. In Table 4, these are given in parentheses, because observations have not yet revealed these molecules. None of the species fell into group 6. Since the electron abundance is determined by the carbon ion abundance, the electrons fell into group 1.

A comparison of the dark and diffuse model clouds shows that the scatter in theoretical abundances attributable to the uncertainties in the rate constants of chemical reactions depends on the physical conditions in the medium. Including ultraviolet radiation in the model (and, accordingly, taking into account photoreactions) can lead to an increase in the uncertainties of the theoretical abundances, as, for example, with N_2H^+, and to their decrease, as with C_2S. In particular, it should be noted that in a diffuse cloud, such observationally important molecules as

Table 3. Distributions of the observed species in sensitivity groups for a dark model cloud

Group 1	Group 2	Group 3		Group 4		Group 5	Group 6
H_2	H	C	NH_2	C_2	H_2C_3	C_4	HC_9N
He	O	S	HCO	C_2H_4	H_2CN	H_3C_4N	C_8H
P	Fe	Si	N_2O	C_2H_5OH	H_2CS	HC_5N	HC_7N
Cl	Na	CH	C_2H	C_2H_6CO	HC_3N	C_5H_4	
CO	Mg	NH	C_3O	C_2S	SiS	C_6H	
SiO	SO	OH	C_2H_2	C_3	$HCOOCH_3$	C_6H_2	
H_3O^+	SO_2	HS	H_2CO	C_3H	HNC	H_3C_6N	
Na^+	H_2O	NO	CHOOH	C_3H_4	SiC	C_7H	
Mg^+	HCl	NS	CH_3OH	C_3N	SiC_2	C_5	
Fe^+	SO^+	N	SiH_4	C_3S	SiC_4	C_5H	
	H^+	CP	NH_3	C_4H	SiNC	C_5N	
	H_3^+	PN	C^+	C_4H_2	HCO_2^+		
	O^+	H_2S	N^+	CH_3OCH_3			
	CO^+	SiN	S^+	CH_3CN			
	HCO^+	CS	Si^+	CH_3CHO			
	HOC^+	CH_2	Cl^+	CCO			
	N_2H^+	CH_4	P^+	CN			
		HNO	HCS^+	CH_2CN			
		CO_2	$HCNH^+$				
		OCS	CH^+				
		HCN	HC_3O^+				

CO and N_2H^+ fell into group 3, with the uncertainty in their equilibrium abundances reaching an order of magnitude, while in a dark cloud, these were included in the first (CO) and second (N_2H^+) groups. This is probably because almost all of the photoreactions in the UMIST 95 database, including the CO, CS, and N_2 (the parent molecule for N_2H^+) photodissociation reactions, were attributed to the third class of accuracy. On the other hand, since the molecular composition is relatively poor, the number of paths that lead to the formation of complex molecules decreases, and, hence, their abundances are calculated more accurately than those for a dark cloud.

Influence of the Choice of Error Distribution

The above results were obtained by assuming a uniform error distribution for the rate constants of chemical reactions within the range specified in UMIST 95. To check whether these change for a different error distribution, we calculated 5000 chemical evolution models for a dark cloud with the same physical and chemical parameters, but using different sets of constants α. All of the constants were randomly and uniformly varied within 25% of the standard value (i.e., all of the reactions were assumed to belong to the first class of accuracy). The histograms of molecular abundances retained a shape similar to that of the histograms in Fig. 1, but with a smaller scatter. Thus, the choice of a different error distribution does not radically change our conclusions.

ERRORS IN THE RATE CONSTANTS OF CHEMICAL REACTIONS AND PARAMETERS OF MOLECULAR CLOUDS

For both variants of physical conditions under consideration, the uncertainties in the abundances of light molecules do not exceed one order of magnitude, which corresponds to the accuracy of their abundances from observations. In other words, the abundances of simple molecules in current astrochemical

Table 4. Distributions of the observed species in sensitivity groups for a diffuse model cloud

Group 1	Group 2		Group 3			Group 4	Group 5	Group 6
H_2	H	O^+	C_2H	CP	SiN	CH_3OCH_3	$(C_8H_5^+)$	–
He	C	N^+	C_2H_2	CS	SiNC	$HCOOCH_3$	$(C_9H_5^+)$	
N	Mg	H_3^+	C_2H_4	CN	SiO	C_2H_5OH		
O	Na	CO^+	C_2S	H_2C_3	SiS	C_2H_6CO		
Cl	Fe	CH^+	C_3H	H_2CN	SO	C_3		
C^+	P	H_3O^+	C_3H_4	H_2CO	SO_2	C_3N		
Mg^+	S	HCO^+	C_3O	H_2CS	HC_3O^+	C_4H_2		
Na^+	Si	HOC^+	C_3S	H_2S	HCO_2^+	H_3C_4N		
Fe^+	C_2	HCS^+	C_4	HC_3N	N_2H^+	C_5H		
S^+	CH	$HCNH^+$	C_4H	HCl	SO^+	C_5H_4		
Si^+	CH_2		C_5	HCO		C_5N		
P^+	H_2O		CCO	HNO		HC_5N		
Cl^+	HCN		CH_2CN	N_2O		C_6H		
	HNC		CH_3CHO	NO		C_6H_2		
	HS		CH_3CN	NS		H_3C_6N		
	NH		CH_3OH	OCS		C_7H		
	NH_2		CH_4	PN		C_8H		
	NH_3		CHOOH	SiC		HC_7N		
	OH		CO	SiC_2		HC_9N		
	H^+		CO_2	SiH_4		SiC_4		

models are modeled with an accuracy comparable to the accuracy of the observational data. However, as the number of atoms in molecules increases, the uncertainties in the abundances increase. This tendency shows up particularly clearly for molecules with long carbon chains. For molecules with 4-atom and 8–9-atom carbon chains, the probable error is about two orders of magnitude and larger than 3.5 orders of magnitude, respectively.

The observed abundances of chemical species are an important source of information about the evolutionary status of molecular clouds and about some of the physical parameters of star-forming regions such as the intensity of the cosmic rays and ultraviolet radiation. The accuracy of interpreting the observational data is largely determined by the accuracy of modeling the chemical evolution of the ISM. The question arises as to how strong the effect of uncertainties in the calculated abundances on the parameters of molecular clouds determined from them can be. A detailed study of this question is beyond the scope of this paper. As an example, we consider only two molecules, HC_3N and C_2S. In the gas-phase approximation, these molecules are believed to be typical representatives of the early-time chemistry and reach their maximum abundances by $t \sim 10^5$ yr. The significant abundance of HC_3N and other cyanopolyynes in TMC-1, for example, is suggested as evidence that this object is chemically young (Hirahara *et al.* 1992) (which, however, does not rule out a different interpretation offered by Ruffle *et al.* (1997)).

However, our calculations indicate that in a dark model cloud with parameters that are similar to the observed parameters of TMC-1, HC_3N, and C_2S fall into group 4, while the more complex cyanopolyynes (HC_5N etc.) fall into groups 5 and 6. This implies that errors in the rate constants of chemical reactions can lead to uncertainties in the equilibrium abundances of these molecules up to several orders of magnitude, as illustrated in Fig. 3. Figure 3a plots the time dependence of the HC_3N abundance calculated for various sets of α that provided the maximum and minimum equilibrium abundances as well as the equilibrium abundances corresponding to half the height of the

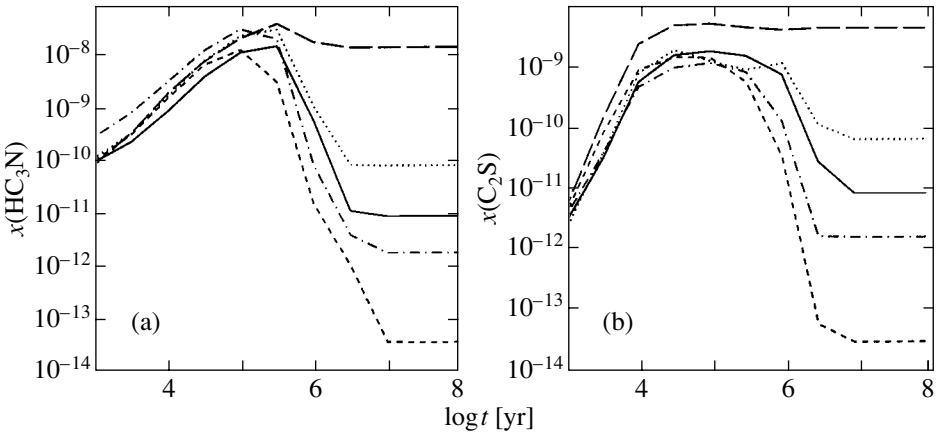

Fig. 3. Evolution of the HC_3N and C_2S molecular abundances for various sets of rate constants.

histogram for this molecule. Figure 3b shows similar plots for C_2S. We see from Fig. 3a that for variations in the equilibrium HC_3N abundance reaching several orders of magnitude, the time it takes for the equilibrium abundance of this molecule to reach its maximum changes appreciably (from 10^5 to 3×10^5 yr). The maximum and minimum HC_3N abundances in our models at time $t \approx 3 \times 10^5$ yr (which is close to the age estimate for TMC-1) differ by more than an order of magnitude. The peak in the C_2S abundance is flatter, and its shift is smaller when varying α.

One may assume that the abundances of various cyanopolyynes are not independent and expect that the situation with the determination of cloud parameters might improve when using the abundance ratios instead of the abundances themselves (as, e.g. suggested by Stahler (1984)). However, our calculations indicate that this is not the case. Figure 4 shows histograms of the HCN/HC_3N and HC_3N/HC_5N equilibrium abundance ratios for all 10 000 realizations of α. Clearly, the scatter in equilibrium abundance ratios exceeds two orders of magnitude for both dark and diffuse clouds, as does the scatter in the abundances themselves. Our calculations show that varying the reaction rate constants can also result in significant qualitative changes of the ratio $x(\mathrm{HCN})/x(\mathrm{HC_3N})$ with time. This is also true of the ratio $x(\mathrm{HC_3N})/x(\mathrm{HC_5N})$.

In any case, our preliminary calculations indicate that there can be significant errors in the ages of molecular clouds estimated quantitatively from the molecular abundances or their ratios. On the other hand, some of the qualitative conclusions remain unchanged. For example, the HC_3N and C_2S molecules still belong to the early-time chemistry if the rate constants are varied within admissible limits.

CORRELATION BETWEEN THE ABUNDANCES AND THE RATE CONSTANTS OF INDIVIDUAL REACTIONS

In the previous section, we showed that the uncertainties in the theoretical abundances of many molecules are several orders of magnitude. The question of searching for effective ways of reducing the uncertainties in the model abundances of chemical species arises. The method of varying the rate constants used here allows the correlation between the abundance of a given molecule and the rate constants of individual reactions to be estimated. In general, the abundance evolution for most of the molecules is determined by a significant number of reactions. Since the chemical network equations are nonlinear and since their number is large, it is generally impossible to establish any simple relations between the rate constants and the abundances of various molecules. However, based on the correlation coefficients between the rate constants and the abundances of various species, we can identify the reactions whose errors in the rate constants make the largest contribution to the uncertainty in the abundance of the species concerned.

In this section, we explore the possibility of identifying a small number of chemical reactions that make the largest contribution to the uncertainty in the abundance of a selected species. We also consider the influence of an improvement in the rate constants of these reactions on the accuracy of calculating the theoretical abundance of this molecule.

We searched for the reactions as follows: Using 10 000 modified versions of the UMIST 95 database, we calculated 10 000 equilibrium abundances for each species in a dark model cloud. We calculated the linear correlation coefficients between these abundances and the rate constants for each of the 3864 reactions from UMIST 95.

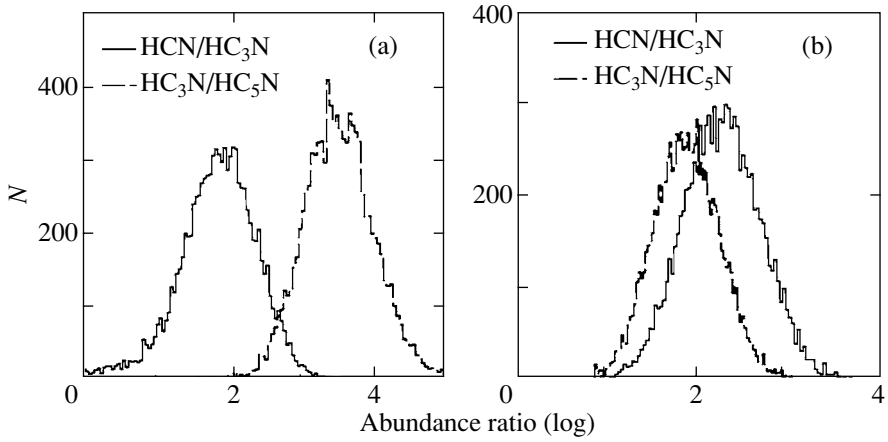

Fig. 4. Histograms of the logarithms of cyanopolyynes equilibrium abundance ratios for 10 000 realizations of rate constants for dark (a) and diffuse (b) clouds.

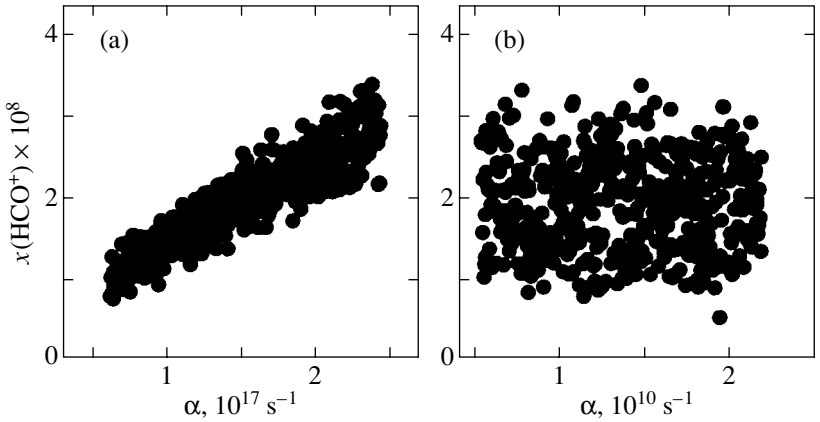

Fig. 5. Distribution of the model HCO^+ abundances in the abundance–rate constant plane for the reactions H_2 + c.r.p. → $H_2^+ + e^-$ ((a) $R = 0.84$) and C + NH → CN + H ((b) $R = 0.01$).

As might be expected, the reaction of molecular hydrogen ionization by cosmic rays H_2 + c.r.p. → $H_2^+ + e^-$, which eventually produces H_3^+, is one of the most significant reactions for simple molecules. For example, the correlation coefficient between the equilibrium HCO^+ abundance and the rate constant of this reaction is $R = 0.84$. In Fig. 5a, the equilibrium HCO^+ abundance is plotted against the rate constant of this reaction. In general, a relatively small number of reactions (~10) whose errors in the rate constants make the largest contribution to the uncertainties in the abundances are identified for simple species. The correlation coefficients for most of the reactions are insignificant. For example, Fig. 5b shows the distribution of equilibrium HCO^+ abundances in the same plane for the reaction C + NH → CN + H (the correlation coefficient with the HCO^+ abundance is $R = 0.01$). There is no correlation between the abundance and the rate constant of this reaction.

Note, in particular, that the reactions with significant correlation coefficients between their rate constants and the abundance of a selected species (particularly for the equilibrium abundances) should not be unequivocally identified with the reactions that are the main production/destruction channels of the selected molecule. The large correlation coefficients between the rate constants and the abundance of a selected molecule at a certain time only imply that the errors in the rate constants of precisely these reactions make the largest contribution to the uncertainty of this abundance at that time. The correlation technique and its possible applications are to be analyzed in detail in subsequent publications.

In general, several reactions with a correlation coefficient R appreciably larger than its value for other reactions are identified for each species. As an example, Table 5 lists the reactions with the largest correlation coefficients between their rate constants and the equilibrium cyanopolyyne abundances. This table

Table 5. Correlation coefficients between the rate constants and the cyanopolyyne abundances

Reaction	R
HCN	
$He + c.r.p. \rightarrow He^+ + e^-$	0.55
$N^+ + H_2 \rightarrow NH^+ + H$	0.16
$He^+ + N_2 \rightarrow N^+ + N + He$	0.16
$NH_4^+ + e^- \rightarrow NH_3 + H$	0.13
$HCNH^+ + e^- \rightarrow HCN + H$	0.10
$HCNH^+ + e^- \rightarrow CN + 2H$	−0.10
$NH_4^+ + e^- \rightarrow NH_2 + 2H$	−0.12
$H_2 + c.r.p. \rightarrow H_2^+ + e^-$	−0.50
HC_3N	
$He + c.r.p. \rightarrow He^+ + e^-$	0.22
$CN + C_2H_2 \rightarrow HC_3N + H$	0.07
$H_3^+ + O \rightarrow OH^+ + H_2$	−0.14
$H_2 + c.r.p. \rightarrow H_2^+ + e^-$	−0.26
HC_5N	
$He + c.r.p. \rightarrow He^+ + e^-$	0.14
$H_3^+ + CO \rightarrow HCO^+ + H_2$	0.05
$H_3^+ + O \rightarrow OH^+ + H_2$	−0.12
$H_2 + c.r.p. \rightarrow H_2^+ + e^-$	−0.18
HC_7N	
$He + c.r.p. \rightarrow He^+ + e^-$	0.11
$CH_3^+ + H_2 \rightarrow CH_5^+ + h\nu$	0.04
$H_3^+ + O \rightarrow OH^+ + H_2$	−0.09
$H_2 + c.r.p. \rightarrow H_2^+ + e^-$	−0.13
HC_9N	
$He + c.r.p. \rightarrow He^+ + e^-$	0.10
$H_3^+ + SiC_2H_2 \rightarrow SiC_2H_3^+ + H_2$	0.04
$H_3^+ + O \rightarrow OH^+ + H_2$	−0.08
$H_2 + c.r.p. \rightarrow H_2^+ + e^-$	−0.12

contains a number of reactions that play an important role in the chemistry of cyanopolyynes. However, apart from the latter, the table includes the reactions whose role in the chemistry of these species is not so obvious. In addition, the correlation coefficients of the rate constants for some of the key (for the chemistry of cyanopolyynes) reactions (in particular, reactions of the type $He^+ + HC_{(5,7,9)}N$) proved to be insignificant. Thus, Table 5 is a good illustration of the assertion made in the previous paragraph.

The proposed method allows the extent to which a theoretical or experimental improvement in the reaction rate constant reduces the uncertainty in the model abundance of a selected species at a given time to be determined even at the initial stage. For this purpose, it will suffice to identify the range about the most probable reaction rate constant on the x axis that corresponds to the spread in rate constants after an improvement in a diagram similar to Fig. 5 and to calculate the scatter in the abundances of the species within the range on the y axis.

CONCLUSIONS

We have considered the influence of uncertainties in the rate constants of chemical reactions on the reliability of the gas-phase chemical evolution models for the ISM. The UMIST 95 database was used as the basis for our study. Our analysis revealed a dependence of the uncertainty in the model abundance of a molecule on the number of atoms in it: the larger the number of atoms in the molecule, the greater the uncertainty. For molecules with a small number of atoms, the uncertainties in their abundances are close to the observational errors in the abundances, 0.5–1.5 orders of magnitude. At the same time, errors in the rate constants of chemical reactions significantly affect the model abundances of complex molecules with long carbon chains by changing them by 2.5–3.5 orders of magnitude, which is much worse than the observational accuracy of the abundance determination. The errors in the abundances depend not only on the rate constants of chemical reactions, but also on the physical conditions under which the chemical evolution of the ISM is calculated. Uncertainties in the rate constants of chemical reactions can lead to significant errors in the estimated parameters of molecular clouds.

All of the species included in UMIST 95 were divided into six groups of sensitivity of their equilibrium abundances to errors in the rate constants. When the physical conditions change, a significant redistribution of the species between the sensitivity groups takes place. We show this effect using two samples as an example: one was calculated for physical parameters typical of a dark cloud, and the other was calculated for a diffuse cloud.

In general, our study indicates that modeling the chemical processes in molecular clouds using UMIST 95 leads to uncertainties in the theoretical abundances of simple molecules that do not exceed the observational errors.

We proposed a method of searching for the chemical reactions whose rate constants affect most

strongly the model abundance of a given species. This method also allows us to tentatively estimate the extent to which an improvement in the rate constants of these reactions increases the accuracy of the abundance of the species under consideration and to identify the constants whose theoretical or experimental improvement is most desirable.

ACKNOWLEDGMENTS

We wish to thank A.B. Ostrovskiĭ and M.S. Kirsanova for their valuable remarks and fruitful discussions. The work of A.I. Vasyunin and A.M. Sobolev was supported by the INTAS grant no. 99-1667, the Russian Foundation for Basic Research (project no. 03-02-16433), and the RF Ministry of Education. The work of D.S. Wiebe was supported by the Russian Foundation for Basic Research (project nos. 02-02-04008 and 01-02-16206) and an RF Presidential Grant (NSh-162.2003.2). The work of D.A. Semenov was supported by DFG grant He-1935/17-2.

REFERENCES

1. Yu. Aikawa, N. Ohashi, S.-I. Inutsuka, *et al.*, Astrophys. J. **552**, 639 (2001).
2. E. van Dishoeck and G. Blake, Annu. Rev. Astron. Astrophys. **36**, 317 (1998).
3. E. Herbst and V. I. Shematovich, ASP Conf. Ser., 2003 (in press).
4. Y. Hirahara, H. Suzuki, S. Yamamoto, *et al.*, Astrophys. J. **394**, 539 (1992).
5. H.-H. Lee, E. Roueff, G. Pineau des Forêts, *et al.*, Astron. Astrophys. **334**, 1047 (1998).
6. Y. H. Le Teuff, T. J. Millar, and A. J. Markwick, Astron. Astrophys., Suppl. Ser. **146**, 157 (2000).
7. Z.-Y. Li, V. I. Shematovich, D. S. Wiebe, and B. M. Shustov, Astrophys. J. **569**, 792 (2002).
8. M. Matsumoto and T. Nishimura, ACM Trans. Modell. Comp. Simul. **8**, 3 (1998).
9. T. J. Millar, P. R. A. Farquhar, and K. Willacy, Astron. Astrophys., Suppl. Ser. **121**, 139 (1997).
10. G. Pineau des Forêts and E. Roueff, Philos. Trans. R. Soc. London, Ser. A **358**, 2549 (2000).
11. D. P. Ruffle, T. W. Hartquist, S. D. Taylor, and D. A. Williams, Mon. Not. R. Astron. Soc. **291**, 235 (1997).
12. S. W. Stahler, Astrophys. J. **281**, 209 (1984).
13. R. Terzieva and E. Herbst, Astrophys. J. **501**, 207 (1998).
14. B. E. Turner, Astrophys. J. **542**, 837 (2000).

Translated by V. Astakhov

Astronomy Letters, Vol. 30, No. 8, 2004, pp. 577–581. Translated from Pis'ma v Astronomicheskiĭ Zhurnal, Vol. 30, No. 8, 2004, pp. 635–640.

On the Variations in the Parameters of High-Degree Acoustic Modes with Solar Cycle

Sh. S. Kholikov, O. S. Burtseva*, A. V. Serebryanskiy, and Sh. A. Ehgamberdiev

Astronomical Institute, Academy of Sciences of Uzbekistan, Astronomicheskaya ul. 33, Tashkent, 700052 Uzbekistan

Received December 16, 2003

Abstract—We analyze the pattern of behavior of p-mode wave packets with solar cycle using TON one-day helioseismic data with a high spatial resolution. The time–distance method is used to perform this task. We make an attempt to determine the variations in the travel time of acoustic waves at maximum and minimum solar activity; at maximum activity, this time decreases by 2 s compared to that at minimum activity to a depth of $0.8R_\odot$. In addition, the correlation amplitudes of acoustic wave packets from minimum to maximum solar activity were found to decrease by 10–20% for all angular distances.

Key words: *Sun, acoustic oscillations, solar activity.*

INTRODUCTION

In observational helioseismology, such basic parameters of individual oscillation modes as the frequencies, line widths, and amplitudes have been determined by analyzing their power spectra (Serebryanskiy *et al.* 2001; Fossat *et al.* 2003). By now, all these parameters have been measured with a high accuracy, and their variations with solar cycle have been studied. The observed frequencies are in good agreement with their theoretical values. These measurements were based mostly on the Fourier expansions of helioseismic time series of intensities or Doppler velocities.

With the advent of the new method for analyzing helioseismic data (time–distance analysis) that was first developed by Duvall *et al.* (1993), it became possible to study the physical parameters of local regions near the solar surface by analyzing the perturbations of the travel time of the acoustic-mode wave packets produced by local inhomogeneities. In addition, such methods of local diagnostics of the solar interior as acoustic holography (Roddier 1975; Lindsey and Braun 1990; Braun *et al.* 1992), acoustic imaging (Chang *et al.* 1997), and other methods (Chou and Serebryanskiy 2002) based on time-distance relations have been developed. In contrast to the standard methods of analysis, all calculations in time–distance analysis are performed in the time domain rather than the frequency domain. The main idea of this method is to measure the travel time of acoustic waves on the Sun, which, in turn, provides information about the properties of the matter, the speed of sound, the magnetic field, and the flows.

On the Sun, acoustic waves propagate in an inhomogeneous, anisotropic, and dispersive medium. In contrast to terrestrial seismic waves whose source is localized, solar waves are generated stochastically, by many sources in the subsurface layer of the convective envelope, and individual sources cannot yet be observed. The acoustic signal that reaches the solar surface is reflected and propagates back to the solar interior, bends its path due to an increase in the speed of sound with depth, and again returns to the surface, emerging at a certain distance from the starting point. Different waves (with different frequencies and spatial sizes) follow different path and reach the surface in different time intervals and at different distances from the starting point. However, modes with the same angular phase velocity ω/l (where ω is the cyclic frequency, and l is the degree of the acoustic mode) follow approximately the same ray path (Duvall 1982). These modes form a wave packet that propagates from point to point on the solar surface. The relationship between the travel time and the angular distance traversed by the wave packet can be obtained by constructing a cross-correlation function (Duvall *et al.* 1993). Each point on the time–distance curve corresponds to the wave packet formed by modes with equal values of w/l.

The cross-correlation function of oscillating signals f for two points with coordinates r_1 and r_2 on

*E-mail: olga@astrin.uzsci.net

1063-7737/04/3008-0577$26.00

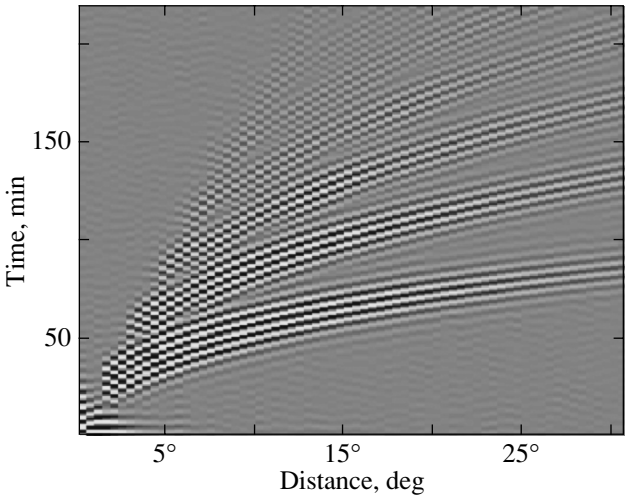

Fig. 1. Cross-correlation function calculated from the TON one-day series.

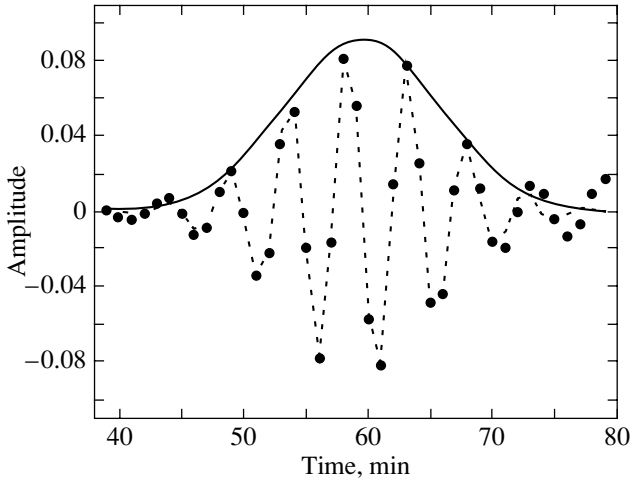

Fig. 2. Cut of the cross-correlation function for $\Delta \approx 10°$ and its fit by the Gabor function (for clarity, the Gabor envelope is shown).

the solar surface is defined as

$$C(\tau, \Delta) = \int_0^T f(r_1, t+\tau) f^*(r_2, t) dt, \qquad (1)$$

where Δ is the angular distance between the two points, and T is the total duration of the observations. The delay τ specifies the time shift between the two signals.

The cross-correlation function for any fixed Δ has several maxima that correspond to the next appearances of wave packets on the solar surface. These maxima occur at certain values of the time required for a wave packet with a given angular phase velocity to propagate from one point of the surface to the other, following a certain ray path. Since the appearances of a wave packet on the solar surface have a bouncing pattern, these are called bounces.

To isolate a certain frequency range of p-modes, the following Gaussian frequency filtering is applied to the data:

$$e^{-0.5\left(\frac{\nu-\nu_0}{w}\right)^2}, \qquad (2)$$

where ν_0 is the central frequency, and w is the width of Gaussian filter; as a result, the cross-correlation function $C(\tau, \Delta)$ is described by the Gabor function

$$G = A \cos\left[2\pi\nu\left(t - \tau_{\rm ph}\right)\right] \exp\left[-\frac{(t-\tau_{\rm en})^2}{2\sigma^2}\right]. \qquad (3)$$

Here, A, ν, and σ are the amplitude, central frequency, and envelope width of the Gabor function, respectively; $\tau_{\rm ph}$ and $\tau_{\rm en}$ are the propagation times of the wave-packet phase and envelope, respectively (Duvall *et al.* 1993, 1996).

It should be noted that the Gabor envelope width in the cross-correlation function is inversely proportional to the width of the Gaussian used in the frequency filtering: $\sigma \propto 1/w$. The wider the Gaussian filter, the narrower the Gabor envelope in the cross-correlation function.

THE DATA AND THEIR PREPROCESSING

In this paper, we used data obtained in the TON (Taiwan Oscillation Network) project, whose instruments were installed on Tenerife (Spain); at the Big Bear Observatory (United States); and in Tashkent (Uzbekistan). The TON instrument images the Sun in the Ca^+ K line with a 16-bit water-cooled 1080×1080-pixel CCD array. The mean diameter of the solar image on the CCD array is 1000 pixels. Images are recorded once a minute; thus, ~600 image files are obtained on a typical observing day. The amplitude of the intensity oscillations is about 2.5% (Chou *et al.* 1995). A huge number of one-day series of observations spanning the period 1994–2003 have been accumulated to date as part of this project. The TON database is located at the Tsing Hua University (Hsingchu, Taiwan).

The TON data preprocessing includes the following:

(1) dark-current removal and flat fielding;

(2) correction for the solar limb darkening;

(3) remapping the images to the latitude–longitude grid in $(\sin\theta, \phi)$ coordinates using the GRASP (IRAF) software package, where θ and ϕ are the latitude and the longitude in spherical coordinates, respectively; the pixel values lie at equally spaced points

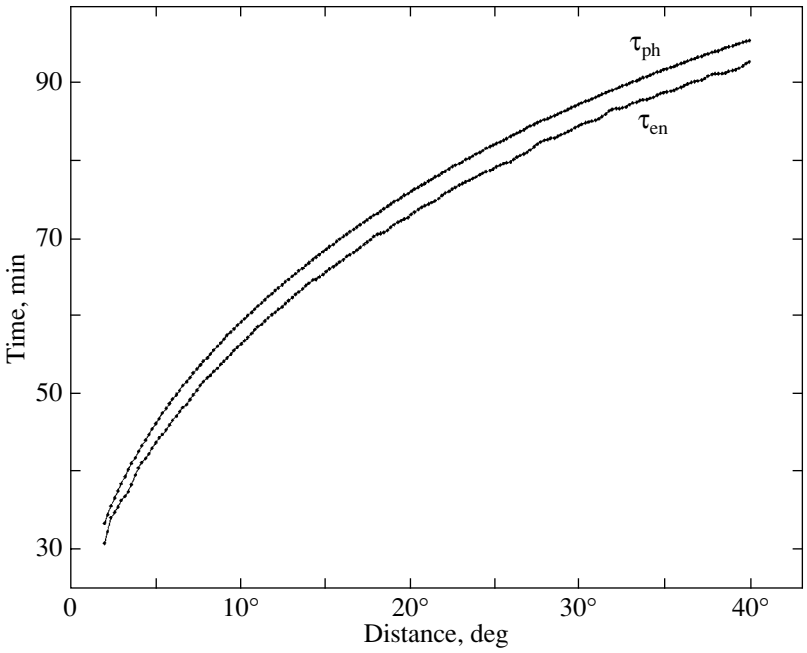

Fig. 3. Time–distance curves obtained from 12 one-day cross-correlation functions. The phase travel time $\tau_{\rm ph}$ is assumed to be the next maximum after the peak of the envelope travel time $\tau_{\rm en}$, i.e., $\tau_{\rm en}$ is always shorter than $\tau_{\rm ph}$.

in the interval $-90^\circ \le \phi \le +90^\circ$ and $-1 \le \sin\theta \le +1$; the size of the remapped image is 1024×1024 pixels;

(4) correction for the surface differential rotation using the formula by Libbrecht and Morrow (1991);

(5) removal of the daily trend and long-period oscillations by subtracting a 15-min running mean.

DERIVING THE TIME–DISTANCE RELATIONS

The following procedure was used to derive the time–distance relations:

(1) We performed the frequency filtering of the preprocessed data by a Gaussian window (see (2)) centered on a 5-min solar oscillation region with a certain width (here, we used a Gaussian filter with the width $w = 0.85$ mHz).

(2) We calculated the cross-correlation function using formula (1). Here, we obtained the cross-correlation functions for 12 TON one-day data series of 1996 (near the solar minimum) and 12 TON one-day series of 2000 (near the solar maximum).

Figure 1 shows the cross-correlation function calculated from a 512-min one-day series. The angular distance between points on the solar surface is along the horizontal axis, and the time is along the vertical axis. In this figure, we clearly see several ridges that correspond to the first, second, third, etc. appearances of wave packets on the solar surface.

RESULTS OF THE ANALYSIS OF TIME–DISTANCE CURVES

Figure 2 shows the cut of the cross-correlation function in Fig. 1 at an angular distance $\Delta \approx 10^\circ$ near the maximum of the first bounce and its fit by the Gabor function (3).

In this paper, we restricted our analysis to the first ridge of the cross-correlation function, i.e., the first appearance of a wave packet on the solar surface. This is the cross-correlation between the signal at a given point and the signals at points offset by a given angular distance from it, i.e., forming a circle of radius Δ. Fitting the cross-correlation function at all angular distances, we obtain the time–distance curve (Fig. 3). Each point (Δ, τ) on this curve corresponds to the oscillation modes that have the same angular phase velocity ω/l and that form a wave packet propagating roughly along the same ray path, where τ is the time it takes for the wave packet to traverse the path in the solar interior between two points on the surface separated by the angular distance Δ.

Since the time–distance curves carry fairly accurate information about the propagation of acoustic waves in the solar interior, we attempted to determine the variations in the travel time of acoustic waves at the solar maximum and minimum. Our results show that the difference between the wave travel times at the minimum and maximum is $\sim$2 s down to a depth of $0.8R_\odot$; at larger depths, this difference decreases (Fig. 4). This probably suggests that acoustic waves penetrating deeper than $0.8R_\odot$ are less sensitive to

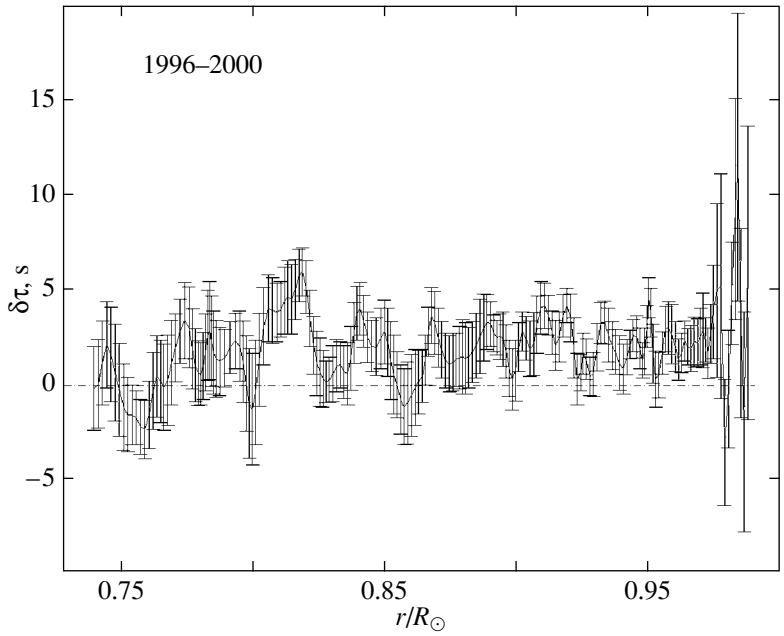

Fig. 4. Difference between the travel times of acoustic waves at the solar minimum and maximum versus their penetration depth, in fractions of $R_\odot$.

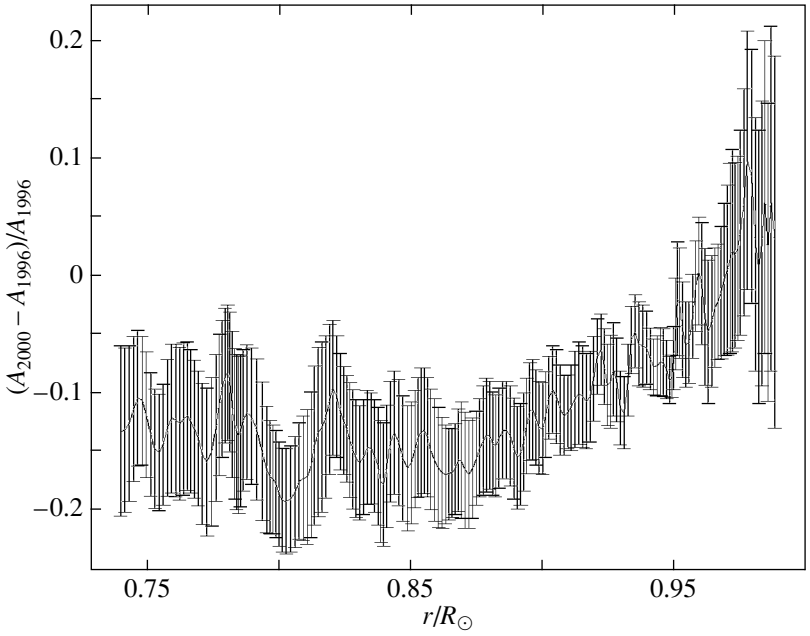

Fig. 5. Relative variations in the correlation amplitudes of wave packets with solar cycle versus their penetration depth, in fractions of $R_\odot$.

solar activity manifestations; i.e., active structures are localized in the upper layer of the convective zone. However, the accuracy of such studies is known to decrease with increasing spatial size of the waves; therefore, it is premature to draw firm conclusions about the radius of influence of solar activity. Nevertheless, in future studies based on more extensive material, this method could yield thickness estimates for the layer of the convective zone that makes the largest contribution to the variations in the travel time of p-modes.

The amplitude A measures the degree of correlation of the wave packet of acoustic oscillations that returns to the surface at distance Δ from the

starting point after its passage along the ray path. The physical parameters of the medium in which acoustic waves propagate are known to vary with solar magnetic activity. However, these variations are very small, although the parameters of the medium in active regions vary significantly; the variations of the magnetic field are particularly large. As a wave packet interacts with active regions, it must lose part of its energy (Chou *et al.* 1996); therefore, in the years of maximum solar activity, when the number of active structures on the Sun increases, the amplitudes of acoustic wave packets must decrease. Figure 5 shows relative variations in the correlation amplitudes of wave packets with solar activity, whence we see that the decrease in the correlation amplitudes of wave packets from minimum to maximum solar activity is 10–20%.

CONCLUSIONS

Time–distance analysis is an efficient method for measuring the variations in the physical parameters of the medium with a high accuracy; our studies confirm this fact once again. Two main conclusions that follow from the results of this work should be noted.

(1) Due to the high accuracy of the derived time–distance relations, we measured the variations in the travel time of acoustic waves at maximum and minimum solar activity. These variations are ~ 2 s for waves that penetrate into the Sun as deep as $0.8R_\odot$. Our results are in a good agreement with the measurements of the variations in the effective acoustic radius by Vorontsov (2002). D'Silva (2001a) showed that the phase velocity is proportional to the acoustic radius. In turn, the time–distance representation is equivalent to Duvall's standard law (D'Silva 2001b). Indeed, the relative change in the phase velocity obtained here is 3×10^{-4}, which is in agreement with the measurements of the relative frequency shift of 2×10^{-4} by Libbrecht and Woodard (1990).

(2) The measured amplitudes of the cross-correlation functions carry important information about the loss of part of the wave packet energy. Although this loss can be partly attributed to the dispersion of acoustic waves as they reflect from the solar surface, we may still assert that the decrease of the amplitudes in the years of maximum solar activity compared to minimum activity is about 15%.

Note one feature in the behavior of the correlation amplitudes of wave packets with solar cycle found here: We see from Fig. 5 that the amplitude variations are insignificant in the subsurface region, down to depths of $\sim 0.97R_\odot$. However, the maximum perturbation attributable to solar activity is known to be localized in a narrow layer immediately beneath the photosphere. It follows from our results that the maximum perturbation arises at a depth of 0.83–$0.85R_\odot$. We hope that analysis of longer time series will allow us to localize the region of maximum perturbation of the wave packet correlation amplitudes more accurately.

ACKNOWLEDGMENTS

This work was supported in part by SCOPES grant no. 7UZPJ065728.01/1. O.S. Burtseva is grateful to the INTAS for support of her studies by a personal grant for young scientists (no. YSF 2001/2-41).

REFERENCES

1. D. C. Braun, C. Lindsey, Y. Fan, and S. M. Jefferies, Astrophys. J. **392**, 739 (1992).
2. H.-K. Chang, D.-Y. Chou, B. LaBonte, and TON team, Nature **389**, 825 (1997).
3. D.-Y. Chou and A. Serebryanskiy, Astrophys. J. **578**, 157 (2002).
4. D.-Y. Chou, M. T. Sun, T. Y. Huang, *et al.*, Sol. Phys. **160**, 237 (1995).
5. D.-Y. Chou, H.-Y. Chou, Y.-C. Hsieh, and C.-K. Chen, Astrophys. J. **459**, 792 (1996).
6. T. L. Duvall, Jr., Nature **300**, 242 (1982).
7. T. L. Duvall, Jr., S. M. Jefferies, J. W. Harvey, and M. A. Pomerantz, Nature **362**, 430 (1993).
8. T. L. Duvall, Jr., S. D'Silva, S. M. Jefferies, and J. W. Harvey, Nature **379**, 235 (1996).
9. E. Fossat, D. Salabert, A. Cacciani, *et al.*, *Proceedings of the SOHO 12,* Ed. by H. Sawaya-Lacoste, ESA SP-517 (ESA Publ. Div., Noordwijk, 2003), p. 139.
10. K. G. Libbrecht and M. F. Woodard, Nature **345**, 779 (1990).
11. K. G. Libbrecht and C. A. Morrow, *Solar Interior and Atmosphere,* Ed. by A. N. Cox, W. C. Livingston, and M. S. Matthews (Univ. Arizona Press, Tucson, 1991), p. 479.
12. C. Lindsey and D. C. Braun, Sol. Phys. **126**, 101 (1990).
13. F. Roddier, Comptes Rendus, Ser. B **281**, 93 (1975).
14. A. Serebryanskiy, Sh. Ehgamberdiev, Sh. Kholikov, *et al.*, New Astron. **6**, 189 (2001).
15. S. D'Silva, Astrophys. J. **547**, L81 (2001a).
16. S. D'Silva, Astrophys. J. **549**, L135 (2001b).
17. S. V. Vorontsov, *Proceedings of the SOHO 11,* Ed. by A. Wilson, ESA SP-508 (ESA Publ. Div., Noordwijk, 2002), p. 107.

Translated by V. Astakhov